Photonic Waveguides Evanescently Coupled with Single NV-centers

Lars Liebermeister

München 2015

Photonic Waveguides Evanescently Coupled with Single NV-centers

Lars Liebermeister

Dissertation
an der Fakultät für Physik
der Ludwig–Maximilians–Universität
München

vorgelegt von
Lars Liebermeister
aus München

München, den 02.11.2015

Erstgutachter: Prof. Dr. Harald Weinfurter
Zweitgutachter: Prof. Dr. Alexander Högele
Tag der mündlichen Prüfung: 18.12.2015

Abstract

The interaction of photons with individual quantum systems is a very fundamental process in physics. Thereby, the emission rate as well as the angular emission pattern of a quantum emitter are not only a function of intrinsic properties of the emitter itself, but are also strongly modified by its surrounding. For instance, by restricting the optical modes which are allowed at the position of the dipole, the emission rate can be strongly modified and the emitted photons can be directed into specific optical modes. This effect can be demonstrated by the interaction of a single optically active quantum emitter with the strongly confined optical mode of a single-mode dielectric waveguide. Efficient coupling of the emitter to the dielectric structure can be achieved by placing the quantum emitter inside the evanescent field of the guided mode. This evanescent field coupling mechanism is discussed and demonstrated experimentally.

A single nitrogen-vacancy center (NV-center), hosted in a nanodiamond is deterministically coupled to a tapered optical fiber (TOF) via the evanescent field of its guided mode (coupling efficiencies exceeding 30% are predicted). By employing an AFM-based nanomanipulation technique, the diamond nanocrystal is placed on the nanofiber waist of the TOF. Beforehand, the diamond nanocrystal has been characterized to guarantee that it hosts only one fluorescing NV-center. While the diamond nanocrystal is optically exited, single photon fluorescence of the NV-center is detected at both outputs of the tapered optical fiber. This verifies the evanescent coupling of the emitter to the guided mode. In order to quantify the coupling, the comparison of the emission rate into free space with the rate into the fiber yields that $(10 \pm 0.5)\%$ of the emitted photons are coupled into the tapered optical fiber. In the determination of this value, the orientation of the emitting dipoles and the emission pattern, which are modified by the TOF, have been considered. The NV-center features a broad emission spectrum which can be used to investigate the wavelength-dependence of the coupling. Comparing the spectra of the emission into the fiber mode with the emission into free space modes roughly resembles the expected wavelength dependency of the coupling efficiency.

The evanescent coupling and the deterministic positioning of preselected fluorescing diamond nanocrystals, which has been demonstrated with the TOF, can be applied to other waveguide structures as well. Dielectric single-mode waveguides made of Ta_2O_5 on a SiO_2 substrate promise similar coupling efficiencies to tapered optical fibers (above 30%). With the design of the on-chip wave-guiding structure being flexible, the combination with other optical on-chip elements is feasible, rendering it a promising platform for on-chip photonic experiments. Test structures of this waveguide design are realized using lithographic processes and are characterized. These waveguides are equipped with inverted taper structures to allow efficient off-chip coupling with butt-coupling to standard single-mode fibers.

The evanescent coupling of a single quantum emitter to a singe optical mode can be used to efficiently collect emission of the quantum emitter. This can help building a compact single photon source and is beneficial for the optical read-out of the quantum emitter's internal degree of freedom, which can be either used as probe (sensing) or as information-storage. Utilizing the high coupling efficiency, for instance, the non-linearities of the quantum system can be exploited to build a single photon transistor [1, 2]. The evanescent coupling is very broadband (about hundred nanometers), allowing to efficiently collect emission from broadband emitters like the NV-center, but it can also be used for multi-wavelength manipulation schemes.

Zusammenfassung

Die Wechselwirkung von Photonen mit einzelnen materiellen Quantensystemen ist ein sehr fundamentaler Prozess in der Physik. Besonders dabei ist, dass das Abstrahlverhalten, also die Emissionsrate und die Abstrahlcharakteristik, nicht rein auf intrinsischen Eigenschaften des Quantenemitters beruhen, sondern stark durch dessen Umgebung modifiziert werden. Beispielsweise kann die Reduzierung der erlaubten optischen Moden um den Emitter die Emissionsrate stark ändern, aber auch die emittierten Photonen in bestimme optische Moden leiten. Dieser Effekt lässt sich gut mit einem optisch aktiven Quantensystem demonstrieren, das an eine stark konzentrierte optische Mode eines Monomodelichtwellenleiters gekoppelt ist. Diese Kopplung kann beispielsweise erzeugt werden indem man den Quantenemitter in dem evaneszenten Feld des Wellenleiters platziert. Diese evaneszente Kopplung eines Quantenemitters an einen Monomodelichtwellenleiter wird in dieser Arbeit behandelt und experimentell demonstriert.

Zur experimentellen Realisierung eines derartig gekoppelten Systems wird ein einzelnes Stickstofffehlstellenzentrum (NV-Zentrum) in einem Nanodiamanten deterministisch an eine gedünnte optische Glasfaser (tapered optical fiber) gekoppelt (Kopplungseffizienz von mehr als 30% vorhergesagt). Diese Kopplung an das evaneszente Feld der Faser wird erreicht, indem der Nanodiamant mit einem Rasterkraftmikroskop (AFM) auf die Taille der gedünnten Glasfaser platziert wird. Der Nanodiamant wurde zuvor charakterisiert um sicherzustellen dass er nur ein einzelnes, optisch aktives Fehlstellenzentrum enthält. Unter kontinuierlicher optischer Anregung dieses gekoppelten Systems konnte das Einzelphotonenfluoreszenzsignal des NV-Zentrums an beiden Faserausgängen identifiziert werden. Dies verifiziert die erfolgreiche Kopplung. Aus dem Vergleich der detektierten Emissionsrate in die Faser und in den freien Raum wurde die Kopplungseffiziens in die geführte Mode zu $(10 \pm 0.5)\%$ bestimmt. Die Orientierung des Zentrums bezüglich der Faser und die dadurch modifizierte Abstrahlcharakteristik in den freien Raum sind dabei berücksichtigt. Dank des stark vibronisch verbreiterten Emissionsspektrums des NV-Zentrums konnte die Kopplungseffiziens auch wellenlängenabhängig betrachtet werden. Der Vergleich der Emissionsspektren in den freien Raum und in die Faser spiegelt grob das erwartete Verhalten wieder.

Diese evaneszente Kopplung, wie sie mit einem NV-Zentrum und einer gedünnten Faser demonstriert ist, kann ebenfalls auf andere Wellenleiterstrukturen angewandt werden. So versprechen dielektrische Monomodelichtwellenleiter aus Ta_2O_5 auf einem SiO_2-Substrat vergleichbare Kopplungseffizienzen (35%) wie die gedünnten Fasern. Dabei birgt die Flexibilität der Chip-basierter Strukturen enorme Vorteile da sich die Wellenleiter fast beliebig mit anderen photonischen Strukturen kombinieren lassen. Diese Tatsache macht die Wellenleiter auf einem Chip zu einer vielseitigen Plattform für zukünftige integrierte Experimente. Erste lithographisch fabrizierte Teststrukturen dieser Wellenleiter wurden hergestellt und charakterisiert. Die Wellenleiter sind zusätzlich mit Verjüngungen an den Enden ausgestattet um effiziente Kopplung an gewöhnliche optische Fasern zu gewährleisten.

Die evaneszente Kopplung eines einzelnen Quantenemitters an eine einzelne optische Mode erlaubt die effiziente Aufsammlung von dessen Fluoreszenz. Damit lassen sich einerseits effiziente Einzelphotonenquellen realisieren, es ist andererseits auch von großem Vorteil bei der optischen Auslese eines internen Freiheitsgrades des Quantensystems. Ein derartiger interner

Freiheitsgrad kann entweder als Sensor oder als Informationsspeicher dienen. Die hohe Kopplungseffiziens verspricht außerdem die Nichtlinearität des Quantensystems nutzen zu können um beispielsweise einen Einzelphotonentransistor zu realisieren [1, 2]. Eine entscheidender Vorteil dieser evaneszenten Kopplung gegenüber resonatorbasierter Methoden ist die enorme Breitbandigkeit ($> 100\,\mathrm{nm}$), die es erlaubt effizient Emission von breitbandigen Emittern wie dem NV-Zentrum, aufzusammeln aber auch aufwändige Manipulationsschemata erlaubt, die verschiedene Wellenlängen benutzen.

Contents

1. Introduction

The interaction of light and matter is a fundamental process in nature and has, therefore, been under investigation for decades. In the 1940s, Edward Mills Purcell discovered that the photon emission rate of an atom is not a purely intrinsic property, but can be strongly influenced by its environment [3]. With an atom coupled to a resonator, he demonstrated enhanced microwave photon emission probability compared to the uncoupled case. With this discovery, he founded a vast research field exploring and exploiting light-matter interaction in the context of quantum mechanics and quantum electro dynamics.

The spontaneous emission of a quantum emitter can be explained by a stimulated emission process, where the stimulation stems from the bath of photonic quantum fluctuations [4]. These photonic quantum fluctuations are virtual photons, temporarily generated and annihilated by fluctuations in the local energy, as allowed by the Werner Heisenberg's uncertainty principle. In an environment, structured by dielectrics, Maxwell's equations define certain allowed optical modes, which are allowed to be occupied by any photons and photonic vacuum fluctuations. The engineering of the vacuum fluctuation allows to enhance the emission into specific optical modes. The optical resonator or cavity is a prominent example for such an engineered environment, which is used to control and often to enhance the vacuum fluctuations. Moreover, a single optical mode, confined to a small lateral extension, can also boost the vacuum fluctuations in a way that an emitter exposed to these condensed fluctuations will emit a significant amount of photons directly into this confined mode. This coupling to a strongly confined optical mode, which can be realized with a simple dielectric waveguide, can be sufficient to achieve a significant amount of the fluorescence photons being directly coupled into the waveguide mode. This thesis is concerned with this effect and utilizes it to channel fluorescence photons from a single quantum emitter into a single-mode dielectric waveguide. This interaction of a single optical mode and a quantum emitter is utilized to collect a great amount of fluorescence of a single quantum emitter with a designed optical mode. As efficient collection of the emission implies mutual coupling of emitter and optical mode, a wide range of applications is conceivable. To study the coupling, a continuous waveguide is considered, featuring an intense evanescent field of the guided mode. The quantum emitter is positioned within this evanescent field, which mediates the coupling of the emitter and the guided mode. In the experiment, demonstrating this evanescent coupling, the quantum emitter is realized by a single nitrogen-vacancy defect center, which is hosted in a diamond nanocrystal.

With the ability to collect a great amount of photons of a single emitter, such a system finds implicit application in the realization of a very compact single photon source. Efficient single-photon sources are needed e. g. in the realization of a linear optical quantum computer (LOQC) [5, 6, 7]. Within this field of quantum information technology, the mutual coupling of an optical mode and a quantum emitter is of strong interest, as the strong non-linear behavior of a single quantum system is of great importance. For instance, a measurable phase-shift can

be imprinted onto a photon when passing a single coupled quantum system [8, 9, 10]. Such a coupled system can also be used as an optical single photon transistor [11, 12].

Many real quantum systems feature internal degrees of freedom which can be modified, but also read-out optically. The nitrogen-vacancy center is a well-known and heavily investigated example of such a system, since it shows long electron spin-coherence times, making it suitable for information storage [1, 2]. Such storage systems depend on an efficient coupling of the quantum emitter to the optical mode to ensure efficient state preparation and read-out. As known from the electronic information technology development throughout the past decades, compact design of the functional unit is the key to reach the necessary scalability. Hence, integrated optics is likely to dominate the field of quantum information technology.

For applications such as single photon source or as information storage, a quantum system is required, which shows very low interaction with its environment. However, quantum systems sensitive to their environment can be beneficial as well, as they can be used as probes and sensors. For sensing applications, point-like single emitters are very interesting, as they can probe their environment with a high spatial resolution. Examples, realized with nitrogen-vacancy centers, are sensing of temperature [13], electric fields [14], magnetic fields [15] and the local density of photonic states [16, 17]. For these applications, the necessary measurement time and the signal to noise ratio increases with the number of detected fluorescence photons of the emitter. Therefore, in a combined system of a nitrogen-vacancy center and a wave-guiding structure, the coupling efficiency of the emitter to a single optical mode is important. Here, the evanescent coupling can provide a compact and efficient design. The collecting of photons in the evanescent field, is of particular interest in the field on integrated optics, since the quantum system's emission is coupled directly into the waveguide. This allows a simple and very compact realization, as no collection optics are necessary. In addition, the combination with integrated optics can allow to combine the optical readout with analysis units, creating a lab on a chip (LOC) [18, 19]. Such on-chip systems are also interesting for fundamental research as they are well suited for experiments in a cryostat and noisy environments.

This work takes steps towards a highly integrated, efficient single photon source, which is based on the evanescent coupling of a single quantum emitter to a strongly confined waveguide mode. It opens with a discussion of the basics of the coupling of a single quantum system to an optical mode and the fundamentals of wave-guiding in dielectric structures (chapter 2). Based on this formalism, the evanescent coupling to cylindrical waveguides is evaluated, promising coupling efficiencies of several ten percent. After an introduction to the nitrogen-vacancy center (NV-center) as quantum emitter in chapter 3, the cylindrical waveguide is realized by the nanometer-sized waist of a tapered optical fiber (TOF) [20]. In this first experimental part (chapter 4), a single NV-center is placed onto a tapered optical fiber (TOF) to demonstrate the potential of evanescent coupling. The coupled system is realized experimentally, investigated and the coupling parameters are compared to their predicted values.

In the second experimental part (chapter 5), the design and fabrication of a platform for on-chip experiments is presented. This platform is based on dielectric optical single-mode waveguides (Ta_2O_5 on SiO_2), which is optimized for broadband ($600 \ldots 800\,\mathrm{nm}$) evanescent coupling to a single quantum emitter (expected efficiency: up to 36%) and efficient off-chip coupling to single-mode optical fibers using inverted tapers. In the final chapter (6) these results are summarized and an outlook to the future goals is provided.

2. Theory of Waveguide Dipole Coupling

The basic idea of dielectric waveguides is to engineer the refractive index in two spatial dimensions to continuously control the propagation of an electro-magnetic wave. The guidance of a light field in a waveguide can be interpreted as a continuous refocusing of the light beam during propagation. This prevents the light field from diverging but also can be used to create a strongly confined optical mode. By placing a quantum emitter, like an atom, within the confined mode the interaction between the guided light field and the quantum emitter can be enhanced. With this coupling, a decent fraction of the quantum system's emission can be expected to be directly emitted into the guided mode.

In this chapter, the principle behind the coupling of a quantum emitter to a confined light-field will be discussed, yielding the figures of merit, the emission enhancement factor α and the coupling efficiency β. Before actual values can be calculated, the waveguide structure and its optical modes need to be specified first. Therefore, the basic concepts of waveguides are derived for the one-dimensionally confined waveguide structure, which are then used to determine the field distributions of the cylindrical single-mode waveguide. From these field distributions, the figures of merit of the expected dipole coupling (α, β) for a coupled system of cylindrical waveguide and quantum emitter, can be calculated. This system is experimentally investigated in section 4. Later on, these figures of merit of the coupling will also be used to design an integrated waveguide system featuring a rectangular cross-section for on-chip experiments in chapter 5.

2.1. Coupling of a Dipole to a Confined Light Field

The coupling of a single quantum emitter to a waveguide can be quantified by comparing the emission rate Γ_{wg} into the waveguide modes to the total emission rate of the emitter in free space or an isotropic medium Γ_{iso}. The quotient of these two rates is referred to as emission enhancement parameter α. Another interesting parameter is the coupling efficiency β given by the ratio of emission rate into the waveguide mode Γ_{wg} to the emission rate into free space in presence of the waveguide Γ_{free} (illustrated in figure 2.1). For sake of simplicity, the quantum emitter is modeled as an artificial two-level atom. In this section, the radiative emission rate of such an artificial atom will be calculated in free space as well as in the vicinity of a waveguide structure. From these rates, the emission enhancement factor α and the coupling efficiency β will be derived. The resulting expressions will be applied to design and evaluate the waveguide structures such as the cylindrical waveguides within this chapter and the on-chip strip waveguides (chapter 5).

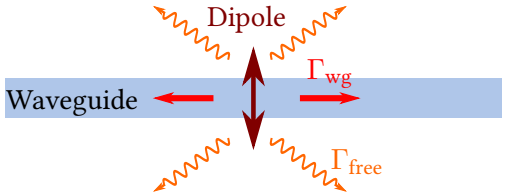

Figure 2.1.: Illustration of the emission rates of the dipole into the waveguide (light blue shaded area) Γ_{wg} and into free space Γ_{free} .

The interaction of a two-level atom with a light-field is generally described by an interaction Hamiltonian. Within the rotating wave approximation[1] [21], this Hamiltonian is established by the sum of the Hamiltonians of the atom $\hat{H}_A$, the light field $\hat{H}_L$ and their interaction $\hat{H}_I$ [22]. The atom has an excited $|e\rangle$ and a ground state $|g\rangle$ with an energy difference of $\hbar\omega_0$. With the ground-state energy normalized to zero, the Hamiltonian of the atom is then $\hat{H}_A = \hbar\omega_0\sigma_z/2 = \hbar\omega_0|e\rangle\langle e|$ [23]. The light field is expressed as the sum of modes $\boldsymbol{\kappa}$ (which can be radiative modes as well as the guided mode) with creation and annihilation operators $\hat{a}^\dagger_{\boldsymbol{\kappa}}$ and $\hat{a}_{\boldsymbol{\kappa}}$ and the energy per mode $\hbar\omega_{\boldsymbol{\kappa}}$. The Hamiltonian of the light field is the sum of all possible modes: $\hat{H}_L = \sum_{\boldsymbol{\kappa}} \hbar\omega_{\boldsymbol{\kappa}}\hat{a}^\dagger_{\boldsymbol{\kappa}}\hat{a}_{\boldsymbol{\kappa}}$. Within the rotating wave approximation, the interaction of the atom with an optical mode $\boldsymbol{\kappa}$ is given by the sum of atomic decay while creating a photon in mode $\boldsymbol{\kappa}$ and atomic excitation with annihilation of a photon from mode $\boldsymbol{\kappa}$: $\hat{a}^\dagger_{\boldsymbol{\kappa}}|g\rangle\langle e| + \hat{a}_{\boldsymbol{\kappa}}|e\rangle\langle g|$. This process is weighted by the coupling field strength $g_{\boldsymbol{\kappa}}$. The interaction Hamiltonian is now calculated by the sum over all modes $\boldsymbol{\kappa}$: $\hat{H}_I = \sum_{\boldsymbol{\kappa}} \hbar g_{\boldsymbol{\kappa}} \left(\hat{a}_{\boldsymbol{\kappa}}|e\rangle\langle g| + \hat{a}^\dagger_{\boldsymbol{\kappa}}|g\rangle\langle e|\right)$. The combined system of the atomic two-level system and the light field is then described in the dressed state picture by the sum of all three Hamiltonians, also known as the Jaynes-Cummings Hamiltonian [24]:

$$\hat{H} = \hbar\omega_0|e\rangle\langle e| + \sum_{\boldsymbol{\kappa}} \hbar\omega_{\boldsymbol{\kappa}}\hat{a}^\dagger_{\boldsymbol{\kappa}}\hat{a}_{\boldsymbol{\kappa}} + \sum_{\boldsymbol{\kappa}} \hbar g_{\boldsymbol{\kappa}} \left[\hat{a}_{\boldsymbol{\kappa}}|e\rangle\langle g| + \hat{a}^\dagger_{\boldsymbol{\kappa}}|g\rangle\langle e|\right] \tag{2.1}$$

with [23]:

$$g_{\boldsymbol{\kappa}} = \sqrt{\frac{\omega_0}{2\varepsilon\hbar V}}|\boldsymbol{\mu}|\langle\hat{\boldsymbol{\epsilon}}\cdot\hat{\boldsymbol{\mu}}\rangle \tag{2.2}$$

The scalar product $\langle\hat{\boldsymbol{\epsilon}}\cdot\hat{\boldsymbol{\mu}}\rangle$ of the unit vector $\hat{\boldsymbol{\epsilon}}$ of the electric field $\mathbf{E}(\mathbf{r})$ (polarization vector) with the unit vector $\hat{\boldsymbol{\mu}}$ of the dipole matrix element $\vec{\boldsymbol{\mu}} = \langle g|\boldsymbol{\mu}|e\rangle$ accounts for the angle between the dipole and the electric field. $|\boldsymbol{\mu}|$ is then the scalar dipole matrix element. The medium surrounding the atom has the dielectric permittivity ε. The quantization volume of the electromagnetic field is given by V.

The emission rate with an arbitrary photonic density of states $D(\omega) = \frac{1}{\hbar}\frac{\mathrm{d}N}{\mathrm{d}\omega}$ (variation of the number of photonic states N with the energy $\hbar\omega$) is given by Fermi's golden rule:

$$\Gamma = 2\pi|g(\mathbf{r},\omega)|^2 D(\omega) = \frac{\pi\omega}{\varepsilon\hbar}|\langle\hat{\boldsymbol{\epsilon}}\cdot\hat{\boldsymbol{\mu}}\rangle|^2|\boldsymbol{\mu}|^2\frac{D(\omega)}{V} \tag{2.3}$$

[1]Starting in the dipole approximation, the interaction Hamiltonian has terms oscillating with $\omega_{\boldsymbol{\kappa}} - \omega_0$ and terms oscillating with $\omega_0 + \omega_{\boldsymbol{\kappa}}$. The dynamics of emission and absorption considered here are on a time scale much slower than $1/\omega_0$ or $1/\omega$. Therefore, the latter terms, oscillating with the sum frequency $\omega_0 + \omega_{\boldsymbol{\kappa}}$ are assumed to average out on the relevant timescale. This approximation is referred to as rotating wave approximation.

This rule can now be used to calculate the emission rate of the atom in an isotropic medium [25]. The photonic density of states $D(\omega)$ can be derived as follows: Wave vectors $\mathbf{k}$ with the equal energy form spherical shells in the three-dimensional reciprocal space. The integrated surface of such shells results in the number of modes N per energy interval $\Delta\hbar\omega$. Now, the derivation of $D(\omega) = \frac{1}{\hbar}\frac{\mathrm{d}N}{\mathrm{d}\omega}$ can be performed, yielding:

$$D(\omega) = \frac{2\omega}{3\pi(c/n)^3}V \tag{2.4}$$

(Here, the dipole is embedded in an isotropic medium with the refractive index n). Now, substituting $D(\omega)$ in Fermi's golden rule (2.3) and using $\varepsilon = n^2\varepsilon_0$ the emission rate of the dipole in free space is:

$$\Gamma_{\text{iso}} = \frac{n\omega^3}{3\pi\hbar\varepsilon_0 c^3}|\boldsymbol{\mu}|^2 \tag{2.5}$$

Besides the natural constants, the emission rate in an isotropic medium is a function of the angular frequency ω of the transition, the squared transition matrix element $|\boldsymbol{\mu}|$ and proportional to the medium's refractive index n. This emission rate in an isotropic medium has to be compared to the emission rate into the guided modes of the waveguide structure Γ_{wg}. The waveguide structure is defined by a refractive index distribution in $n(x, y)$ which is invariant in the propagation direction $\hat{z}$.

For this derivation, a general description of the guided modes, which is given by the transverse light-field distribution of the complex electric field vector $\mathbf{E}(x, y) = (E_x(x, y), E_y(x, y), E_z(x, y))$, is useful. Variations with time t and in propagation direction z are chosen to yield only a phase factor which is equivalent to stationary and non-diverging light field. $\mathbf{E}(x, y)$ has to be square-integrable[2] (confined transversally) for guided optical modes. For sake of simplicity, the waveguide is assumed to be single-mode in this section, meaning that only one guided field-distribution $\mathbf{E}(x, y)$ exists. However, there also exists an infinite number of radiative modes. Besides its field distribution $\mathbf{E}(x, y)$, the group velocity v_{gr} of the waveguide mode has also to be taken into account in the following derivation. Both quantities depend on the actual waveguide geometry, the refractive index $n(x, y)$, and the wavelength λ.

As a waveguide is a non-uniform dielectric structure, the photonic density of final states $D(\omega)$ changes with position, which inspired the term local density of states (LDOS). The quantization volume for a waveguide mode is calculated by the effective mode area times the quantization length L, $V = A_{\text{eff}}L$. This effective mode area can be defined for the guided mode and the dipole orientation $\hat{\boldsymbol{\mu}}$:

$$A_{\text{eff}}(\mathbf{r}_0, \hat{\boldsymbol{\mu}}) = \frac{\iint n^2(x, y)\langle\mathbf{E}(x, y)\cdot\hat{\boldsymbol{\mu}}\rangle^2\mathrm{d}x\,\mathrm{d}y}{n^2(\mathbf{r}_0)\langle\mathbf{E}(\mathbf{r}_0)\cdot\hat{\boldsymbol{\mu}}\rangle^2} \tag{2.6}$$

Here, the position of the emitter is given by $\mathbf{r}_0 = (x_0, y_0, z_0)$. The effective mode area can be interpreted as the area of constant electric field intensity as experienced by the dipole $n^2(\mathbf{r}_0)\langle\mathbf{E}(\mathbf{r}_0)\cdot\hat{\boldsymbol{\mu}}\rangle^2$, which carries the equal total power $\iint n^2(x, y)\langle\mathbf{E}(x, y)\cdot\hat{\boldsymbol{\mu}}\rangle^2\mathrm{d}x\,\mathrm{d}y$ as the original mode in the component parallel to the dipole.

[2] The integral of the intensity distribution via the plane perpendicular to z must not diverge. Therefore, the $\int_{-\infty}^{\infty}\int_{-\infty}^{\infty}|\mathbf{E}(x, y)|^2\mathrm{d}x\mathrm{d}y$ has to result in a finite value.

The density of photonic states $D(\omega)$ in a one-dimensional structure is [26]:

$$D(\omega) = L/(2\pi v_{\mathrm{gr}}(\omega)) \tag{2.7}$$

with quantization length L and the group velocity $v_{\mathrm{gr}}(\omega)$. With the help of Fermi's golden rule (2.3) the total emission rate Γ_{wg} into a mode of a one-dimensional waveguide results in:

$$\Gamma_{\mathrm{wg}} = \frac{\omega}{2\hbar n^2 \varepsilon_0 A_{\mathrm{eff}} v_{\mathrm{gr}}} |\boldsymbol{\mu}|^2 \langle \hat{\boldsymbol{\epsilon}} \cdot \hat{\boldsymbol{\mu}} \rangle^2 \tag{2.8}$$

Here, Γ_{wg} is the total emission rate into the guided mode, i. e. the sum of the emission in both directions of the waveguide.

In order to calculate the enhancement of the rate emitted into the waveguide mode, the isotropic emission rate of the atom Γ_{iso} has to be compared to the emission rate into the guided mode Γ_{wg}. This fraction is referred to as emission enhancement factor α:

$$\alpha = \frac{\Gamma_{\mathrm{wg}}}{\Gamma_{\mathrm{iso}}} = \frac{3}{4\pi} \frac{c}{v_{\mathrm{gr}} n^3(\mathbf{r}_0)} \frac{\lambda_0^2 \langle \mathbf{E}(\mathbf{r}_0) \cdot \hat{\boldsymbol{\mu}} \rangle^2}{\int \varepsilon(x,y) \langle \mathbf{E}(x,y) \cdot \hat{\boldsymbol{\mu}} \rangle^2 \mathrm{d}x \, \mathrm{d}y} \langle \hat{\boldsymbol{\epsilon}} \cdot \hat{\boldsymbol{\mu}} \rangle^2 \tag{2.9}$$

$$= \frac{1}{2} \frac{n_{\mathrm{gr}}}{n(\mathbf{r}_0)} \frac{\sigma_A}{A_{\mathrm{eff}}(\mathbf{r}_0, \hat{\boldsymbol{\mu}})} \langle \hat{\boldsymbol{\epsilon}} \cdot \hat{\boldsymbol{\mu}} \rangle^2 \tag{2.10}$$

The second expression uses the scattering cross-section of a dipole $\sigma_A = 3\lambda_0^2/(2\pi n^2)$ and the group index $n_{\mathrm{gr}} = c/v_{\mathrm{gr}}$. Since the group velocity is the propagation speed of the envelope function of a wave-packet, it is easily recognizable, that a decreasing group velocity results in an increased interaction time of photon and atom. Here, it has been assumed that the refractive index at the position of the emitter $n(\mathbf{r}_0)$ is equal to the refractive index of the medium surrounding the free dipole.

The emission enhancement α is proportional to the intensity $|E_{\parallel}(\mathbf{r}_0)|^2$ of the electric field component parallel to the dipole at the position of the emitter $\mathbf{r}_0$. With a given electric field distribution $E_{\parallel}(\mathbf{r})$, α is strongest for that emitter position r_0 showing the maximum electric field intensity $|E_{\parallel}(\mathbf{r})|^2$. When optimizing the electric field intensity distribution $|E_{\parallel}(\mathbf{r})|^2$ shape for a maximum emission enhancement α, in general a highly confined mode is desirable as this shrinks the effective mode area A_{eff}. Using dielectric waveguides, an effective mode area A_{eff} of the same order of magnitude as the photonic scattering cross-section σ_A is in reach, resulting in an α which is around one and, therefore, a significant amount of photons are emitted into the guided mode. The maximization of α optimizes the emission rate into the guided mode. However, the parameters at this maximum do not necessarily coincide with the parameters maximizing the coupling efficiency of the emitter and the optical mode. As the presence of the waveguide changes the the allowed free-space modes (as can be seen in the modification in the far-field emission pattern), coming along with a modification of the photonic density of states (LDOS) compared to the isotropic medium, the emission rate into free space modes differs from the rate in the isotropic case $\Gamma_{\mathrm{free}} \neq \Gamma_{\mathrm{iso}}$. Furthermore, due to practical reasons[3], the emission

[3]Fluorescing diamond nanoparticles, as used in this thesis as quantum emitters, are nanoscale solids which have to be kept in place for the investigations. The investigation of the diamond nanoparticles, embedded in an isotropic environment prior to the coupling to a waveguide, is experimentally unpractical. Optically levitation of fluorescing nanocrystals has been demonstrated[27], but the optical trap shows a strong influence on the fluorescence emission.

rate in an isotropic medium Γ_{iso} is difficult to determine experimentally, as is the emission enhancement factor α. Easier to access is the total emission rate in presence of the waveguide from which the coupling factor β can be derived. The coupling efficiency or coupling factor β is defined as the ratio of the photon rate emitted into the waveguide Γ_{wg} to the total radiative decay rate $\Gamma_{\text{rad}} = \Gamma_{\text{wg}} + \Gamma_{\text{free}}$ in presence of the waveguide structure.

$$\beta = \Gamma_{\text{wg}}/\Gamma_{\text{rad}} = \frac{\Gamma_{\text{wg}}}{\Gamma_{\text{wg}} + \Gamma_{\text{free}}} \tag{2.11}$$

This coupling efficiency β is the probability of a photon being emitted into the guided mode. Alternatively, β can also be interpreted as the probability of the two-level system absorbing a photon from the guided mode. As mentioned above, the emission rate into the waveguide mode Γ_{wg} is defined as the sum of right and left propagating emission. β is then twice the coupling factor to one propagation direction. Therefore, the actual probability to absorb a single photon coming from one side is $\beta/2$ [28].

The presence of the waveguide has a direct impact on the total emission rate Γ_{rad} of the emitter and also on the excited state lifetime τ_{tot}. Such an influence of the surroundings on the lifetime of an emitter has first been described by Purcell [3]. A change of the local density of states (LDOS) changes the lifetime of its excited state $\tau_{\text{iso}}/\tau_{\text{tot}}$. This lifetime change can be described in terms of the Purcell factor[4] [3] even though no cavity is present. The Purcell factor compares the emission rate into the structure Γ_{wg} with the emission rate in an isotropic medium Γ_{iso} [29].

$$F_{\text{P}} = \frac{\Gamma_{\text{wg}}}{\Gamma_{\text{iso}}} = \alpha \tag{2.12}$$

The modification of the overall radiative decay rate, which can also be seen as a change of the emitters radiative lifetime compared to the isotropic case, is given by the fraction of emission enhancement factor α and the coupling β.

$$\frac{\tau_{\text{iso}}}{\tau_{\text{tot}}} = \frac{\Gamma_{\text{rad}}}{\Gamma_{\text{iso}}} = \frac{\alpha}{\beta} = \frac{\Gamma_{\text{free}}}{\Gamma_{\text{iso}}} + F_{\text{P}} \tag{2.13}$$

Concluding, as the waveguide adds additional photonic decay channels with the possibility of high coupling, the Purcell factor F_{P} can be larger than one [28].

The basic figures of merit concerning the coupling of a radiating dipole to a wave-guiding structure have been discussed. To continue the discussion, the waveguide modes of interest have to be specified first. Therefore, the next section provides an introduction into the basics of guided modes in dielectric waveguides.

[4] Often, the change in lifetime is referred to as the Purcell factor $F_{\text{P}} = \tau_{\text{iso}}/\tau_{\text{tot}} = \alpha/\beta$ [28]. However, in his calculation [3], Purcell neglects a change in radiative emission rate due to the presence of the resonant circuit $\Gamma_{\text{iso}} \approx \Gamma_{\text{free}}$ resulting in the widely adapted definition of the Purcell factor as $F_{\text{P}} = \Gamma_{\text{wg}}/\Gamma_{\text{iso}} = \alpha$ with $\tau_{\text{iso}}/\tau_{\text{tot}} = 1 + F_{\text{P}}$. This is justified for high coupling factors $\beta \gg 0.9$, as the change in lifetime is dominated by the scattering rate into the cavity mode Γ_{wg} and leads to the widely used expression: $F_{\text{P}} \approx \frac{\beta}{1+\beta}$. However, if β is not close to one, as assumed here, the typical QED approximation is not justified and the more general expression $F_{\text{P}} = \alpha$ with $\Gamma_{\text{rad}}/\Gamma_{\text{iso}} = F_{\text{P}} + \Gamma_{\text{free}}/\Gamma_{\text{iso}}$ is used [29].

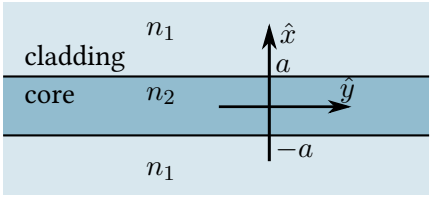

Figure 2.2.: Basic one-dimensional slab waveguide structure, also known as dielectric sandwich structure or planar waveguide. The structure is indifferent in y and the propagation direction z, but shows a step-function in the refractive index parallel to the x-axis.

2.2. One-Dimensional Slab Waveguides - Fundamental Waveguide Properties

The fundamentals of waveguiding structures will be discussed by means of a one-dimensionally confined waveguide. The results will then pose the basis for the understanding of the tapered optical fiber (section 2.3) as well as the slab waveguides (section 5.1). The discussion presented here skips some of the mathematical details. However, a more rigorous analytical treatment of a one-dimensional slab waveguides can be found in the appendix A.

A basic structure (figure 2.2), showing the fundamental properties of dielectric waveguides, is a layer with refractive index n_2, thickness $2a$ along the axis $\hat{x}$ and infinite extent in the two other dimensions (axes $\hat{y}$ and $\hat{z}$). This layer is referred to as the core and is embedded in a so called cladding with refractive index n_1. Within the ray optics picture, where the guidance is mediated by total internal reflection at the dielectric interfaces, it is intuitively clear that n_2 has to be greater than n_1 to allow guidance. The structure is illustrated in figure 2.2 and can be described in mathematical terms as a step function:

$$n(\mathbf{r}) = n(x) = \begin{cases} n_1 & \text{for } |x| > a \\ n_2 & \text{for } |x| < a \end{cases} \qquad \text{and} \qquad n_1 < n_2 \tag{2.14}$$

In the following, the basic properties of dielectric waveguides are derived, based on Maxwell's equations.

Maxwell's equations in purely dielectric media can be written as follows (with $\mathbf{r} = (x, y, z)$) [30]:

$$\nabla \times \mathbf{E}(\mathbf{r}, t) + \frac{\partial \mathbf{B}(\mathbf{r}, t)}{\partial t} = 0 \tag{2.15a}$$

$$\nabla \times \mathbf{H}(\mathbf{r}, t) - \frac{\partial \mathbf{D}(\mathbf{r}, t)}{\partial t} = 0 \tag{2.15b}$$

$$\nabla \cdot \mathbf{D}(\mathbf{r}, t) = 0 \tag{2.15c}$$

$$\nabla \cdot \mathbf{B}(\mathbf{r}, t) = 0 \tag{2.15d}$$

Here, **E**, **D**, **B**, and **H** are the complex vector fields of the electric field and the electric displacement field as well as the complex pseudovector fields of the magnetic field, and the magnetizing

field, respectively. Additionally, there are two relations taking into account the materials involved by including the dielectric permittivity ε and the magnetic permeability μ :

$$\mathbf{B}(\mathbf{r},t) = \mu_0 \mathbf{H}(\mathbf{r},t) \tag{2.16a}$$

$$\mathbf{D}(\mathbf{r},t) = \varepsilon(\mathbf{r})\mathbf{E}(\mathbf{r},t) \tag{2.16b}$$

With the assumption of well-behaved functions (they fulfill Schwarz' theorem [31]) which allows to switch the order of temporal and spatial derivatives, the stationary wave equations for monochromatic light can be derived:

$$\left(\Delta - \mathbf{k}^2 n^2(\mathbf{r})\right) \mathbf{E}(\mathbf{r}) = 0 \tag{2.17a}$$

$$\left(\Delta - \mathbf{k}^2 n^2(\mathbf{r})\right) \mathbf{H}(\mathbf{r}) = 0 \tag{2.17b}$$

Here, the Laplacian operator $\Delta\mathbf{E}(\mathbf{r}) = \nabla \times \nabla \times \mathbf{E}(\mathbf{r})$ and the wave vector $\mathbf{k}$ have been introduced.

Since the structure is invariant in $\hat{y}$ and $\hat{z}$, $\hat{z}$ is, without loss of generality, chosen as the direction of propagation. The propagation of a monochromatic wave can be expressed with a propagation constant consisting of the absolute value of the vacuum wave vector $k = \sqrt{\mathbf{k}^2}$ times the effective refractive index n_{eff}. For any field distribution, the effective refractive index n_{eff} has to take a value between n_1 and n_2. Choosing $\hat{z}$ as the direction of propagation and the fields being invariant in $\hat{y}$ yields (with the imaginary unit $\imath$):

$$\mathbf{E}(\mathbf{r}) = \mathbf{E}(x) \exp(-\imath n_{\text{eff}} k z) \qquad \text{with} \qquad n_1 < n_{\text{eff}} < n_2 \tag{2.18}$$

These simplifications can be inserted into the wave equations (2.17a) and (2.17b). After evaluating the derivative of the Laplacian, the functional dependence on z is dropped. The resulting wave equations are:

$$\frac{\mathrm{d}^2\mathbf{E}(x)}{\mathrm{d}x^2} + \left(n(x)^2 - n_{\text{eff}}^2\right) k^2 \, \mathbf{E}(x) = 0 \tag{2.19a}$$

$$\frac{\mathrm{d}^2\mathbf{H}(x)}{\mathrm{d}x^2} + \left(n(x)^2 - n_{\text{eff}}^2\right) k^2 \, \mathbf{H}(x) = 0 \tag{2.19b}$$

These equations can be solved by two orthogonal modes with different polarization. They are distinguished by their transverse ($\hat{y}$) field component, the transverse electric (TE) and the transverse magnetic (TM) mode:

$$\text{TE:} \qquad \mathbf{E} = \begin{pmatrix} 0 \\ E_y \\ 0 \end{pmatrix} \qquad \mathbf{H} = \begin{pmatrix} H_x \\ 0 \\ H_z \end{pmatrix} \tag{2.20}$$

$$\text{TM:} \qquad \mathbf{E} = \begin{pmatrix} E_x \\ 0 \\ E_z \end{pmatrix} \qquad \mathbf{H} = \begin{pmatrix} 0 \\ H_y \\ 0 \end{pmatrix} \tag{2.21}$$

The solutions to (2.19a) and (2.19b) can be either an exponential decay or a harmonic oscillation with x depending on the sign of $(n(x)^2 - n_{\text{eff}}^2)$. The equations will be solved separately in the three regions (above, within, and below the waveguide) and afterwards the solutions will be related at the interface based on continuity considerations.

Transverse Electric Modes: The solutions $E_y(x)$ for equation (2.19a) describing a transverse electric mode are:

$$\text{TE}: \qquad E_y(x) = \begin{cases} \mathcal{E}_{y,1} \exp\left[2\pi\sqrt{n_{\text{eff}}^2 - n_1^2}\,(x+a)\right] & \text{for } x < -a \\ \mathcal{E}_{y,2} \cos\left[2\pi\sqrt{n_2^2 - n_{\text{eff}}^2}\,x + \gamma\right] & \text{for } |x| < a \\ \mathcal{E}_{y,1} \exp\left[2\pi\sqrt{n_{\text{eff}}^2 - n_1^2}\,(a-x)\right] & \text{for } x > a \end{cases} \tag{2.22}$$

with the amplitudes $\mathcal{E}_{y,i}$. Here, the natural length scale is the wavelength λ of the light. Therefore, it is convenient to express all lengths like the coordinates x, y, z and the waveguide width $2a$ in units of the vacuum wavelength λ. With this choice, the absolute value of the wave vector k equals 2π. The lateral field distribution can be either symmetric or antisymmetric. Depending on the phase factor γ which is 0 for even and $\pi/2$ for odd modes. In the core ($x < a$) the effective refractive index n_{eff} is the parameter defining the lateral oscillation period. A small core region ($a \ll 1$) results in n_{eff} being close to n_1, which creates fast oscillations with x. On the other hand, n_{eff} approaches n_2 for very wide cores ($a \gg \lambda$) which is causing slow oscillations with x. Evidently, for a certain finite waveguide width a, only a discrete range of n_{eff} allows the existence of either symmetric or antisymmetric modes. Such a set of mode profiles is enumerated by the mode index number q, which corresponds to the number of nodes in the intensity distribution. Every mode is a specific combination of a lateral oscillation length inside the core and an exponential decay into the cladding $|x| > a$, referred to as the evanescent field. Similar to the situation for the oscillation length in the core the evanescent field in the cladding decays fast if n_{eff} approaches n_2, or can become very large (many wavelengths) if n_{eff} is close to n_1.

The corresponding magnetizing field $\mathbf{H}(x)$ can be calculated using Maxwell's equations. The functional dependency $\mathbf{E}(z)$ (2.18) has to be remembered at this point as well as k has been set to 2π by expressing all length scales in units of the wavelength λ. The non-vanishing components, therefore, are:

$$H_x(x) = -\frac{2\pi n_{\text{eff}}}{\omega\mu_0} E_y(x) \tag{2.23a}$$

$$H_z(x) = -\frac{1}{j\omega\mu_0} \frac{\partial E_y(x)}{\partial x} \tag{2.23b}$$

The relative amplitudes $\mathcal{E}_y$ can be determined from the continuity relations regarding the parallel and perpendicular components of the electric and magnetic fields at the core-cladding interface. These continuity relations can be derived directly from Maxwell's equations and are, therefore, very general for any jump in the relative dielectric permittivity ε_r and/or the relative magnetic permeability μ_r [30]. The components of the four fields **D**, **E**, **B**, and **H**, which are parallel $\parallel$ and perpendicular $\perp$ to the dielectric interface, are continuous at the interface but with the following exceptions. If there is a jump in the dielectric permittivity ε_r, the parallel component of the electric displacement field $D_\parallel$ and the perpendicular component of the electric field $E_\perp$ are discontinuous. In the same way, if there is a jump in the relative magnetic

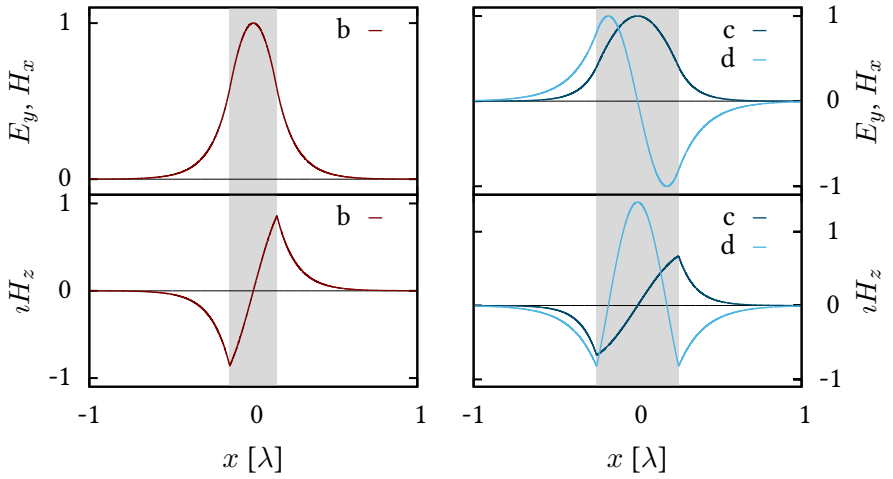

Figure 2.3.: Exemplary illustration of the TE-modes for two different waveguide widths. The profiles of the electric field $E_y(x)$, the magnetizing fields $H_x(x)$, and $H_z(x)$ are plotted in individual arbitrary units as function of the x-coordinate which is given in units of the wavelength λ. The electric field component $E_y(x)$ and the magnetizing field $H_x(x)$ are proportional and therefore result in the same curve due to the normalization. The refractive indices are chosen to be $n_1 = 1$ in the cladding (white) and $n_2 = 2$ in the core (indicated by the gray shaded area). The waveguide widths $2a$ are 0.288λ (single-mode regime, close to cut-off) on the left and 0.5λ (multi-mode regime) on the right. The mode index q for mode d and b is 0 whereas it is 1 for the mode c.

permeability μ_r at the interface, the perpendicular component of the magnetizing field $H_\perp$ and the parallel component of magnetic flux density $B \parallel$ are discontinuous. Summarizing these continuity relations provides:

$$\text{continuous:} \quad D_\perp \; E_\parallel \; B_\perp \; H_\parallel \qquad \text{potentially discontinuous:} \quad E_\perp \; D_\parallel \; H_\perp \; B_\parallel \tag{2.24}$$

Applying these continuity relations to the TE-mode $\mathbf{E}(x)$, and $\mathbf{H}(x)$ are found to be continuous (e.g. $\mathbf{E}_y(a+\epsilon) \overset{\epsilon\to 0}{=} \mathbf{E}_y(a-\epsilon)$). From equation (2.23b), it directly follows that in this case also the derivative $\partial E_y/\partial x$ is continuous. Then, $E_y(x)$ and $H_x(x)$ are smooth without kinks as illustrated in the example solutions plotted in figure 2.3.

By comparison of the relative amplitudes $\mathcal{E}_{y,(1,2)}$, provided by the continuity of $E_y(x)$ and $H_z(x)$, a necessary condition for the existence of a mode with the mode number q can be derived (see appendix A for details):

$$q = 4\sqrt{n_2^2 - n_{\text{eff}}^2}\, a - \frac{2}{\pi} \arctan\left[\sqrt{\frac{n_{\text{eff}}^2 - n_1^2}{n_2^2 - n_{\text{eff}}^2}}\right] \qquad q \in \mathbb{N} \tag{2.25}$$

For a given waveguide with width $2a$ and refractive indices n_1 and n_2, every effective refractive index n_{eff} allows a stable guided mode for which equation (2.25) results in an integer number q.

The electric field of the TE-mode has only a component in y, therefore, its polarization is in-plane with the dielectric interface, but perpendicular to the propagation direction. As discussed before, there is a second class of modes, the TM-modes. These modes have a polarization perpendicular to y and also a non-vanishing electric field component in the propagation direction ($|E_z| > 0$).

Transverse Magnetic Modes: At first sight, the solution $H_y(x)$ for the transverse magnetic modes (TM) of equation (2.19b) is identical to $E_y(x)$ derived for the TE-modes (2.22):

$$H_y(x) = \begin{cases} \mathcal{H}_{y,1} \exp\left[2\pi\sqrt{n_{\text{eff}}^2 - n_1^2}\,(x+a)\right] & \text{for } x < -a \\ \mathcal{H}_{y,2} \cos\left[2\pi\sqrt{n_2^2 - n_{\text{eff}}^2}\,x + \gamma\right] & \text{for } |x| < a \\ \mathcal{H}_{y,1} \exp\left[2\pi\sqrt{n_{\text{eff}}^2 - n_1^2}\,(a-x)\right] & \text{for } x > a \end{cases} \tag{2.26}$$

However, new effects appear for the electric field components for TM-modes which again are derived directly from Maxwell's equations:

$$E_x(x) = -\frac{2\pi n_{\text{eff}}}{\omega\varepsilon_0 n^2(x)} H_y(x) \tag{2.27}$$

$$E_z(x) = \frac{1}{\imath\omega\varepsilon_0 n^2(x)} \frac{\partial H_y(x)}{\partial x} \tag{2.28}$$

Here, the proportionality is modified by the relative permittivity $\varepsilon_r(x) = n^2(x)$ which causes a jump in $E_x(x)$ at the interface. With this jump the local field intensity $\mathbf{E}^2(x)$ of the evanescent field can be larger than the field within the core (see figure 2.4). As discussed before, $E_z(x)$ has to be continuous but this time the derivative $\partial H_y(x)/\partial x$ is not, causing $H_y(x)$ to show kinks at the interfaces (see figure 2.4).

Analogous to the TE-mode, from the continuity relations (2.24) the conditions on n_{eff} for guidance can be derived:

$$q = 4\sqrt{n_2^2 - n_{\text{eff}}^2}\,a - \frac{2}{\pi} \arctan\left[\left(\frac{n_2}{n_1}\right)^2 \sqrt{\frac{n_{\text{eff}}^2 - n_1^2}{n_2^2 - n_{\text{eff}}^2}}\right] \qquad q \in \mathbb{N} \tag{2.29}$$

This equation is nearly identical to what have been found for the TE-mode (2.25), but with the factor $(n_2/n_1)^2$ in the arctangent. One effect of this modification is that TE and TM-modes show different effective refractive indices n_{eff} for the same mode index q. In general, TE-modes show a larger n_{eff} for the same mode number q resulting in a higher propagation constant $n_{\text{eff}}k$ and lower phase velocity $v_{\text{ph}} \propto 1/n_{\text{eff}}$.

In contrast to the TE-mode, the TM-mode has an electric field component in x and in z. As both components differ by the imaginary unit $\imath$ they have a fixed relative phase-shift of $\pi/2$. This results in a rotating electric field vector in a plane parallel to the propagation direction

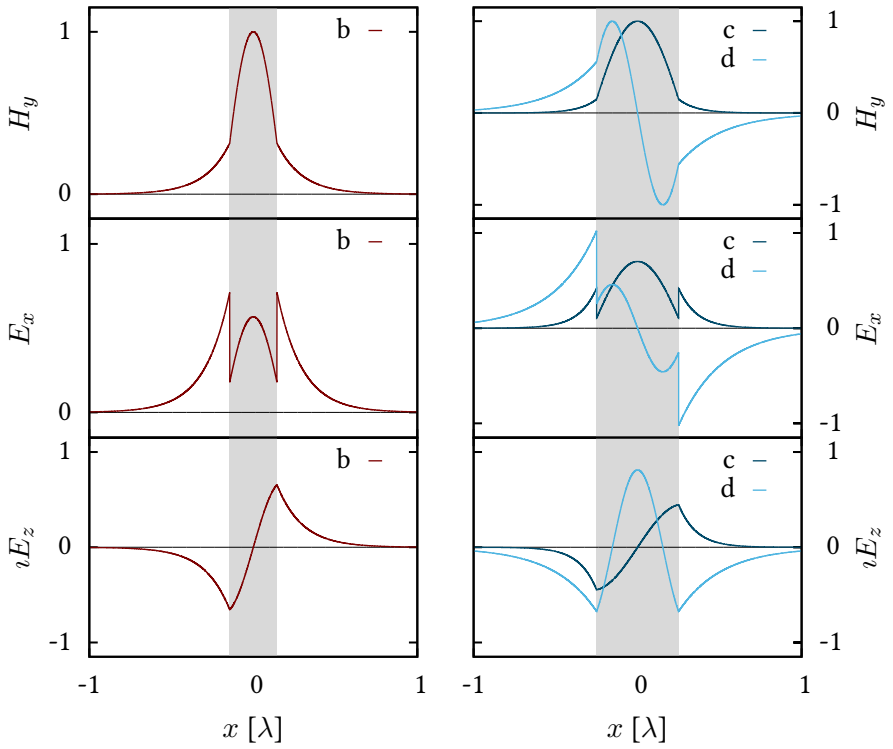

Figure 2.4.: The TM-mode, illustrated exemplary for the same two waveguide widths as in figure 2.3. The profiles of the magnetizing field $H_y(x)$, the electric fields $E_x(x)$, and $E_z(x)$ is plotted in individual arbitrary units as a function of the x-coordinate. The units used for x is the wavelength λ. The refractive indices are chosen to be $n_1 = 1$ for the cladding and $n_2 = 2$ in the core (marked as gray shaded area). The waveguide widths $2a$ are 0.288λ (single-mode regime, close to cut-off of the second order mode) on the left resulting in mode "b" and 0.5λ (multi-mode regime) on the right yielding the fundamental mode "c" and the first and only higher order mode "d". The mode index q for fundamental mode "d" and "c" is zero whereas it is one for the first higher order mode "d". In the appendix A, mode profiles for additional waveguides widths are illustrated.

and perpendicular to the dielectric interface.

For every guided mode, except the for fundamental modes, ($q \geq 1$) there is a specific relative waveguide width a for a specific wavelength below which the mode does not exist. This transition is referred to as the cut-off wavelength $\lambda_{\text{cut},q}$ of the mode q. If no mode is specified, the cut-off wavelength of a specific waveguide is defined as wavelength where the transition of single-mode to multi-mode operation occurs ($\lambda_{\text{cut}} = \lambda_{\text{cut},1}$). The cut-off waveguide width a_{cut} can be derived from equations (2.25) (TE modes) or (2.29) (TM modes) by setting the effective refractive index $n_{\text{eff},q}$ of mode q to n_1 as this represents the cut-off condition. For the TE- and the TM-modes the same result can be found:

$$a_{\text{cut},q} = \frac{q}{4\sqrt{n_2^2 - n_1^2}} \tag{2.30}$$

The propagation constant $n_{\text{eff}}k = 2\pi n_{\text{eff}}/\lambda$ has a non-trivial dependence on the wavelength, since the effective refractive index $n_{\text{eff}}(\lambda)$ itself is a function of the wavelength. In this sense the waveguide geometry creates a chromatic dispersion additional to possible intrinsic dispersions of the materials. This dispersion manifests itself in a difference in phase velocity and group velocity of a propagating wave packet. The phase evolution during propagation can be expressed by the phase velocity of mode q:

$$v_{\text{ph},q} = \frac{\omega}{n_{\text{eff},q}k_q} = \frac{c}{n_{\text{eff},q}} \tag{2.31}$$

with the angular frequency of the light wave ω and the vacuum speed of light c. As found in the previous section (see equation (2.10)), the emission enhancement factor α is proportional to the group index n_{gr} which is the vacuum speed of light c divided by the group velocity v_{gr}. The group index n_{gr} can also be expressed by:

$$1/n_{\text{gr}} = \frac{v_{\text{gr}}}{c} = \frac{1}{c}\frac{\partial\omega}{\partial(n_{\text{eff}}k)} = \frac{\partial k}{\partial(n_{\text{eff}}k)} = n_{\text{eff}}^{-1} + k\frac{\partial n_{\text{eff}}^{-1}}{\partial k} = n_{\text{eff}}^{-1} - \lambda\frac{\partial n_{\text{eff}}^{-1}}{\partial\lambda} \tag{2.32}$$

In the limit of a waveguide which is narrow compared to the wavelength, the transcendental equation (2.25) for the TE-mode can be analyzed further. Clearly, the single mode regime is valid ($q = 0$), yielding:

$$a = \frac{1}{2\pi\sqrt{n_2^2 - n_{\text{eff}}^2}} \arctan\left[\sqrt{\frac{n_{\text{eff}}^2 - n_1^2}{n_2^2 - n_{\text{eff}}^2}}\right] \tag{2.33}$$

As with decreasing a also the arctangent decreases, it can be approximated linearly with $\arctan(x) \approx x$. Additionally, for small a, the effective refractive index n_{eff} is approaching n_1. Therefore, $(n_2^2 - n_{\text{eff}}^2) \approx (n_2^2 - n_1^2)$ can be used:

$$a \approx \frac{1}{2\pi(n_2^2 - n_1^2)}\sqrt{n_{\text{eff}}^2 - n_1^2} \tag{2.34}$$

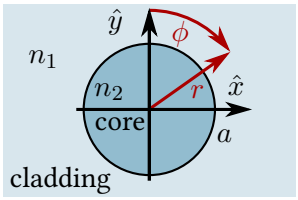

Figure 2.5.: Cylindrical waveguide shown schematically in cross section. This type of structure is realized in nanofibers as well as in standard optical fibers. The radius of the cylindrical waveguide is a. The cylindrical coordinates r and ϕ are indicated by red arrows. The z-axis, which is shared by Carthesian and cylindrical coordinates, points into the plane.

The approximation (2.34) can be used in the exponential decay of the evanescent field as it is described for $x > a$ ($x < a$ is equivalent) in equation (2.22). The approximated decay for small a can be written as:

$$E_y^{\mathrm{TE}}(x) \approx \mathcal{E}_{y,1} \exp\left[-4\pi^2(n_2^2 - n_1^2)a\, x\right] \qquad \text{for } x > a \tag{2.35}$$

This representation shows, that, for waveguide widths small compared to the wavelength (small a) the decay-length of the evanescent field is inversely proportional to the waveguide width a. Therefore, a half the waveguide width can lead to twice the extend of the evanescent field.

Concluding, a simple one-dimensional sandwich structure features two distinct sets of modes, the transverse electric and transverse magnetic mode. They show similar properties but also certain differences due to the asymmetry in the material properties (equal μ_r but different ε_r). Based on the continuity relations, the evanescent field of the transverse magnetic modes (TM) can be much stronger and even exceeding the maximum inside the waveguide. At the interface, this set of modes features also a strong electric field component in the direction of propagation (z). In the limit of very wide waveguides, as well as for very thin waveguides, the intensity of the evanescent field on the surface is low, however, there exits a maximum in the evanescent field intensity when the waveguide width is of the same order of magnitude as the wavelength. This regime is referred to as the strong evanescent field regime which coincides with the regime of a strongly confined mode as the extend of the mode is minimal.

In two-dimensionally confined waveguides, the TE and TM modes form hybrids showing properties of both types, e.g. the jump in the electric field at the surface but also its continuity depending on the angle of the local electric field vector to the surface. These features will be discussed in the following section which is attributed to cylindrical waveguides.

2.3. Cylindrical Waveguides

A natural choice for the confinement of light in two dimensions is a cylindrical core embedded in infinitely extended cladding. The perhaps simplest and most prominent example of such a

cylindrical dielectric waveguide is the optical fiber, which is a standard tool in telecommunication technology and science. Such optical fibers represent a special type of cylindrical waveguides with a large core radius compared to the wavelength $a \gg \lambda$ and a very weak refractive index contrast $n_2/n_1 \approx 1$. Due to the resulting low mode confinement they are referred to as weakly guiding fibers. The modes of such weakly guiding fibers can be approximated as linear polarized (LP) modes, also known as transverse electro-magnetic modes (TEM), as in this approximation the electric and the magnetic field feature transverse components only. A derivation of this linear polarized mode approximation also known as weak-guidance approximation can be found in the literature such as [32].

In contrast, the work presented here focuses on nanofibers with a diameter smaller than the wavelength and a high refractive index contrast ($n_2/n_1 \approx 1.4$). In this case, an approximation with linear polarized (LP) modes is not justified [33], instead the exact solutions to Maxwell's equations have to be used.

The discussion of the cylindrical waveguides presented here starts with the general derivation and discussion of the mode profiles (following the approach of [33]). This treatment will focus on single-mode nanofibers featuring strong mode confinement. This discussion leads to actual values of the coupling parameters α and β for an emitting dipole coupled to the nanofiber.

2.3.1. Optical Mode Profiles of Nanofibers

For a dielectric cylinder (illustrated in figure 2.5), cylindrical coordinates ($\mathbf{r} = (r,\, \phi,\, z)$) are the natural choice. Let the waveguide, as well as the light propagation, be parallel to the axis $\hat{z}$, then the radial coordinate is $r = |\mathbf{r}| = \sqrt{x^2 + y^2}$ and the angular coordinate is $\phi = \arctan(y/x)$. Thus, the core region is defined by $r < a$. The core material refractive index is denoted as n_2, while the surrounding cladding ($r \geq a$) has the refractive index n_1, fulfilling $n_1 < n_2$. The waveguide structure is invariant in z and ϕ and the refractive index n can be expressed as a step function of r:

$$n(\mathbf{r}) = n(r) = \begin{cases} n_1 & \text{for } r \geq a \\ n_2 & \text{for } r < a \end{cases} \qquad \text{and} \qquad n_1 < n_2 \tag{2.36}$$

The wave equations (2.17a) and (2.17b) can be expressed in cylindrical coordinates. Additionally, the derivative with respect to z can be evaluated immediately in analogy to (2.18) with $\frac{\partial^2}{\partial z^2} = -n_{\text{eff}}^2 k^2$:

$$\left(\frac{\partial^2}{\partial r^2} + \frac{1}{r}\frac{\partial}{\partial r} + \frac{1}{r^2}\frac{\partial^2}{\partial \phi^2} - (n_{\text{eff}}^2 - n^2(r))k^2 \right) \mathbf{E}(r,\, \phi,\, z) = 0 \tag{2.37a}$$

$$\left(\frac{\partial^2}{\partial r^2} + \frac{1}{r}\frac{\partial}{\partial r} + \frac{1}{r^2}\frac{\partial^2}{\partial \phi^2} - (n_{\text{eff}}^2 - n^2(r))k^2 \right) \mathbf{H}(r,\, \phi,\, z) = 0 \tag{2.37b}$$

Linear solutions for the lateral field distributions $\mathbf{E}(r,\, \phi)$, $\mathbf{H}(r,\, \phi)$ have to be separable of the form:

$$\mathbf{E}(r,\, \phi) = \mathbf{F}(r)\mathbf{G}(\phi) \qquad \mathbf{H}(r,\, \phi) = \mathbf{L}(r)\mathbf{M}(\phi) \tag{2.38}$$

With the substitution (2.38) and rearrangement of the dependencies on r and ϕ in (2.37a) and (2.37b), they can be separated. These equations can only be solved for all values of r and ϕ if both parts, $\mathbf{G}(\phi)$ and $\mathbf{F}(r)$ are equal to a constant, which will be named m^2 and l^2, respectively. Then, two equations per field can be found. In the following, the discussion focuses on the solutions for the electric field, the magnetic field behaves equivalently if not mentioned explicitly.

$$\left(\frac{\partial^2}{\partial\phi^2} + m^2\right)\mathbf{G}(\phi) = 0 \tag{2.39a}$$

$$\left(r^2\frac{\partial^2}{\partial r^2} + r\frac{\partial}{\partial r} - (n_{\text{eff}}^2 - n^2(r))k^2r^2 - l^2\right)\mathbf{F}(r) = 0 \tag{2.39b}$$

The first equation can be solved by:

$$G(\phi) = \mathcal{E}_\phi \exp(\imath m\phi) \tag{2.40}$$

This directly implies that m is an integer as the condition $G(\phi{=}0) = G(\phi{=}2\pi)$ has to be fulfilled and, therefore, l is an integer too.

The second equation (2.39b) has the form of Bessel's differential equation [31]. If the factor $(n_{\text{eff}}^2 - n^2(r))k^2$ is negative, the result is identical to the ordinary Bessel's differential equation whereas, if the factor is positive, the modified Bessel's differential equation has to be considered. In the core region with $n_{\text{eff}} < n_2$, the ordinary Bessel's differential equation has two solutions for each l, called 1st and 2nd kind. The solution of the 2nd kind diverges for small arguments and is, therefore, discarded as unphysical. In the same way, the modified Bessel's differential equation in the cladding $n_{\text{eff}} > n_1$ has two solutions for each l, where the 1st kind diverges for large arguments and is therefore rejected as well. The two non-diverging solutions are:

$$\begin{aligned} J_l(x) &= \frac{1}{\pi}\int_0^\pi \cos(n\tau - x\sin(\tau))\,d\tau \qquad \text{for } l \in \mathbb{Z} \qquad \text{ordinary, 1st kind} \\ K_l(x) &= \frac{\pi}{2}\frac{\imath^l J_{-l}(\imath x) - \imath^{-l}J_l(\imath x)}{\sin(l\pi)} \qquad \text{for } l \in \mathbb{Z} \qquad \text{modified, 2nd kind} \end{aligned} \tag{2.41}$$

At this point, the modified propagation constants h and q can be introduced, simplifying the expressions in a way consistent with the literature such as [33]:

$$(n_{\text{eff}}^2 - n^2(r))k^2 = \begin{cases} h^2 & \text{for } r < a \\ q^2 & \text{for } r > a \end{cases} \tag{2.42}$$

$$\text{with: } h = \sqrt{n_2^2 - n_{\text{eff}}^2}k \qquad \text{and} \qquad q = \sqrt{n_{\text{eff}}^2 - n_1^2}k \tag{2.43}$$

Including equations (2.40) and (2.39b) one can find solutions for (2.37a) and (2.37b) of the kind:

$$E_{l\,m}(r,\phi) = \begin{cases} \mathcal{E}_1 J_l(hr)\,\exp(m\phi) & \text{for } r < a \\ \mathcal{E}_2 K_l(qr)\,\exp(m\phi) & \text{for } r > a \end{cases} \tag{2.44}$$

A general field distribution consists of a superposition of modes:

$$\mathbf{E}(r,\phi) = \sum_m \sum_l E_{l\,m}(r,\phi) \tag{2.45}$$

Higher order modes fulfilling the exact analytical equation are indicated by m, the azimuthal mode number (2.39a) and l, the radial mode number (2.39b). Additionally, they are labeled according to their polarization as either hybrid modes HE, EH or pure TM and TE. The modes TE_{01} and TM_{01} are fully rotational symmetric (as $m = 0$ implies). Here, the main electric field polarization component is either radial or azimuthal. In both cases, the mode is doughnut-like, with a node in the center and, therefore, are intuitively not the fundamental modes. Together with the EH_{11} mode, these modes correspond to the LP_{11} mode. The hybrid mode HE_{11} has a high intensity in the waveguide center and dominating linear polarization. This mode is the fundamental mode and corresponds to the fundamental mode in the linear polarization approximation LP_{01}. There exists a cut-off condition for all these modes like in the one-dimensionally confined waveguide except for the fundamental mode HE_{11} [34].

The following derivation is concerned with a single-mode waveguide only. The discussion will, therefore, be restricted to the fundamental mode HE_{11}. In analogy to the treatment in the one-dimensional case (section 2.2), the other field components can be calculated based on Maxwell's equations, and the continuity relations at the interfaces (2.24) can be used to find the effective refractive index n_{eff} as function of a and the refractive indices. n_{eff} and the propagation constant $n_{\text{eff}}k$ can then be found as solutions to the transcendental equation (please note, h and q are functions of $n_{\text{eff}}k$) [33]:

$$\frac{J_0(ha)}{haJ_1(ha)} = -\frac{n_2^2+n_1^2}{2n_2^2}\frac{K_1'(qa)}{qaK_1(qa)} + \frac{1}{h^2a^2} - \sqrt{\left(\frac{n_2^2-n_1^2}{2n_2^2}\frac{K_1'(qa)}{qaK_1(qa)}\right)^2 + \frac{n_{\text{eff}}^2}{n_2^2}\left(\frac{1}{q^2a^2}+\frac{1}{h^2a^2}\right)^2} \tag{2.46}$$

A solution of this transcendental equation is shown exemplary in a plot of n_{eff} against the waveguide radius a as dispersion-like diagram in figure 2.6.

The radial function $F(r)$ is given by:

$$\mathbf{E}(r,\phi,z,t) = \mathbf{F}(r)\exp(\imath(-\omega t + n_{\text{eff}}kz \pm \phi)) \tag{2.47}$$

As discussed in [33], the fundamental mode in radial coordinates is a superposition of $E_{l=0,m=\pm1}$ and $E_{l=2,m=\pm1}$. The radial function $\mathbf{F}(r)$ for this superposition has the three components in cylindrical coordinates:

$$F_r(r) = \begin{cases} -\imath A\frac{n_{\text{eff}}k}{2h}\left((1-s)J_0(hr) - (1+s)J_2(hr)\right) & \text{for } r < a \\ -\imath A\frac{n_{\text{eff}}k}{2q}\frac{J_1(ha)}{K_1(qa)}\left((1-s)K_0(qr) + (1+s)K_2(qr)\right) & \text{for } r > a \end{cases} \tag{2.48}$$

$$F_\phi(r) = \begin{cases} A\frac{n_{\text{eff}}k}{2h}\left((1-s)J_0(hr) + (1+s)J_2(hr)\right) & \text{for } r < a \\ A\frac{n_{\text{eff}}k}{2q}\frac{J_1(ha)}{K_1(qa)}\left((1-s)K_0(qr) - (1+s)K_2(qr)\right) & \text{for } r > a \end{cases} \tag{2.49}$$

$$F_z(r) = \begin{cases} AJ_1(hr) & \text{for } r < a \\ AK_1(qr) & \text{for } r > a \end{cases} \tag{2.50}$$

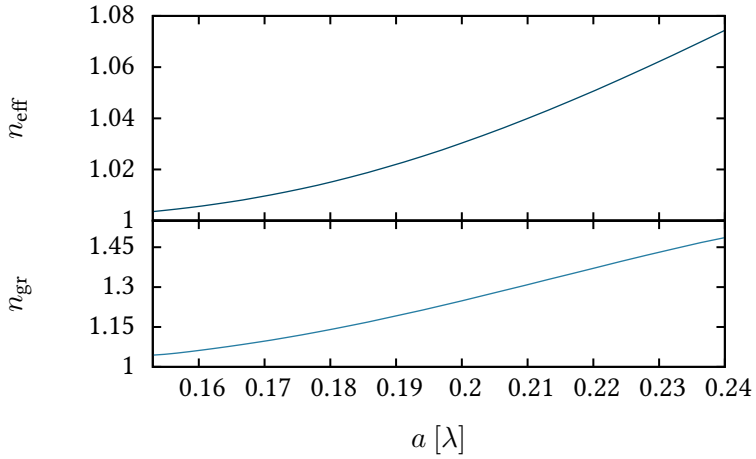

Figure 2.6.: Dispersion of a cylindrical waveguide with core $n_2 = 1.45$ and cladding $n_1 = 1$. In the upper plot the effective refractive index is plotted based on the transcendental equation (2.46) for different core radii a. The group index (lower plot) is calculated from the effective refractive index according to (2.32) and is used in the calculation of the emission enhancement factor α. The range of relative waveguide widths has been chosen to cover the features of the experimental realization.

with:

$$s = \frac{(qa)^{-2} + (ha)^{-2}}{\frac{J_1'(ha)}{haJ_1(ha)} + \frac{K_1'(qa)}{qaK_1(qa)}} \tag{2.51}$$

This intensity distribution is illustrated in figure 2.7 for as specific set of parameters which is chosen in accordance to the experiment (chapter 4). A representation of such a mode in Cartesian coordinates as well as in Cartesian field components can be found in [33].

The fundamental mode HE_{11} (shown in 2.7) is often referred to as quasi linear polarized, since one electric field component is dominating. For this discussion, this dominating component can be chosen to be E_x (in this case, Cartesian coordinates are useful as they resemble the symmetry implied by $m = 1$). Now, comparing the situation with one-dimensional waveguides, due to the continuity of $E_{\|}$ at an interface like in the y-direction ($x = 0$), the electric field profile E_x should be similar to the analytical results shown for E_y of TE-mode in planar waveguides (Fig.: 2.3). Analogously, from the discontinuity of $E_{\perp}$, a TM-like (figure 2.4) behavior of E_x in x-direction at $y = 0$ can be expected. For the combined profile, the value at the origin $x = 0$, $y = 0$ has to be identical. This directly shows that even for two-dimensional waveguides, the evanescent field intensity in the direction of the main polarization (here $\hat{x}$) can be much higher than the field inside the core region. Then, E_y is zero in the x-direction as the TM-mode has no component parallel to the interface. For the y-direction, as the TE-mode has no component perpendicular to the interface, E_y is again zero. The third component, E_z, is strong near the surface in x similar to the situation with the TM-mode, but with a zero-crossing at the center. E_z vanishes completely in the y-direction, as does the TE-mode. Motivated by the ambivalence

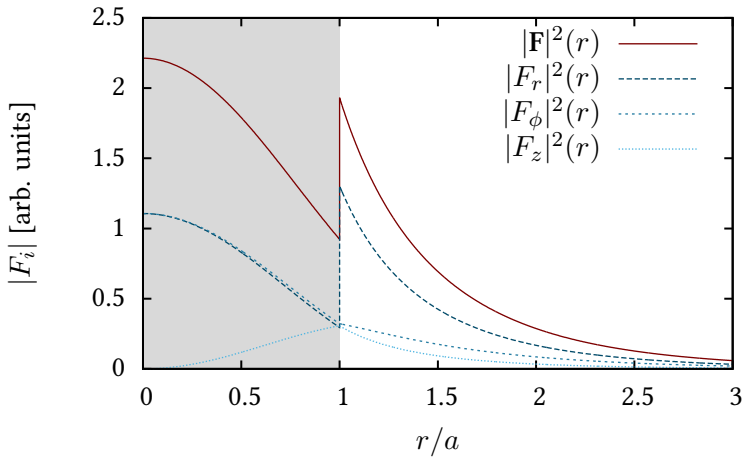

Figure 2.7.: The radial intensity profile (HE_{11}) of a single-mode nanofiber as predicted by equations (2.48), (2.49), (2.50) for the radial, azimuthal, and tangential components, respectively. The modulus squared of each component of $\mathbf{F}(r)$, the radial dependency of $\mathbf{E}(r)$ is shown as well as their square sum. The values used for this plot are inspired by the experiment shown in chapter 4 and are chosen as follows: $a = 0.195\lambda$, $n_2 = 1.45$, and $n_1 = 1$. This results in the parameters $n_{\text{eff}} = 1.03$, and $s = -0.96$. The gray shaded area indicates the nanofiber core region.

of a mode showing TE and TM-like properties, these modes are called hybrid modes (in this case the fundamental mode HE_{11}).

The knowledge of the mode-profiles and their dependence on the radius a can be used to design a nanofiber with optimized coupling to e.g. a broadband quantum emitter like the nitrogen vacancy center in diamond, which is discussed in detail in chapter 3.

2.3.2. Dipole Coupling to a Nanofiber

In section 2.1, the basic formulas, needed to calculate the emission enhancement factor α from a known electric field profile $\mathbf{E}(x, y)$ of a certain mode, have been derived. This calculation can now be applied to the mode profile found for the nanofiber, which allows to determine α and β [35].

The system, which is going to be discussed here, is a dipole placed on the surface of the nanofiber. This choice is based on the experimental realization scheme where the quantum emitter is placed on the surface of the waist of a tapered optical fiber which is surrounded by air (for details see chapter 4). TOFs are made of standard single-mode silica fibers and, therefore, also the nanofiber material is silica. The refractive indices from the actual experiment are used, defining a fused silica core with the refractive index of $n_2 = 1.46$, surrounded by air $n_1 = 1$. The fiber radius a is the only free parameter left, and therefore, be measured in units of the wavelength λ. Doing so, the wavelength dependence of the coupling parameters and their scaling with the fiber radius a can be visualized within a single graph.

The knowledge of the nanofiber mode allows for the analytical derivation of the emission enhancement factor α. From equation (2.6) and (2.47), the effective mode area for a dipole positioned above the fiber surface with a variable distance d to the surface and a dipole orientation parallel to field component j of the respective mode is given by:

$$A_{\text{eff},j}(d) = \frac{2\pi \int n^2(r)|\mathbf{F}(r)|^2 r \mathrm{d}r}{|F_j(a+d)|^2} \tag{2.52}$$

Inserting this expression of the effective mode area into equation (2.10), finally gives the desired emission enhancement factor:

$$\alpha_j(d) = \frac{1}{8\pi} n_{\text{gr},j} \frac{\sigma_A |F_j(a+d)|^2}{\int n^2(r)|F_j(r)|^2 r \mathrm{d}r} \tag{2.53}$$

Here, the dipole orientation with respect to the electric field $\langle \hat{\boldsymbol{\epsilon}} \cdot \hat{\boldsymbol{\mu}} \rangle^2$ will not be treated as a scalar product, but replaced by separate solutions for the three different dipole orientations $j = r, \phi, z$.

The analytical expression for the group index n_{gr} from the transcendental equation (2.46) is linearly interpolated based on $n_{\text{eff}}(\lambda)$ which is calculated at discrete wavelengths λ (see equation (2.32)). This group index is plotted against the waveguide radius a in figure 2.6.

For a vacuum-clad nanofiber with a core refractive index of $n_2 = 1.46$, the emission enhancement factor α can be above 0.7 for two of the three dipole orientations. With this value, it can be expected that about 70% of the total emission rate in an isotropic medium can be expected in the waveguide mode of the coupled system ($\Gamma_{\text{wg}} \approx 0.7\Gamma_{\text{iso}}$). The maximum coupling is achieved with a fiber radius of about $a = 0.23\lambda$, which is consistent with the analysis of Waken et al. [36]. The region for maximum coupling is broad, which can be interpreted as a tolerance criterion for the fabrication of the fiber or a broadband coupling with respect to the wavelength. The waveguide-width dependency of α is shown in figure 2.8.

As discussed in the previous section, the experimental determination of the emission enhancement factor is unpractical. However, the coupling efficiency β can be obtained and will therefore be used to compare the experiment with theoretical results.

The coupling efficiency is expressed by the factor β, whose determination requires the knowledge of the emission rates into the waveguide modes and into free space in presence of the waveguide. To calculate the emission rate into free space modes, these modes have to be determined first, but, since the nanofiber modifies the free space emission pattern these modes are difficult to calculate. Using an analytical derivation, Klimov et al. [35] were able to calculate the radiative decay-rates into the fiber as well as into free-space modes. These calculations were performed for different refractive indices of the nanofiber and as function of the fiber radius a. However, none of the refractive indices discussed in this publication match the index of the fiber used in this experiment. Instead of the analytical calculations, a numerical three-dimensional Finite-Difference-Time-Domain method [37] is used to simulate the emission of the dipole on the nanofiber which allows to extract β. This procedure has the advantage of being very flexible in the design of the structure. For instance, a diamond nanocrystal can easily be included in the simulations, modeled as a dielectric sphere surrounding the dipole.

The FDTD-simulation for a time-independent emission source results in a stationary power density distribution in the three dimensional simulation volume (a two-dimensional cut along

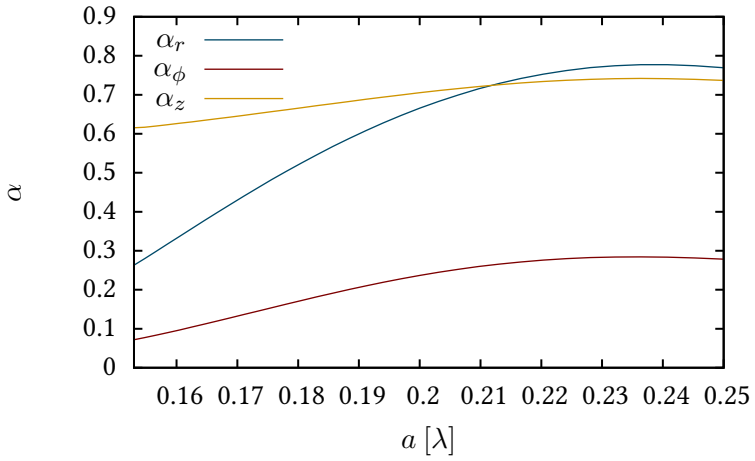

Figure 2.8.: Calculated emission enhancement factor α as function of the waveguide radius a for the three main dipole orientations: radial to the waveguide α_r, tangential α_ϕ, and parallel α_z. The electric fields at the position of the emitter as well as the effective mode area A_{eff} were obtained using equations (2.48), (2.49), (2.50), the group index n_{gr} follows graph 2.6.

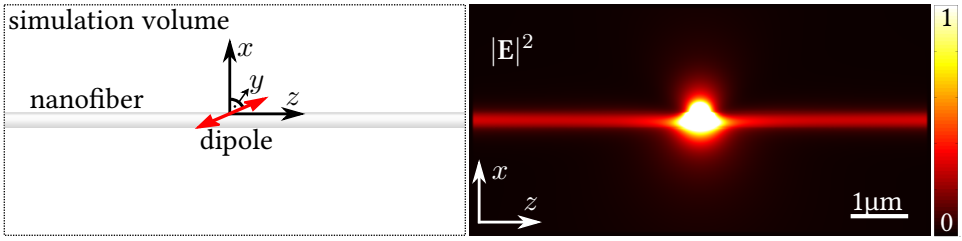

Figure 2.9.: Exemplary intensity map (right) of a plane cut through a cylindrical waveguide with an emitting dipole on top such as illustrated on the left. The intensity map (high value: white, low value: black) is created via 3-dimensional FDTD-simulations [37] of a volume of $4 \times 4 \times 8\,\mu\text{m}^3$. The cut plane ($x$-$z$-plane) shown in the right is parallel to the waveguide and centered ($y = 0$). The orientation of the simulated dipole is parallel to the fiber surface but diagonal between z and y. The fraction of light being coupled to the nanofiber is indicated by the constant intensity (non-diverging) in the fiber to the left and to the right.

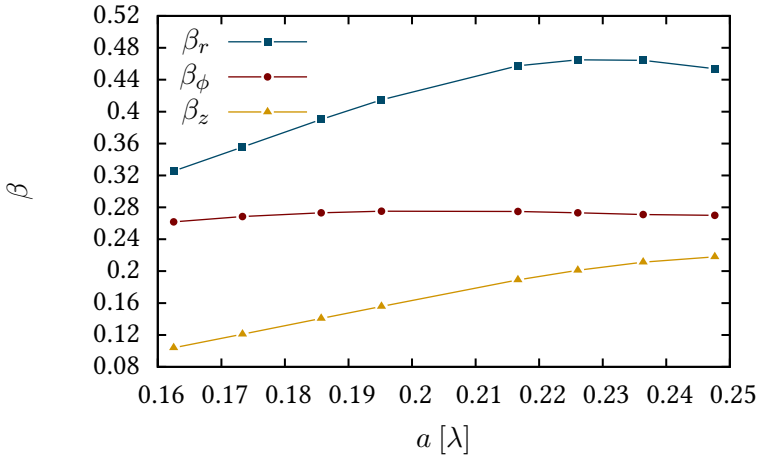

Figure 2.10.: Coupling efficiency β of a dipole placed on top of a cylindrical waveguide with refractive index of 1.46 and radius a. These values have been obtained from FDTD-simulations such as depicted in figure 2.9. β is shown for the three different dipole orientations, radially (r), azimuthal (ϕ) and parallel (z) to the fiber axis.

the center of the nanofiber is shown in 2.9). The size of the simulation volume has been chosen as a compromise of computation time, simulation accuracy, and the decay length of near field effects.

The total emitted power P_{tot} of the dipole can be extracted from the summation via the power of each grid point of the outer shell P_{x_i,y_j,z_k} of the simulation volume. Thereby, the projection of the spherical emission pattern onto the rectangular surface of the simulation volume has been compensated for. Here, the simulation volume has a high aspect ratio. The power in the waveguide mode can be well approximated by the summation of the power of the two end faces of the simulation volume. The fraction of the total power to the guided power is equal to the fraction of the total emission rate Γ_{rad} to the emission rate into the guided mode Γ_{wg} and therefore equal to β. It has to be noted, that FDTD-simulations are not able to determine the absolute value of Γ_{rad}, Γ_{free} or Γ_{wg} but only their mutual relative values [38].

The FDTD-simulations[5] predict a coupling efficiency with a maximum above 45% for a dipole oriented radially β_r. This peak is found for a fiber radius of $a = 0.23\lambda$, which is at the same position as the peak of the emission enhancement factor α_r. The coupling efficiency β_ϕ of the a tangentially oriented dipole is nearly constant (around 26%) in the range $a = (0.16 \ldots 0.25)\lambda$. A dipole oriented along the propagation direction z is expected to experience the lowest coupling efficiency ($0.1 < \beta_z < 0.24$) within the simulated range of $a = (0.16 \ldots 0.25)\lambda$.

The determination of α and β allows to discuss their quotient, the expected change in the

[5]In the FDTD-simulations, the dipole is located slightly ($0.08a$) above the surface of the nanofiber. This distance is chosen to account for the size of the dielectric particle hosting the dipole in the experimental part. Additional simulations are performed hosting the dipole in a dielectric sphere of $0.16a$ (20 nm) to represent the diamond nanocrystal. These simulations showed no significantly different results from the ones without the dielectric sphere.

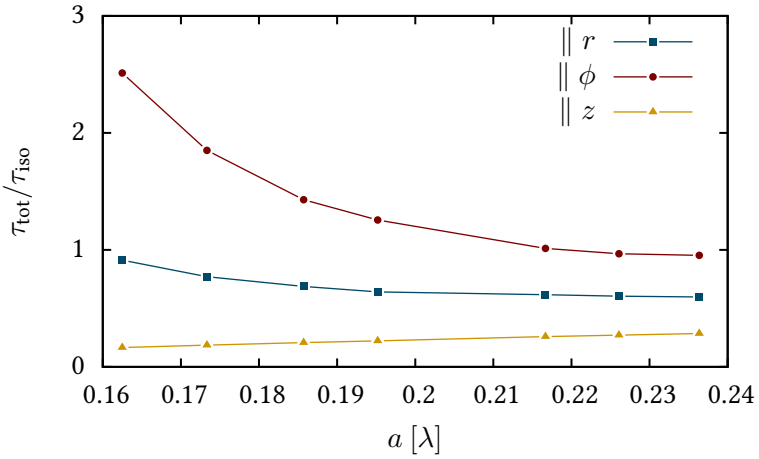

Figure 2.11.: Expected change of the emitters total lifetime as a function of the nanofiber radius a.

exited state lifetime $\tau_{tot}/\tau_{iso} = \beta/\alpha$ for the different orientations of the dipole with respect to the nanofiber (see figure 2.11). Here, for two ($\|_r$, $\|_z$) of the three main dipole orientations a relative lifetime τ_{tot}/τ_{iso} below one is found (see figure 2.11). Such shortening of lifetime due to the presence of the fiber indicates an enhancement of the total radiative decay rate and a Purcell-effect can be expected (see also section 2.1). However, the azimuthal dipole orientation ($\|_\phi$) shows an increased lifetime for decreasing core radii. As the coupling efficiency β_ϕ is nearly constant, this indicates suppression of spontaneous emission into the fiber and into free space modes at the same time.

In summary, the discussion of the interaction between a light field and a two-level quantum emitter, leads to expressions for the relative emission rates. From these rates, the emission enhancement factor α and the coupling efficiency β can be derived. The emission enhancement α is a measure of the emission rate which can be expected to be emitted into the waveguide mode. The coupling efficiency β is the probability of an emitted photon to be coupled into the waveguide mode. However, β is also the probability of the two-level-system to absorb a photon guided by the waveguide. Already the most basic waveguiding dielectric structures, the one-dimensional slab waveguide shows an evanescent field, mode confinement, mode cut-off and waveguide dispersion. In such a structure, there exist two sets of modes, the transversally electric (TE) and transversally magnetic (TM) modes. In contrast, the cylindrical waveguide features the fundamental mode HE_{11}, which is a hybrid of TE and TM-modes showing properties of both types. This hybrid nature is most prominent in highly confining waveguides such as the single-mode nanofiber with a high refractive index contrast. For this nanofiber, the expected emission enhancement parameter α and coupling efficiency β are calculated, for dipole orientations radially, azimuthal, and parallel to the fiber yielding values up to 45%, 26% and 24% respectively. The change in the photonic lifetime could be extracted from these values (figure 2.11), giving a hint about what emission rate changes can be expected. However, as

non-radiative decay channels might be modified by surface-, mechanical, or electrical effects, the modification of emission rates can be expected differ from these predictions in the actual experiment.

Before comparing these predictions with the results of the experimental realization, the following chapter introduces the nitrogen-vacancy center which will be used as single quantum emitter in the experiment.

3. The Nitrogen-Vacancy Center

In order to test the coupling to single mode waveguides experimentally, a single, isolated quantum emitter has to be chosen. Many different systems are possible candidates, such as atoms, quantum dots, dye molecules and fluorescent defect centers in crystals. The latter has been chosen for this work, due to their simple handling and their reliability. A very common fluorescent crystallographic defect center in the diamond crystal is the nitrogen vacancy center. In the past years, this system has gained much interest in the scientific world due to its huge variety of interesting properties [39]. Two of the most prominent features are its high photostability without blinking or photo-bleaching and its operation at ambient temperatures, rendering it a promising candidate for a stable and efficient single-photon source [40] (even commercially [41]). Another fascinating feature is that its spin can be initialized and read out optically. Via this spin, the NV-center is used to sense electric and magnetic fields [14, 42, 15], temperatures [13] and even detect and manipulate close nuclear spins [1], individually serving as a solid-state based multi-qubit system [43, 2]. For many of these applications, single NV-centers hosted in diamond structures, like AFM-tips [44] or nanodiamonds [45], can be used for extraordinarily high spatial resolution.

In the context of this work the nitrogen vacancy center is used as a single quantum emitter, therefore, this chapter will focus on its photon emission properties. The NV-centers used here are hosted in diamond nanocrystals which can be positioned deterministically on arbitrary structures using an AFM-based nanomanipulation technique. This chapter provides a short introduction to the basic photonic properties of the NV-center which will be useful in the subsequent chapters dealing with a coupled system of fluorescing nanodiamond and tapered optical fiber.

3.1. Structure of the Nitrogen-Vacancy Center

The nitrogen vacancy center is a defect in the diamond crystal lattice, consisting of a nitrogen atom substituting a carbon atom and an adjacent vacancy in the diamond lattice (illustrated in figure 3.1 a)). This complex has localized electronic states within the diamond band gap ($\Delta E = 5.45\,\mathrm{eV}$) of which some feature optically active transitions[1]. Starting with two levels, a triplet ground-state (^{3}A) and a triplet excited state (^{3}E) the level-structure will be gradually expanded within this section to explain the features relevant for this work.

The NV-center features two charge states, the neutral state (NV^0) and the negative charged state NV^- with an additional captured electron, which has been donated, for instance, by

[1] By optically active transition an electronic transition is meant which couples to the photon bath. The system can be excited while annihilating a photon or decay into a lower energy state while generating a photon. Here, energy differences are of interest which correspond to photons in the visible and near infra-red spectral range.

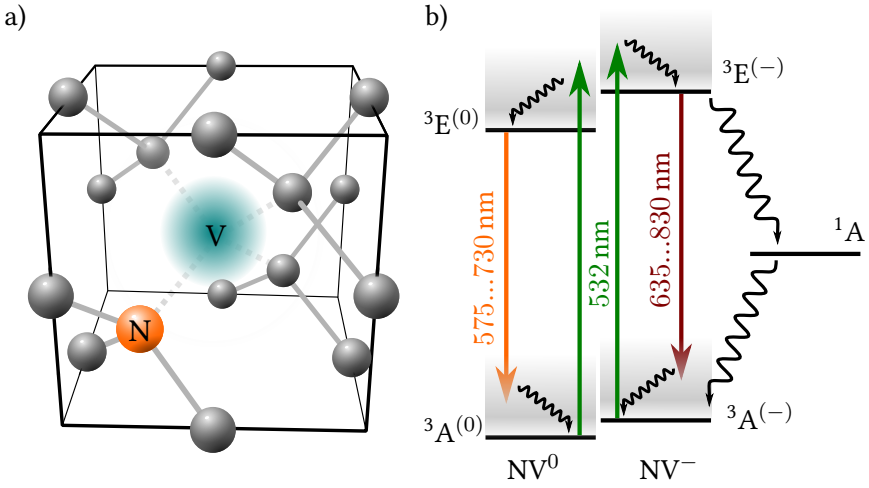

Figure 3.1.: a) Schematic of the nitrogen-vacancy center in the diamond crystal matrix. The gray dots indicate the carbon atoms of the diamond lattice. The substitutional nitrogen atom is indicated by N and the neighboring vacancy is denoted with V. b) Schematic of a simple model, describing the NV-center's level structure including the two charge states, indicated (NV^0 left and NV^- right). The horizontal black lines indicate the vibronic ground state of the electronic levels (electronic ground state ^3A, excited state ^3E, and shelving level ^1A). The gray shaded areas symbolize vibrational excitation bands. The straight arrows indicate photonic (radiative) transition, whereas the curled lines indicate a non-radiative transition. This level-structure is arranged within the band-gap generated by the diamond crystal lattice. The conduction band is located energetically above the excited levels and the valence band is below the ground states. Both bands are not shown here.

a close nitrogen atom. Both charge states feature an optical transition at the wavelengths $\lambda_{NV^0} = 575\,\text{nm}$, $\lambda_{NV^-} = 637\,\text{nm}$ (see figure 3.1 b)), respectively, and excited state lifetimes of few ten nanoseconds [46]. The NV^- can be ionized to its neutral charge state NV^0 by a two photon absorption process which first brings the center into its excited state ($^3E^{(-)}$) and second, excites the electron into the conduction band. The electron can then relax to the ground state, whereas the relaxation energy can ionize the complex to its NV^0 charge state via an Auger-process. In the reverse process of switching from the neutral to the negative charge state (NV^0 $\rightarrow$ NV^-), the NV^0 is excited ($^3E^{(0)}$) by absorbing a first photon. Then, an electron from the valence band can be excited by a second photon the ground ground state ($^3A^{(0)}$). Thereby, a hole is left in the valence band, which can diffuse. The cycling between both charge states is inevitable under continuous excitation [47, 48, 49]. As the charge state switching can only occur starting from the excited state, a continuous fluorescence emission can only be achieved with an excitation capable to excite both charge states. This can be realized by a single excitation laser at a wavelength within the interval where the absorption spectra of both charge states coincide (about $450 - 575\,\text{nm}$). This scheme is applied within this work by using an excitation laser at a wavelength of $532\,\text{nm}$. Alternatively, two lasers can be used, one to excite the neu-

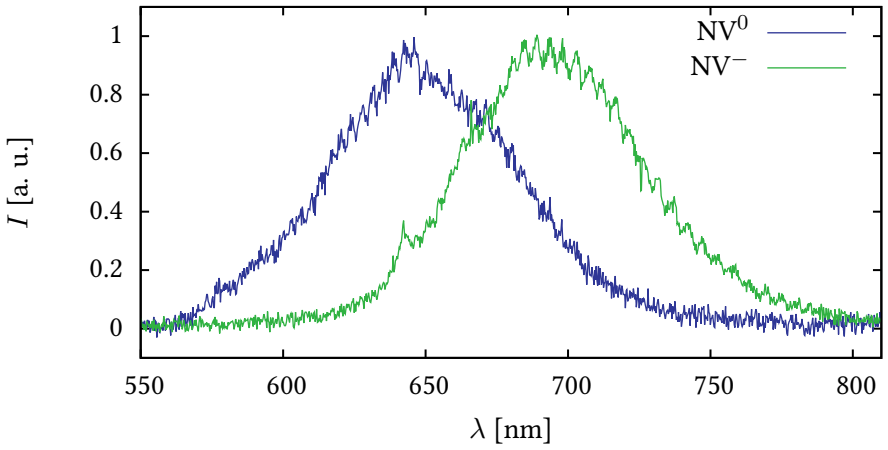

Figure 3.2.: Room-temperature spectra of two NV-centers, each hosted in a diamond nanocrystal. The blue spectrum shows emission dominated by the neutral charge state (NV^0) and the green spectrum indicates a major emission from the negative charge state (NV^-). At a wavelength of 637 nm, the zero phonon transition of the negative charge state shows a prominent peak. However, the zero phonon line (575 nm) of the neutral charge state is hard to distinguish from the noise. These two spectra are exemplary, as the most NV-centers show a mixture of both with variable pronounced features.

tral charge state NV^0 (wavelength: $400 - 575$ nm) and one exciting the negative charge state NV^- (wavelength $450 - 637$ nm) [48, 49]. Statistically, the center can undergo more emission cycles in one of the two charge states before the switching occurs and therefore the amount of emission of the two charge state can be very different (two examples are shown in figure 3.2).

The simple two-level scheme can be expanded by a third state (^{1}A), often called shelving level, which is coupled non-radiatively (figure 3.1 b)). This shelving level has a lifetime about an order of magnitude longer than the excited state [40]. The transition from this shelving state to the ground state is again non-radiatively. Even though the branching ratio is low, indications of such a level can be found in the second order correlation function of the emitted photons [40, 50]. This shelving level is included in the model of the second order correlation function (4.1) used in chapter 4 to prove the coupling of the single emitter to the tapered optical fiber. Due to such non-radiative decay channels, the correspondence of the excited state lifetime τ_{tot} to the maximum (saturated) photonic emission rate Γ_{sat} is lifted. Here, the quantum efficiency can be introduced as the ratio of the total decay rate $1/\tau_{tot} = \Gamma_{sat} + \Gamma_{nr}$ (the sum of radiative and non-radiative decay rates) to the photonic decay rate[2]: $QE = \tau_{tot}\Gamma_{sat}$.

The saturation of the photon emission rate Γ with excitation power P can simply be modeled

[2]The photonic decay rate is often referred to as the radiative decay rate expressing the disambiguation of radiative and non-radiative decay such as excitation of vibrational modes. However, to avoid confusion with the photon emission rates into guided Γ_{wg} and radiative free space Γ_{free} modes the total rate of emitted photons will be denoted as Γ_{rad} and the saturated emission rate $\Gamma_{sat} = \lim_{P\to\infty} \Gamma_{rad}$.

with a saturation excitation power P_{sat} and a saturation emission rate $\Gamma_{\text{sat}} = \lim_{P\to\infty} \Gamma_{\text{rad}}$:

$$\Gamma(P) = \Gamma_{\text{sat}} \frac{P}{P + P_{\text{sat}}} \tag{3.1}$$

In the experimental part, this model will be used to determine the saturation power sat from an excitation power series.

The nitrogen vacancy-complex features strong vibrational modes which include the three nearest neighboring carbon atoms [51]. The lifetimes of these vibrational levels are on the scale of picoseconds resulting in an energetic broadening of the transitions. The resulting emission spectrum of such a NV-center features a zero phonon line combined and a broad continuous vibronic sideband of overlapping vibrational levels, which is highly dominant at ambient temperatures. This forms the typical spectral emission pattern which allows to identify NV-centers. The absorption spectrum is of similar structure: Due to the similarity of the vibronic ground and excited state and the Franck-Condon principle, absorption and emission spectrum can be approximated as one being mirror symmetric to the other with respect to the zero-phonon line [52, 53]. This vibronic absorption sideband allows, therefore, for far off-resonant excitation with standard lasers. Both charge states show similar vibronic modes and therefore show very similar absorption and emission spectra, but shifted in energy.

The NV-center has a fixed symmetry axis connecting the nitrogen atom and the vacancy. Within the diamond crystal, this axis can be oriented along one of four orientations. The absorption and emission dipoles are perpendicular to the symmetry axis. Therefore, it is convenient to model this system as two perpendicularly oriented dipoles. In the experimental part 4, logging the emission rate while rotating the polarization of the excitation will be used to determine the angle between of the dipole plane and the image plane.

3.2. Fluorescing Nanodiamonds

An interesting feature of the NV-center is, that this complex can be stable and fluorescent in diamond nanocrystals of a few tens of nanometers and even down to $5\,\text{nm}$ [54]. Thereby, the quantum emitter is securely embedded inside a solid state crystal matrix, but can be moved mechanically and brought very close to any photonic structure. Such fluorescent diamond nanocrystals can be created by milling of larger diamond particles from a high pressure, high-temperature (HPHT) process [55], or by detonation [56]. Such diamond nanocrystals are produced on a commercial scale as polishing suspensions [57, 58]. However, in this context the content of nitrogen and NV-centers is irrelevant for polishing process and therefore mostly unknown. For the usage as hosts for defect centers, such diamond nanoparticles can be irradiated with electrons or ions and annealed to achieve the desired concentration of NV-centers [55]. Recently, efforts are made to commercialize the production of fluorescing nanodiamonds with a defined NV-center concentration, suitable for quantum optical experiments [59]. The diamond nanocrystals used in this experiment stem from an untreated polishing suspension sold by Microdiamant [57] (mean diameter about $16\,\text{nm}$ [60]), showing a reasonable amount of diamond nanocrystals hosting single NV-centers (about 1% [60]).

NV-centers in diamond nanocrystals maintain most of their bulk-properties, however, some of them show blinking and photo-bleaching. These effects are well known in the literature

[61, 62] and attributed to surface defects and modifications [63, 64]. With systematic precharacterization, stable single NV-centers hosted in nanodiamonds can be located easily. The precharacterization, as well as the AFM-based nanomanipulation technique used to place the diamond nanocrystal deterministically are presented in section 4.

In the discussion of the coupling of a dipole to a waveguide structure (chapter 2.1), it has been found that the surrounding of an emitter can have a strong impact on its radiative lifetime [3]. In this context, also a modification of the lifetime of an emitter situated in a nanocrystal instead of a bulk crystal environment can be expected. A lifetime modification is caused by the glass substrate, on which the diamond nanocrystals are placed on during their experimental characterization.

In the limit of a large nanocrystal size ($\lambda \ll r$) the emission rate of a dipole in the nanocrystal Γ_{np} approaches the value found for the bulk Γ_{bulk}. Particles with sizes on the order of the emitted wavelength pose an intermediate regime. Mie-resonances in the particle can either suppress or enhance the emission rate to a great amount. This effect highly depends on the position of the emitter inside the particle as well as on the exact size and the detailed shape (as discussed for europium ions in polystyrene colloids in [65]). If the size of the nanocrystals is smaller than the wavelength ($\lambda \gg r$) these resonances vanish and the limit of an infinitesimal small particle (Rayleigh limit) is a valid approximation. As the diamond nanocrystals, which are used in this thesis, have diameters far below the emission wavelength of the incorporated NV center, this Rayleigh regime has to be considered. The emission rate of the emitter inside of the nanoparticle Γ_{np} can be related either to the bulk emission rate Γ_{bulk} or the vacuum emission rate $\Gamma_{\text{vac}} = \Gamma_{\text{bulk}}/n$. In a general form, their relation can be expressed as [66]:

$$\Gamma_{\text{np}} = n^p \, l^q(n) \, \Gamma_{\text{bulk}} \tag{3.2}$$

The nanoparticle has the refractive index n and $l^q(n)$ governs local electric field corrections. These corrections and therefore the function $l(n)$ and the exponents p and q are subject of ongoing debate in the literature. Several solutions have been proposed which are derived from different models [67]. But, it has been also pointed out that each model could be confirmed experimentally.

Beveratos et al. argue, that a diamond nanocrystal has the same dielectric properties as diamond-bulk and, therefore, the local field corrections l do not influence the NV-center [68]. Additionally, they found the model (3.2) representing their measured data well with $p = 1$. According to this argument, the lifetime of the optical transitions of NV-centers in nanodiamond is only modified linearly by the refractive index change from the absence of the bulk crystal. In the experiment the diamond nanocrystals are usually placed on a fused silica substrate. Here, a simple mean model can be used to calculate the expected radiative lifetime change $\tau_{\text{sub}}/\tau_{\text{free}}$, introduced by the dielectric half-space [68, 69]:

$$\frac{\tau_{\text{sub}}}{\tau_{\text{free}}} = \frac{2}{n_{\text{sub}} + 1} \tag{3.3}$$

This value is about 81% for a glass substrate with $n_{\text{sub}} = 1.46$. Including the simple model of negligible field corrections l but correction for the glass substrate, a mean lifetime of $22\,\text{ns}$ is calculated, which could be verified experimentally [68]. As expected by the model, a dependency on the crystal size has not been found. However, the influence of the substrate might

vary with the orientation of the dipoles with respect to the substrate. This can be an explanation of the variance in lifetime of ± 4 ns which has been reported [68]. The quantification of the lifetime is not part of this work, however, six single NV-centers hosted by nanocrystals of the same solution as used in the following experiment have been analyzed with pulsed resonant excitation on a fused silica substrate. This pulsed excitation lifetime measurement revealed a mean lifetime of 25 ns with a standard deviation of 9 ns consistent with the literature [68].

4. Coupling a Single NV-center to a Tapered Optical Fiber

The theoretical analysis in section 2.3 predicts the possibility of efficient coupling of a quantum emitter to a nanofiber. It has been found that the strong confinement of the optical mode of a nanofiber results in a strong evanescent field surrounding the fiber. A two-level system placed inside this evanescent field can experience efficient coupling to the guided mode. Due to this coupling, a fraction of its radiative emission is coupled directly to the guided mode of the nanofiber (see section 2.3). In this chapter, the experimental implementation and characterization of such a coupled system will be demonstrated. The nanofiber is realized by the waist of a tapered optical fiber (TOF) (see Fig. 4.1) the evanescent coupling to a quantum emitter is increased by the field enhancement of a confined mode in the nanofiber. To benefit from the enhanced field the single nitrogen-vacancy center, hosted in a diamond nanocrystal, is placed on the surface of the TOF. Major aspects of this chapter are published in [70].

Until now, evanescent coupling of fluorescence photons to a single guided mode of a TOF has been achieved for various solid state quantum emitters [71, 72, 73, 74], molecules [75], and laser-cooled atomic vapors [76]. To bring these emitters into the strong evanescent optical field at the surface of the nanofiber several, non-deterministic deposition techniques like dip-coating [71, 72], picoliter-dispensers [73, 74], and optical surface traps [77] have been applied. However, for real applications in quantum information science, for instance the photonic quantum-bus mediated coupling of NV-centers in a lattice [78], deterministic positioning of single solid state quantum emitters onto the submicron waist of a TOF with nm position control is required.

After an introduction to the assembly procedure of the system based on a pick and place procedure of the diamond nanocrystal, the coupling is verified. Then, the experimental result of the coupling efficiency β is determined and compared with the value obtained from the simulation.

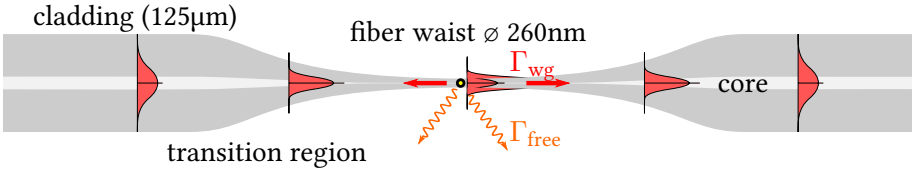

Figure 4.1.: Schematic of evanescent coupling of single photons emitted by a single nitrogen vacancy center (hosted in a diamond nanocrystal) to a single guided mode of a tapered optical fiber (TOF). Mode profiles are sketched in red in order to illustrate the mode conversion in the transition region. (Not to scale)

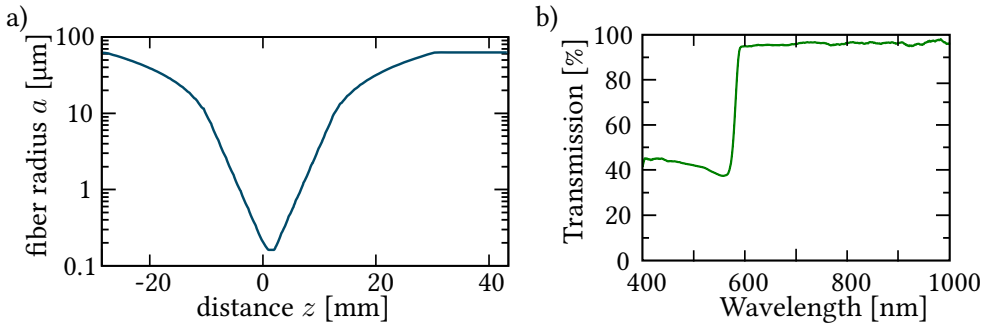

Figure 4.2.: a) Designed radius of the TOF as function of the propagation length z. This design was developed by Ariane Stiebeiner [34]. b) Measured transmission spectrum of a TOF, which has been produced in exactly the same way as the one used in the experiment. The transmission spectrum has been recorded immediately after the fabrication process. After several months in a transport case, a reduced transmission has been found, showing a spectral λ^4-characteristic [80], which is consistent with the model of Rayleigh scattering at dust particles attached to the tapered region.

4.1. Tapered Optical Fiber

The tapered optical fiber (illustration in figure 4.1), is a standard optical single-mode fiber which has been drawn down to a waist diameter of 260 nm with a fiber-pulling-rig [79, 20]. The thickness profile of the transition region (see figure 4.1) is designed to provide high transmission for the broad wavelength range of the NV-centers emission. The design of the transition is sophisticated, as it is connecting a strongly confining single-mode cylindrical waveguide with a large refractive index contrast, to a standard single-mode fiber. The single-mode fiber is single-mode regarding its core, but the cladding itself is also a high-order multi-mode waveguide. These cladding modes are usually unwanted and regarded as loss-modes. Therefore, in the transition region of the tapered fiber system the goal is to couple the single-mode of the nanofiber exclusively to the fundamental mode of the single-mode fiber. This can be achieved by using the adiabatic theorem, stating roughly that, for an axial symmetric transition, the fundamental mode of one waveguide is coupled exclusively to the fundamental mode of the other waveguide, if the transition is smooth enough (see section 5.2.2). Due to this adiabatic theorem, but also caused by the fabrication process, TOFs always have a certain length (several millimeters). A detailed description of the design parameters, the fabrication and characterization can be found in [34]. The TOFs used in this experiment show an initial transmission of more than 94% for wavelengths ranging from 600 nm to about 1 µm. The measured transmission spectrum of a TOF, which has been produced in exactly the same way as the one used in the experiment, is shown in figure 4.2 b).

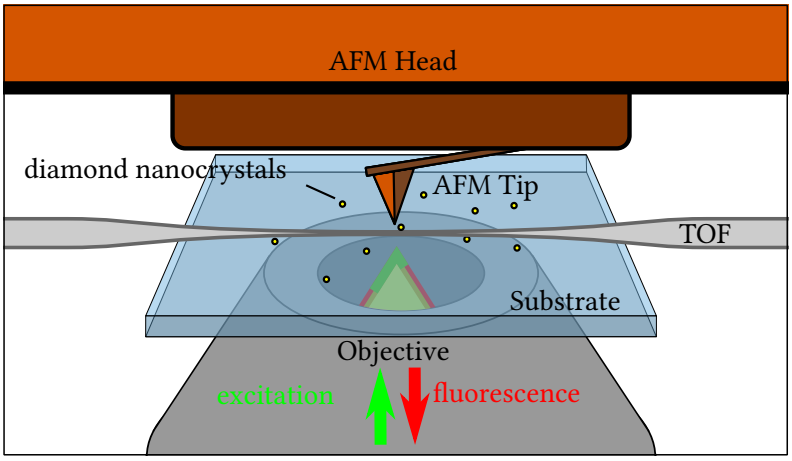

Figure 4.3.: Schematic diagram of the sample stage of the experimental setup. An inverted optical confocal scanning microscope (objective depicted at the bottom) is used to analyze the fluorescence properties of individual diamond nanocrystals. From the top, an atomic force microscope (AFM) is employed for in-situ nano-manipulation of individual crystals. This configuration allows the positioning of a diamond nanocrystal in the apex of the tapered optical nanofiber (TOF). At the same time, the confocal microscope can be used to monitor the nanomanipulation procedure. More details about the experimental setups are presented in appendix B.

4.2. Hybrid Microscope

The setup (a schematic of the sample stage is presented in figure 4.3) is designed to cover the whole experimental procedure: locating and characterizing individual NV-center candidates, assembling the coupled TOF-nanodiamond system, and investigating its properties. The optical characterization of the NV-centers is conducted with a confocal optical scanning microscope. This optical microscope is combined with an atomic force microscope (AFM) to allow in-situ nanomanipulation of the fluorescing diamond nanocrystals. The combination of both devices allows to monitor the assembly of the coupled system of TOF and nanodiamond. After a successful composition, its characterization can be performed within the same experimental setup.

The confocal microscope (detailed sketch can be found in appendix B) is constructed to locate and characterize single nitrogen-vacancy centers based on their fluorescence signal. The NV-centers are excited to their phononic absorption sideband using a continuous-wave laser at a wavelength of 532 nm. This excitation light is focused onto the diamond nanocrystals with a microscope objective (NA=0.75). The same objective also collects the fluorescence signal from the sample, which is then separated from the excitation light with a dichroic mirror. In the confocal path, a voice-coil scanning mirror is used to vary the deflection angle of the confocal path computer-controlled. This variation of the deflection angle is translated by a 4f-telescope into a displacement of the focal spot of the objective within the image plane. The fluorescence light transmitted by a dichroic mirror is focused into a single mode fiber. This fiber, thus, acts

as a spatial mode filter which not only increases the signal to noise ratio, but also allows easy switching of the analysis apparatus. For example, an avalanche photodiode (APD) can be connected to count collected fluorescence photons, allowing to record fluorescence intensity maps. Analyzing such maps, fluorescing particles like diamond nanocrystals hosting NV-centers can be localized for further investigations. Instead of the avalanche photodiode, a spectrometer can also be attached to the fiber output of the confocal microscope. This spectrometer can help to distinguish NV-centers from other fluorescing objects. Another analysis device applied here is the Hanbury-Brown and Twiss-interferometer [40], which can be used to determine the second-order correlation function[1] of the collected fluorescence photons. If the fluorescence is generated mainly by a single quantum emitter, this is indicated by a clear anti-bunching dip in this second-order correlation function. With these analysis devices and methods, single NV-centers suitable for the experiment can be identified and characterized.

The hybrid microscope is formed by combining this confocal microscope with an atomic force microscope (AFM). This AFM (details in the appendix, section B and [81]) is placed on top of the confocal microscope with the AFM-tip facing the microscope objective (sketched in figure 4.3). With this arrangement the AFM can be operated while the confocal microscope still has full optical access. As both, the AFM and the confocal microscope can be used simultaneously, the repetition cycle can be short and the nanomanipulation process can be monitored in-situ.

4.3. Assembly of the Coupled System

The on-demand highly accurate picking and placing of single diamond nanocrystals is achieved using a recently introduced nanomanipulation technique [82]. With the hybrid microscope the topography (see Fig. 4.4, b) and the respective optical response (see Fig. 4.4, c) of NV-centers in diamond nanocrystals are monitored before, during, and after assembly (see Fig. 4.4, from left to right).

First, the diamond nanocrystals are distributed on a glass substrate by spin-casting the suspension of nanocrystals in ethanol. Second, diamond nanocrystals hosting single NV-centers are identified by observing photon anti-bunching [40] of the emitted fluorescence light. A confocally preselected diamond nanocrystal is identified in an AFM-topology map of the substrates surface. Then, the AFM tip is being flattened by pressing it onto the substrate. This enlarges the surface of the tip and, thus, increases the pick-up probability. Now the selected nanodiamond is picked up by pushing the AFM-tip several times onto the diamond. A successful pick-up process is indicated by a drop in the fluorescence signal to background-level at the diamond's position (shown in figure 4.5). By placing the tapered optical fiber (TOF) on a clean substrate, the nanocrystal can be placed onto the nanofiber waist by pushing the AFM-tip onto the fiber. Finally, the TOF is detached from the fused silica substrate and the assembled system can be

[1] In the auto-correlation measurement, differences τ of the detection times of photon pair events are recorded by a time-to-digital converter used as a correlation instrument with 77 ps time resolution and stored in a histogram with a time bin width of $t_{\text{bin}} = 0.924\,\text{ns}$. To obtain $g^{(2)}(\tau)$ from this delay time histogram, the number of entries in each time bin is normalized by its average value for long detection time differences $\tau = 0.7 \ldots 1.1\,\mu\text{s}$.

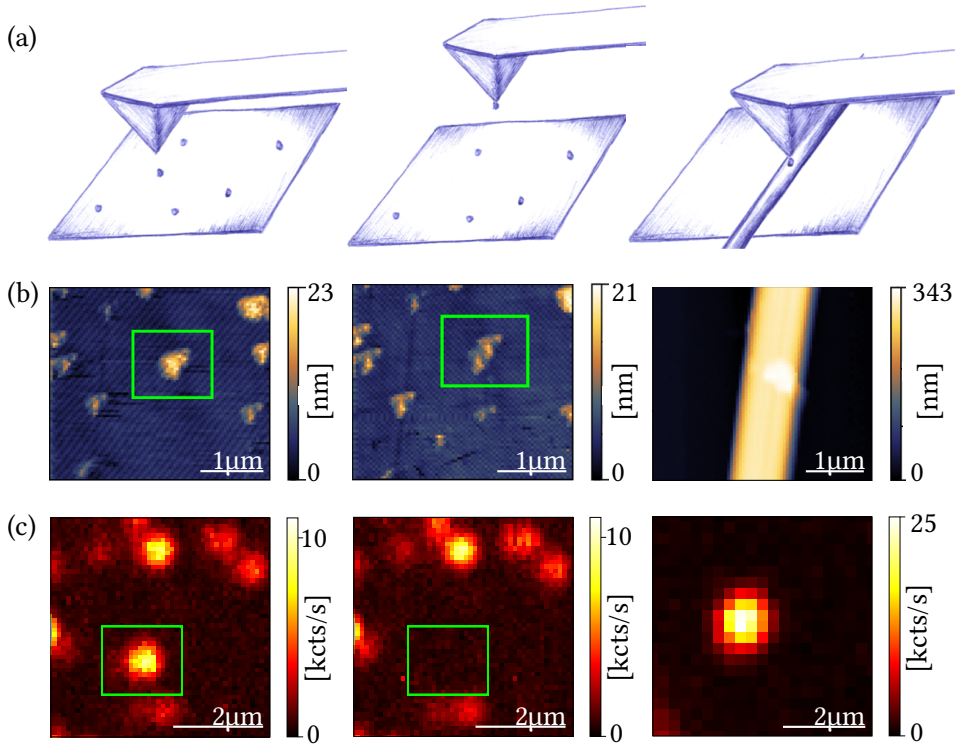

Figure 4.4.: (a) Schematics of the deterministic positioning of single fluorescing diamond nanocrystals onto the apex of an optical nanofiber. (b) Topography and (c) optical scan before pick-up, after pick-up, and after placing the nanocrystal onto the optical fiber (from left to right).

examined.

4.4. Experimental Determination and Investigation of the Coupling

For all optical investigations, the NV-center on the nanofiber is excited through the confocal microscope with a continuous wave laser at a wavelength of 532 nm (perpendicular to the TOF). NV-fluorescence is collected in both ways, confocally with the microscope objective and via the tapered optical fiber.

The coupling of the single NV-center to the guided mode of the TOF can be verified by means of the photon statistics of the fluorescence light. The fluorescence signal is analyzed via its second-order correlation function $g^{(2)}(\tau)$, measured in a Hanbury-Brown-Twiss (HBT) configuration. ThisHBT-interferometer can be realized in two different ways (see figure 4.6): (i) In the standard-setting as used for the identification of single NV-centers in the precharacterization procedure, two single-photon detectors (APD) on either exit port of a bulk beamsplitter

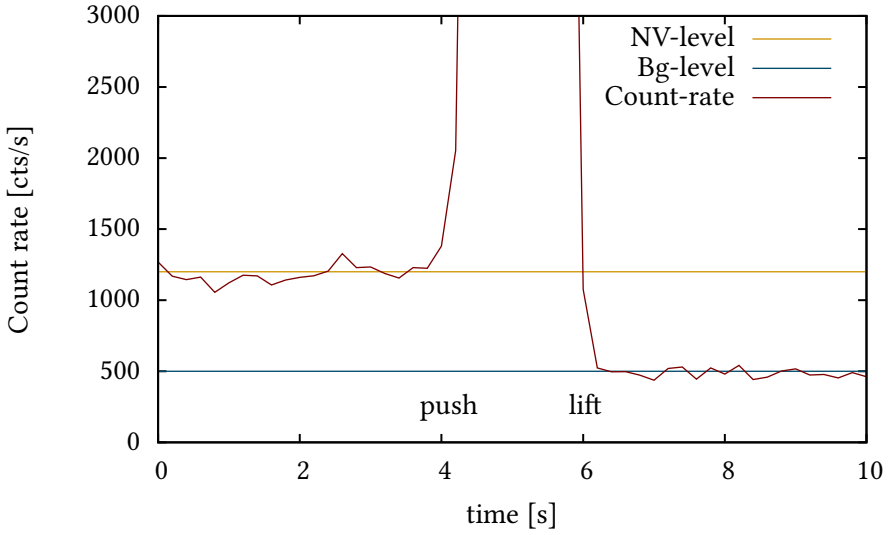

Figure 4.5.: Fluorescence time-trace during the pick-up of a fluorescing diamond nanocrystal. Initially, the fluorescence signal is at the level of the diamond nanocrystal. At 4 s, the AFM-tip is approaching the diamond nanocrystal which results in an additional fluorescence signal from the gold-coated tip. After removing the tip (6 s), a successful pick-up of the diamond nanocrystal is immediately indicated by a drop in the fluorescence signal to the background signal level.

at the output of the confocal microscope [40] can obtain the photon auto-correlation of the free space emission. (ii) The two APDs can be positioned at the outputs of the TOF. In this scheme, the fiber acts as an intrinsic beamsplitter, given that guided photons have equal probability to be detected in one of both directions. Once photon anti-bunching of the guided light is observed, it verifies the coupling of single photons to the guided mode of the TOF.

To further analyze the evanescent coupling of fluorescence light emitted by a single NV-center to the guided mode of the TOF and to obtain more information about uncorrelated background, $g^{(2)}(\tau)$ is obtained for different excitation powers P, ranging from $0.5\,\mathrm{mW}$ to $10\,\mathrm{mW}$ (see Fig. 4.7, b). For comparison, the second-order correlation function is recorded simultaneously at the fiber outputs as well as via confocal collection (see Fig. 4.7, a). Both sets of measured $g^{(2)}(\tau)$ functions are then fitted using a modified three-level model [40, 50]

$$g^{(2)}(\tau) = 1 + p_\mathrm{f}^2[ce^{-\frac{|\tau|}{\tau_1}} - (1+c)e^{-\frac{|\tau|}{\tau_2}}], \tag{4.1}$$

which neglects intensity dependent deshelving of the meta-stable state. The parameter p_f represents the probability, that a detected photon event stems from a single NV-center. τ_1 describes the pump-power dependent slope of the anti-bunching dip, τ_2 governs the decay of $g^{(2)}(\tau) > 1$ for intermediate detection time differences, while c determines its amplitude. To directly quantify the influence of background on the quality of the non-classical single-photon source, the fitted value of the second-order correlation function is plotted for zero detection time difference, i. e. $g^{(2)}(0) = 1 - p_\mathrm{f}^2$ (see Fig. 4.8, a). For low excitation powers, $g^{(2)}(0)$ is determined by

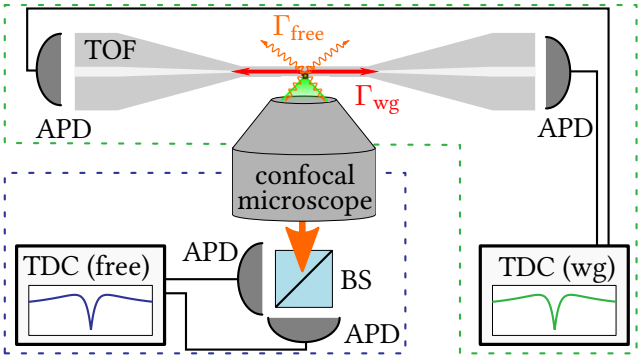

Figure 4.6.: Illustration of the two different implementations of a Hanbury-Brown-Twiss interferometer which are used to verify the coupling. (i) In the standard scheme the two APDs are positioned at the two outputs of a non-polarizing beamsplitter (BS). (ii) As the photons emitted into the fiber are equally probable to travel to one or to the other fiber output, this emitter-fiber-system acts as an intrinsic beamsplitter. Therefore, one APD can be placed on one end of the fiber, while the other APD can be placed on the other fiber output. In both cases, a time-to-digital converter (TDC) is used to associate a detection time with each APD-click. From those detection times, a histogram of the detection time differences of the photons can be generated. This histogram corresponds to the second-order correlation function $g^{(2)}(\tau)$ when normalized for long detection time differences.

the dark count rates of the APDs and residual background fluorescence. Increasing the excitation power P, the influence of the dark count rate and the residual background fluorescence decreases in confocal collection, leading to almost perfect anti-bunching. In fiber-based collection, an excitation power dependent increase of $g^{(2)}(0)$ from 0.26 to 0.67 is observed. This points to additional uncorrelated photons that are mainly attributed to intrinsic fluorescence of the fiber core, generated by Rayleigh-scattered excitation laser light that is coupled into the nanofiber.

As a next step, the nanofiber coupling efficiency $\beta = \Gamma_{\text{wg}}/(\Gamma_{\text{wg}} + \Gamma_{\text{free}})$ can be evaluated, which is defined as the ratio of the radiative decay-rate into the nanofiber Γ_{wg} to the total radiative decay rate $\Gamma_{\text{rad}} = \Gamma_{\text{wg}} + \Gamma_{\text{free}}$. The measurements performed on this assembled structure can be used in combination with numerical FDTD-simulations to predict and measure the coupling efficiency β. The theoretical value for β for such a system has been derived for three main dipole axis relative to the fiber (section 2.3). However, the nanocrystal placed on the fiber is oriented arbitrarily and so are the two emitting dipoles of the NV-center. Therefore, the orientation of the dipoles has to be determined experimentally before expected coupling can be stated.

For an NV-center (see chapter 3) hosted in a diamond nanocrystal, the orientation of the two orthogonal dipoles $\mathbf{p}_1$ and $\mathbf{p}_2$ can be determined via polarization dependent excitation measurements and polarization analysis of the emitted fluorescence light [83]. In this experiments the linear polarization angle ψ of the excitation laser ($\lambda = 532\,\text{nm}$) is varied and the broad-

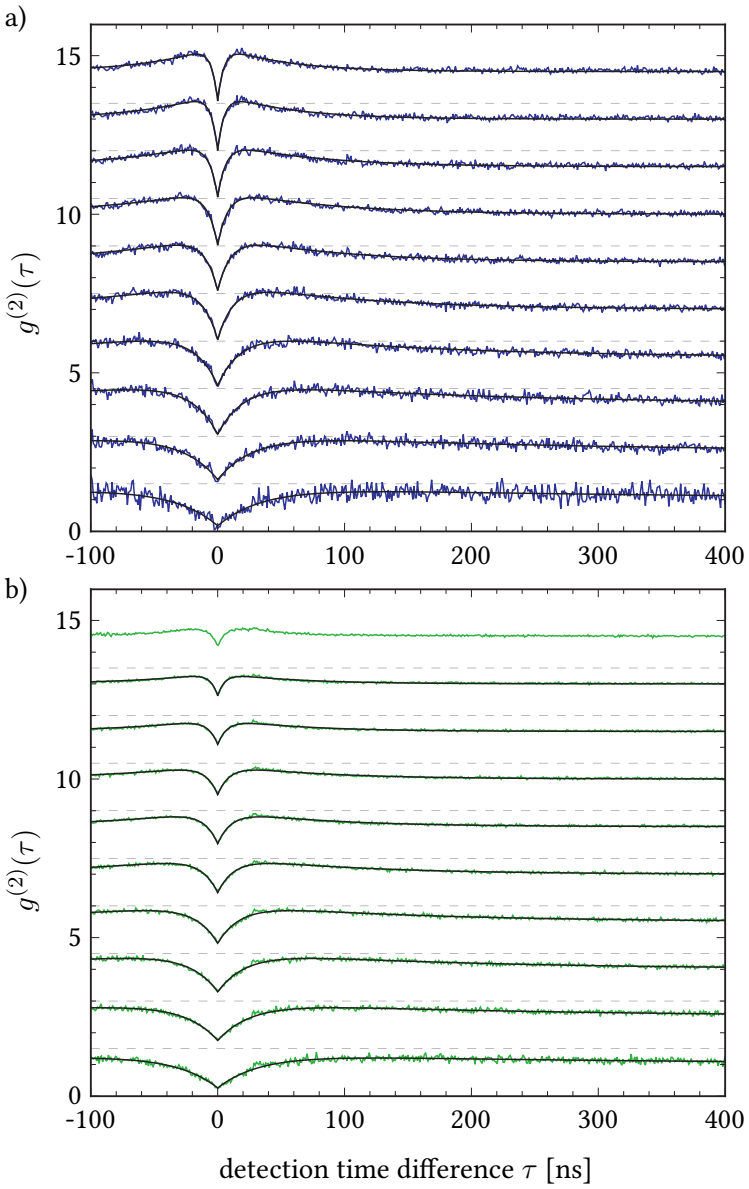

Figure 4.7.: Second-order correlation function $g^{(2)}(\tau)$ of fluorescence light emitted by a single NV-center for different excitation powers $P = (0.5, 1.0, 1.5, 2, 3, 4, 5, 6, 8, 10)$ mW (from bottom to top), coupled to an optical nanofiber with a diameter of 260 nm. The NV-center is excited perpendicular to the optical fiber via a confocal microscope. Fluorescence photons are collected (a) via the objective of the confocal microscope and (b) via coupling to the guided mode of the optical nanofiber. The anti-bunching dip at zero detection time difference $\tau = 0$ demonstrates the non-classical character of the fluorescence light as well as the coupling of the NV-center emission to the optical nanofiber. For better discrimination, the curves are shifted vertically by increments of 1.5.

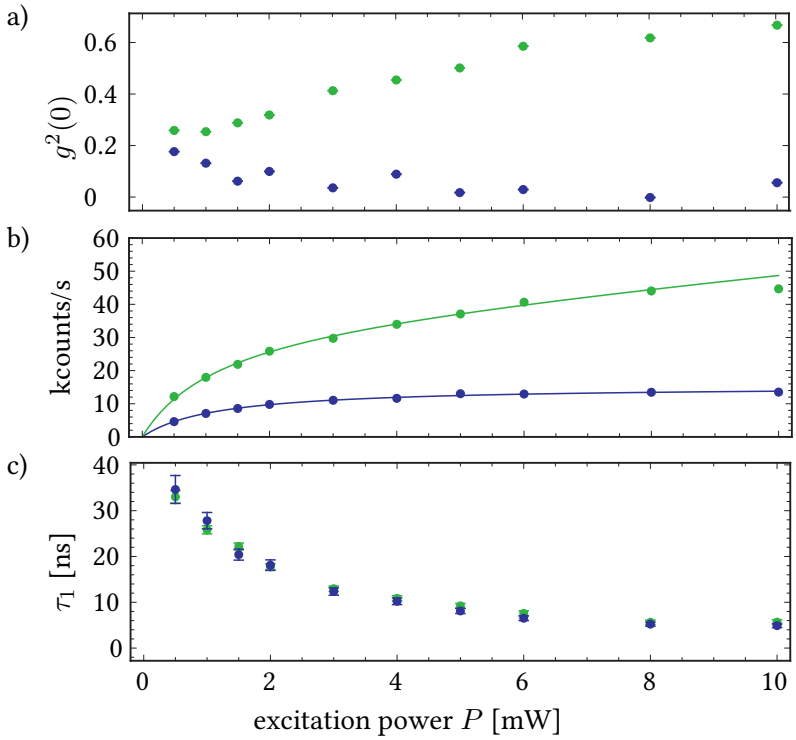

Figure 4.8.: (a) Second-order correlation function $g^{(2)}(0)$ at detection time difference $\tau = 0$, (b) detected count rate, and (c) fit-parameter τ_1 as a function of the excitation power P. Blue data points stem from confocal collection whereas green data points from nanofiber collection, respectively.

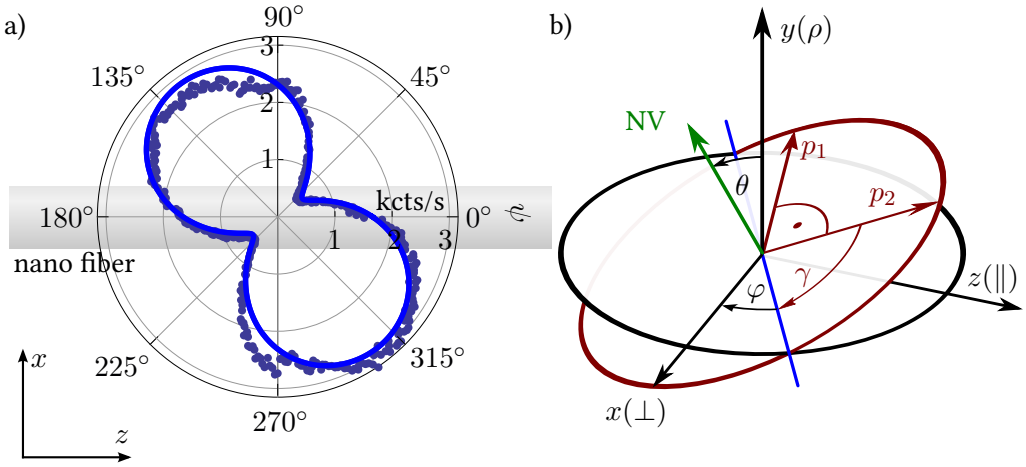

Figure 4.9.: (a) Measured confocal count-rate of an NV-center on a nanofiber as function of the excitation polarization angle ψ and corresponding fit (excitation power 0.5 mW). (b) Euler angles $(\theta, \varphi, \gamma)$ used to describe the spatial orientation of the two orthogonal dipoles $\mathbf{p}_1$ and $\mathbf{p}_2$ of the NV-center on the surface of an optical nanofiber. The projections of $\mathbf{p}_i$ onto the eigenaxes of the nanofiber $(\perp, \parallel, \rho)$ $((\phi, z, r)$ from 2.3 respectively) allows to determine the nanofiber coupling efficiency.

band NV-fluorescence is detected polarization insensitive. Therefore, the orientation of the NV symmetry axis can be determined, which is given by the Euler angles φ and θ (see Fig.4.9, b). However, the orientation of these dipoles (given by the Euler angle γ) within the plane perpendicular to the NV symmetry axis [83] can not be accessed. However, the knowledge about the orientation of the NV symmetry axis with respect to the nanofiber is sufficient to perform numerical FDTD simulations providing a lower and upper bound for the predicted and measured nanofiber coupling efficiency β.

As a first step towards the determination of the dipole orientation, the count-rate of confocally detected photons is measured (emitted by the single NV-center on the nanofiber) as a function of the excitation polarization angle ψ (see Fig.4.9, a). These measured data are then fitted with the model of a saturating fluorescence intensity I (adopted from (3.1)):

$$I(\psi) = \varkappa' \frac{P(\psi)}{P(\psi) + P_{\text{sat}}}. \tag{4.2}$$

This model includes the projection of the excitation polarization $P(\psi)$ onto the dipoles of the NV-center. The two free parameters are the saturation power P_{sat} and a normalization factor $\varkappa'$. The saturation power $P_{\text{sat}} = 1.17\,\text{mW}$ is determined by a least square fit of the power-dependent confocal count rate (blue data points in Fig. 4.8, b) with the model $\varkappa P/(P + P_{\text{sat}})$. The model (4.2) accounts for the saturation of the two coupled dipole transitions at room tem-

perature [84, 85] and the polarization dependence

$$P(\psi) = P_0[\sin^2(\psi - \varphi) + \cos^2(\psi - \varphi)\cos^2\theta] \tag{4.3}$$

of the excitation power for the two dipoles $\mathbf{p}_1$ and $\mathbf{p}_2$ in the weak excitation regime [83]. In this model, θ is the angle between the NV symmetry axis and the optical axis of the confocal microscope (y-axis) whereas φ is the Euler angle corresponding to a rotation around the y-axis (see figure 4.9 b)).

The mentioned fit finally yields the Euler angles

$$\varphi = (36.3 \pm 3.0)^\circ \qquad \theta = (70.7 \pm 0.3)^\circ, \tag{4.4}$$

which describes the orientation of the NV symmetry axis.

Now, a lower and an upper bound for the expected nanofiber coupling efficiency β can be derived. A single, arbitrarily oriented dipole $\mathbf{p}_i(\varphi, \theta, \gamma)$ of the NV-center can be decomposed with the help of an Euler transformation [86] into the components $p_\perp, p_\parallel$ and p_ρ for the nanofiber eigenbasis $\{\perp, \parallel, \rho\}$. Within this part of the work, this notation is intuitive. However, there is a direct correspondence to the cylindrical coordinates used in section 2.3: $\perp = \phi$, $\parallel = z$ and $\rho = r$. As known from the calculations in section 2.3, the coupling efficiency of a dipole oriented along the respective eigenaxis from FDTD simulations ($0.275, 0.156$ and 0.415 for a dipole positioned 10 nm above the surface of the nanofiber with a radius of 260 nm and for an emission wavelength of 666 nm) the nanofiber coupling efficiencies β_1 and β_2 can be calculated for the two dipoles $\mathbf{p}_1$ and $\mathbf{p}_2$:

$$\beta_i = \sqrt{(0.275 p_{i,\perp})^2 + (0.156 p_{i,\parallel})^2 + (0.415 p_{i,\rho})^2} \tag{4.5}$$

For an NV-center the nanofiber coupling efficiency β is then given by

$$\beta = \frac{\beta_1 + \beta_2}{2}. \tag{4.6}$$

By variation of γ (plotted in figure 4.10), which takes into account the unknown orientation of the two dipoles in the plane perpendicular to NV symmetry axis, and for fixed angles $\varphi = 36.3^\circ$ and $\theta = 70.7^\circ$ an upper and lower bound for the expected coupling efficiency is derived to

$$(31.84 \pm 0.03)\% \leq \beta \leq (32.82 \pm 0.03)\%. \tag{4.7}$$

This value has to be compared with the actual measured coupling efficiency β_{meas}, which can be determined as follows: First Γ_{free} is obtained from the fit of the power dependent confocal count rate (blue data points in Fig. 4.8, b) with the model $\varkappa P/(P + P_{\text{sat}})$. Here, $\varkappa$ is the count rate for excitation power $P \to \infty$. This least square fit converges to a saturation power of $P_{\text{sat}} = 1.17\,\text{mW}$ and a free-space saturation count rate of $C_{\text{free}} = 7.70 \times 10^3\,\text{s}^{-1}$. The corresponding decay rate Γ_{free} into free-space modes can be determined from C_{free} by taking into account the fraction of photons collected by the microscope objective (effective numerical aperture $\text{NA}^* = 0.32 \pm 0.01$), transmission losses from the focal spot to the single photon detectors (APD), and the quantum efficiency $\eta = 0.65$ of the SPDs. With the help of numerical

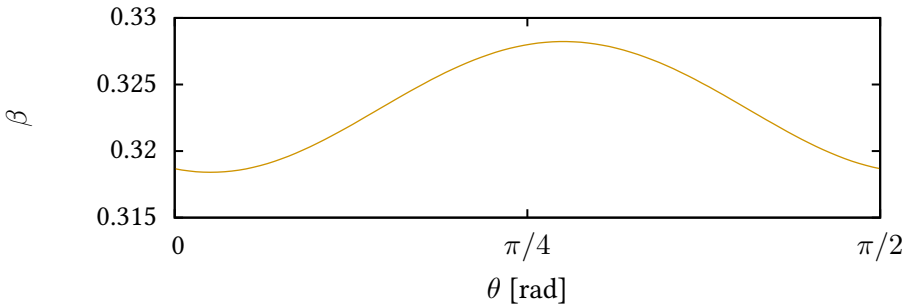

Figure 4.10.: Plot of the theoretical coupling factor β as a function of the undetermined angle θ.

FDTD simulations, a lower and upper bound can be obtained for Γ_{free} of $(1.7 \pm 0.1) \times 10^6\ \text{s}^{-1}$ and $(1.8 \pm 0.1) \times 10^6\ \text{s}^{-1}$, respectively.

Next, the amount of single photons scattered into the nanofiber per second, i. e. the radiative decay rate Γ_{wg} is calculated. To determine the saturation count rate for the nanofiber collection, the corresponding power dependent count rate (green data points in Fig. 4.8, b) is fitted with with the model

$$I(P) = \varkappa' P/(P + P_{\text{sat}}) + mP, \tag{4.8}$$

taking into account an additional linear increase mP of the fiber background fluorescence. For this fit, P_{sat} is fixed to the value of the first fit (confocal detection and no fiber background fluorescence), resulting in a nanofiber saturation count rate of $C_{\text{wg}}^{\text{sat}} = 19.6 \times 10^3\ \text{s}^{-1}$. A simple analysis shows that $\Gamma_{\text{wg}}^{\text{sat}} = C_{\text{wg}}/(\eta\sqrt{T_{\text{ges}}})$, where $T_{\text{ges}} = (2.41 \pm 0.03)\%$ is the overall transmission of the TOF-system (includes the intrinsic transmission losses of the TOF, transmission losses due to spectral filters, and coupling losses stemming from the nanofiber into detector fibers) and $\eta = 0.65$ is the quantum efficiency of the used APDs. These values lead to $\Gamma_{\text{wg}} = (1.94 \pm 0.02) \times 10^5\ \text{s}^{-1}$.

Apart from the determination of the expected nanofiber coupling efficiency, the performed FDTD simulations also enable the estimation of the decay rate Γ_{free} into free-space modes, an important part for the determination of the measured fiber coupling efficiency. On the basis of those FDTD-simulations, also the fraction of light scattered by a dipole (aligned parallel to one of the eigenaxes $(\perp, \parallel, \rho)$ of the nanofiber) into the effective numerical aperture ($\text{NA}^* = 0.32 \pm 0.01$) of the microscope objective $(0.0515, 0.0705, 0.00429)$ [2] is determined. For an arbitrarily oriented dipole $\mathbf{p}_i$ the fraction of photons collected by the microscope objective is then given by

$$\eta_i^{\text{coll}} = \sqrt{(0.0515 p_{i,\perp})^2 + (0.0705 p_{i,\parallel})^2 + (0.00429 p_{i,\rho})^2}, \tag{4.9}$$

[2] A dipole oriented radially ρ with respect to the fiber and on the opposite side from the confocal collection optics is also parallel to the optical axis of the confocal microscope. Even though radiation can be collected via the microscope objective, the resulting mode cannot be coupled into a single-mode fiber. This would justify to set the collection efficiency for this dipole orientation to zero. Nevertheless, in the following calculation the value obtained from the simulation will be used.

and for an NV-center

$$\eta^{\text{coll}} = \frac{\eta_1^{\text{coll}} + \eta_2^{\text{coll}}}{2}. \tag{4.10}$$

Again, varying the angle γ (plotted in figure 4.10) (for fixed angles $\varphi = 36.3°$ and $\theta = 70.7°$), an upper and lower bound for η^{coll} can be derived:

$$0.040 \pm 0.002 \leq \eta^{\text{coll}} \leq 0.044 \pm 0.002 \tag{4.11}$$

With these values and by taking into account all losses of the confocal microscope, the emission rate of the NV-center into free-space modes is $(1.7 \pm 0.1 \leq \Gamma_{\text{free}}^{\text{sat}} \leq 1.8 \pm 0.1)$ Mcts/s. Combined with the total radiative decay rate into the fiber mode $\Gamma_{\text{wg}}^{\text{sat}} = (194 \pm 2)$ kcts/s, the measured nanofiber coupling efficiency is limited to

$$(9.5 \pm 0.6)\% \leq \beta_{\text{meas}} \leq (10.4 \pm 0.7)\% \tag{4.12}$$

This value of the measured coupling should be compared to the simulated coupling efficiency of a radiating NV-center (emission wavelength $\lambda = 666$ nm, located 10 nm above the nanofiber) coupled to a nanofiber with 260 nm diameter. From polarization dependent excitation measurements and numerical FDTD-simulations, a lower and upper bound for β has been estimated as $(28.78 \pm 0.03)\%$ and $(29.22 \pm 0.03)\%$, respectively. Reduction of this value by few percent can be expected due to the broadband emission spectrum of the NV-center, however, can not explain the discrepancy to the experimental findings. This contradiction is also observed by a recent experimental work with a single CdSe/ZnS nanocrystal [71].

As the total decay rate $1/\tau_{\text{tot}} = \Gamma_{\text{rad}}^{\text{sat}} + \Gamma_{\text{nrad}}^{\text{sat}}$, i. e. the sum of the radiative and non-radiative rate, can be determined from the extrapolation of $\tau_1(P)$ obtained from the measured second-order correlation functions for different excitation powers $\tau_{\text{tot}} = \lim_{P \to 0} \tau_1(P)$ [40], an estimate for the internal quantum efficiency QE$= \Gamma_{\text{rad}}^{\text{sat}} \tau_{\text{tot}}$ of the NV-center can be provided too. For small excitation powers the fit parameter τ_1 reaches $\tau_{\text{tot}} = (63 \pm 9)$ ns (see Fig. 4.8, c), resulting in an upper and a lower bound for the quantum efficiency QE of $(12.9 \pm 2.0)\%$ and $(11.8 \pm 1.8)\%$. This finding is in good agreement with recent QE-measurements from NV-centers in diamond nanocrystals of different size [87].

In section 3, an excited state life time of the NV-center hosted by a diamond nanocrystal on a fused silica substrate has been discussed. With pulsed excitation measurements on diamond nanocrystals of the same type, a lifetime of (25 ± 9) ns has been obtained, which is in agreement with the literature [68]. The theoretical calculations in section 4 suggest a reduction of the lifetime when the crystal is placed on the TOF. However, the measured lifetime of $\tau_{\text{tot}} = (63 \pm 9)$ ns is significantly longer than expected. Prior to the pick-up the lifetime of this NV-center has not been determined, therefore a direct comparison is not possible. However, a $g^{(2)}$-fit to the autocorrelation function recorded before the pick-up can be compared to the autocorrelation function recorded after the assembly at equal excitation power relative to the saturation power. The comparison of the τ_1-values on the substrate and on the fiber reveals a longer τ_1 of the fiber-coupled system, but also a significant difference of the c-parameter, the amplitude of the decay of $g^{(2)} > 1$ (see equation 4.1). This parameter is an indication of the

strength of the non-radiative coupling of the shelving state ^1A to the excited state ^3E [40]. Due to the difference in the c-parameter, the comparison of the two life-times is hardly interpretable. This change in non-radiative coupling is not directly introduced by the change in the photonic states. However, during the nanomanipulation, the orientation of the nanocrystal with respect to the glass surface has changed, and, as can be seen in figure 4.4 b), graphitic shells are partially striped off during the pick-up of the crystal. Both changes of the mechanical local environment of the NV-center which can be the reason for the different c-values.

Concluding, the measured exited state lifetime of $\tau_{\text{tot}} = (63 \pm 9)\,\text{ns}$ is not explained by the theory. The comparison of the autocorrelation functions before and after assembly could not lead to conclusions whether this value is caused by the presence of the fiber or is a feature of this specific diamond nanocrystal.

4.5. Spectral Modification

The quantification of the total coupling β was presented in the previous section. However, in accordance with the theoretical analysis 2.3.2 the coupling of the NV-center to the guided mode is expected to be broadband with a certain wavelength-dependency. As the NV-center features a broadband emission spectrum, spectra of the emission into free space and into the tapered optical fiber can be compared in order to test the predicted wavelength-dependency.

The expected wavelength-dependency is described by the coupling factor β as a function of the wavelength, which can be described as the sum of both dipoles (see equations 4.5 and 4.6):

$$\beta(\lambda) = \frac{1}{2}\sum_{i=1}^{2}\sqrt{(\beta_\phi(\lambda)p_{i,\perp})^2 + (\beta_z(\lambda)p_{i,\parallel})^2 + (\beta_r(\lambda)p_{i,\rho})^2} \tag{4.13}$$

As found in section 2.3.2 (see figure 2.10), β_r and β_z are decreasing monotonically from around $\lambda = a/0.22 = 591\,\text{nm}$ towards longer wavelengths, whereas β_ϕ is nearly constant. Therefore, $\beta(\lambda)$ can be expected to decrease towards longer wavelengths for both dipole orientations. The simulated coupling efficiency can be derived numerically for discrete wavelengths from numerical FDTD-simulations. Further analysis of $\beta(\lambda)$ for the two dipoles as derived in the previous section shows a nearly linear decrease from $575\,\text{nm}$ to $800\,\text{nm}$, which covers the complete NV^- emission spectrum.

In order to test the predicted wavelength-dependency, the spectrum of the NV-center emission into free space has to be compared to the emission into the guided mode. The free space emission I_{free} is collected via the confocal microscope and guided to the fiber-coupled spectrometer[3]. The background signal is collected from an adjacent dark spot on the TOF. To record the spectrum $I_{\text{wg,raw}}$ of the photons emitted into the TOF, it is connected to the spectrometer via a free space spectral filtering stage with equal set of filters[4] as used in the confocal microscope.

[3] The total resolution of the spectrometer is about $0.7\,\text{nm}$ [88]. A more detailed discussion of its properties can be found here [89].

[4] A long-pass filter at $590\,\text{nm}$ in combination with a notch-filter at $532\,\text{nm}$ are used to remove the excitation laser light.

The background signal is captured at the output of the TOF, while the excitation is focused at an adjacent dark spot on the TOF. In the previous section uncorrelated background fluorescence $I_{\text{wg,bg}}$ has been found, which is attributed to fiber fluorescence generated by excitation light coupled into the fiber via the diamond nanocrystal. To analyze this background fluorescence, a pure scattering center (dielectric particle without a color center) on the TOF can be used, as such a center does not generate intrinsic fluorescence but only scatters excitation laser light into the fiber. This produces the same fiber fluorescence spectrum as the excitation light scattered by the diamond nanocrystal. Such a pure scattering center can be a non-fluorescent diamond nanocrystal or other dielectric dust-particle and is indicated by a strong fluorescence signal $I_{\text{wg,bg}}$ at the output of the TOF, but no signal during confocal detection. While focusing the excitation laser onto this scattering center, the spectrum $I_{\text{wg,bg}}(\lambda)$ of the fluorescence signal guided by the TOF provides the spectrum of the fiber-fluorescence. Due to the different scattering cross-sections of the fluorescing diamond nanocrystal and the pure scattering center, this fiber-fluorescence signal cannot be simply subtracted from the raw NV-fluorescence spectrum $I_{\text{wg,raw}}$ in the TOF. However, there is a spectral region ($600 - 620\,\text{nm}$), where the fiber-fluorescence signal is strong, while the free space emission spectrum I_{free} of the NV-center shows no signal. This spectral window can be used to scale the level of the fiber-fluorescence spectrum to fit the spectrum $I_{\text{wg,raw}}$ (compare figure 4.11). This rescaled fiber-fluorescence spectrum can now be subtracted from the raw data to obtain the pure spectrum I_{wg} of the NV-centers emission into the fiber. The integrated intensity of the of the fiber-fluorescence amounts to 33% of the raw integrated intensity. This value can be cross-checked with the saturation of excitation power series of the signal at the output of the TOF, which has already been evaluated in the previous section. There, the contribution of fiber-fluorescence to the total signal at the excitation power $P = 10\,\text{mW}$ is $((\varkappa'/m)(1 + P_{\text{sat}}/P)^{-1} + 1)^{-1} = 35\%$. This compares very well to the value which was calculated based on the measured spectra (33%). All three spectra are plotted in figure 4.11 together with the confocally collected free space emission of the NV-center for comparison.

Figure 4.12 shows the spectrum of the radiative emission captured via the confocal microscope I_{free} and the spectrum of the emission of the NV-center into the nanofiber. The different collection efficiency of the emission into the nanofiber and into free-space modes makes it necessary to normalize the two spectra with respect to each other. The comparison of both spectra clearly indicates decreasing coupling for longer wavelengths, which is in accordance to the theoretical predictions. This feature is especially dominant around the zero phonon line ($637\,\text{nm}$).

In order to quantitatively compare theory and experiment, the coupling as function of the wavelength has to be extracted from these two spectra. The overall measured coupling factor $\beta^{\text{tot}}_{\text{meas}} = \Gamma_{\text{wg}}/(\Gamma_{\text{free}} + \Gamma_{\text{wg}})$ has been determined from measurements in section 4.4 to $\beta^{\text{tot}}_{\text{meas}} = (10 \pm 0.5\%)$. Neglecting variations in the detection efficiency[5] of the APDs for different wavelengths, one can assume that the detected rate is proportional to the integral over the recorded spectrum $\Gamma^{\text{tot}} = C \int I(\lambda)\text{d}\lambda$. The proportionality factor C is equal for the guided

[5]Both spectra I_{free} and I_{wg} have a very similar distribution, but the center of mass is shifted by about 20 nm around 700 nm. The quantum efficiency of the APDs (Perkin Elmer SPCM-AQ4C) shows a plateau at this wavelength and variations of less than 2% have to be expected according to the specifications.

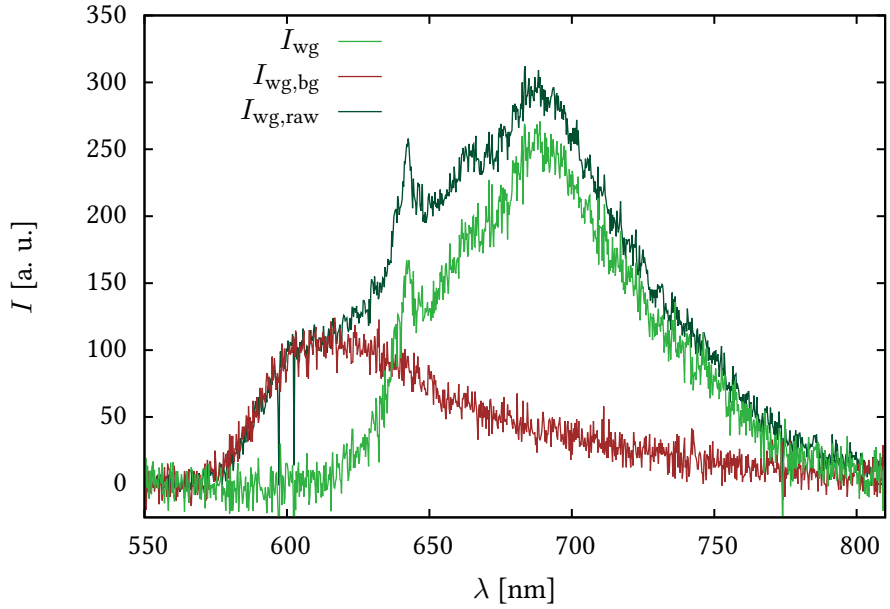

Figure 4.11.: Spectra of the fiber-coupled emission illustrating the correction of $I_{wg,raw}$ for fiber-fluorescence background. $I_{wg,raw}$ is the spectrum of the total fluorescence signal at the output of the TOF. $I_{wg,bg}$ is the spectrum recorded while exciting the second, not intrinsically fluorescing scattering center on the TOF. This spectrum shows the fluorescence background produced by excitation light coupled into the fiber. This background is scaled by 1.38 to match $I_{wg,raw}$ around $\lambda = 600\,\text{nm}$. $I_{wg} = I_{wg,raw} - I_{wg,bg}$ is then the fluorescence of the NV-center coupled into the fiber. According to the free space emission spectrum I_{free} (see figure 4.12)of the coupled system, there is no NV-fluorescence signal around $\lambda = 600\,\text{nm}$ which justifies this approach. All spectra are recorded at 10 mW excitation power and corrected for the spectrometer's intrinsic background.

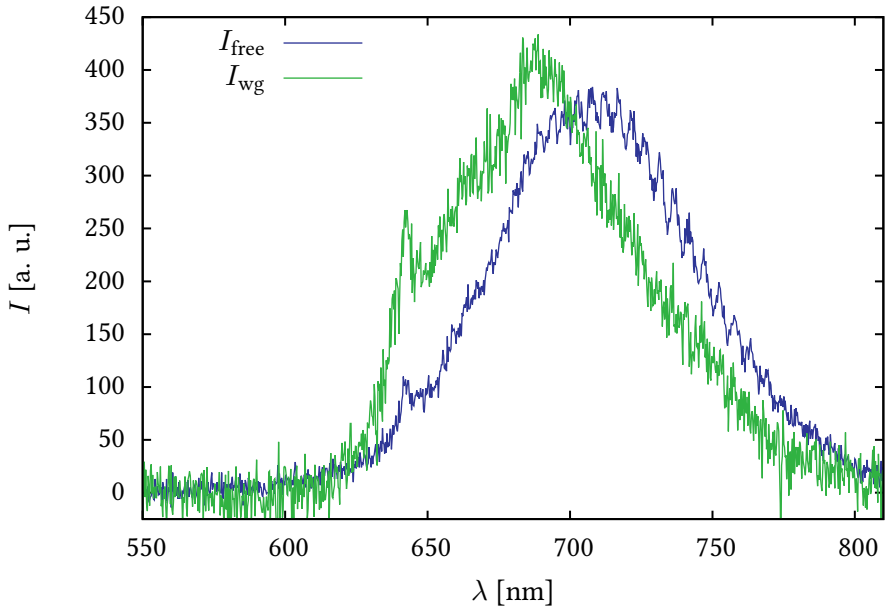

Figure 4.12.: Spectra of the NV-center captured at equal excitation conditions (10 mW excitation power). One spectrum I_{free} is collected via the confocal microscope, showing the emission into free space. The other spectrum I_{wg} shows the NV-center's emission coupled into the TOF. I_{wg} is corrected for fiber-fluorescence as shown in figure 4.11. The intensity is plotted in arbitrary units, however, both spectra are normalized relatively to the same total intensity.

and the free-space emission as it just relates the APDs count rate to the signal output value of the spectrometer. C can also be interpreted as the relative normalization condition of the two spectra with respect to the total measured coupling $\beta^{\text{tot}}_{\text{meas}}$:

$$C = \beta^{\text{tot}}_{\text{meas}} \frac{\int I_{\text{free}}(\lambda)\mathrm{d}\lambda + \int I_{\text{wg}}(\lambda)\mathrm{d}\lambda}{\int I_{\text{wg}}(\lambda)\mathrm{d}\lambda} \tag{4.14}$$

With this proportionality factor C the coupling factor can be calculated from the spectrometer signal $I(\lambda) = \Gamma(\lambda)/C$ for each wavelength separately:

$$\beta_{\text{meas}}(\lambda) = C \frac{I_{\text{wg}}(\lambda)}{I_{\text{wg}}(\lambda) + I_{\text{free}}(\lambda)} \tag{4.15}$$

This coupling efficiency, extracted from the measured spectra (shown in figure 4.13) can be compared to the wavelength-dependence of the simulated coupling efficiency β, presented in section 2.3.2. In order to support this comparison with actual numbers, a linear function can be fitted to the data in a wavelength interval (627 nm -781 nm), where both spectra show significantly strong signal. Even though, a linear function is a poor parameterization of the wavelength-dependency of the measured coupling efficiency, the basic tendency will be reflected. The regression of the linear function converges to a slope of -1.12 μm^{-1} of the measured coupling $\beta_{\text{meas}}(\lambda)$. For the same wavelength range, also the predicted $\beta(\lambda)$ can be approximated as linear function yielding a slope of -0.43 μm^{-1}. In comparison, the sign and the order of magnitude of the slope are the same in both cases, but the absolute value of the slope of the measured values is more than twice the expected value. This means that a much stronger wavelength dependence of the coupling efficiency has been measured than the FDTD-simulations suggest.

This discrepancy between simulations and measurement might arise from wavelength dependencies in the collection of the free space emission by the confocal microscope. However, according to the manufacturers specifications, such a strong effect cannot be attributed to any of its components. The precise distance of the NV-center to the nanofiber is not known, however, with certainty it is located within the diamond nanocrystal of about 20 nm in hight. Within this crystal, the NV-center is most likely located close to the center, therefore, the assumption of 10 nm distance to the nanofiber surface is reasonable. Nevertheless, the distance of the NV-center to the fiber within the 20 nm crystal changes the emission enhancement factor α about less than 5% and the variation in the coupling efficiency β is on the same order of magnitude. Based on FDTD-simulations, the influence of a dielectric sphere representing the diamond nanocrystal on the coupling factor could me analyzed. Its influence has been found to be below 10%. Neither the uncertainty in the distance, nor the presence of the diamond nanocrystal can explain the deviation of theory and experiment. Another explanation worth consideration is that the spectral transmission of the nanofiber is modified by Rayleigh scattering at dust particles. Though, a stronger reduction of the transmission would be expected for shorter wavelengths which would result in the opposite effect as found here. In the same way, an over-estimation of the fiber-fluorescence would have lead to an even stronger discrepancy between theory and experiments and an under-estimated fiber-fluorescence would have lead to negative values in the fiber-coupled NV-spectrum, which can be dismissed as unphysical. In

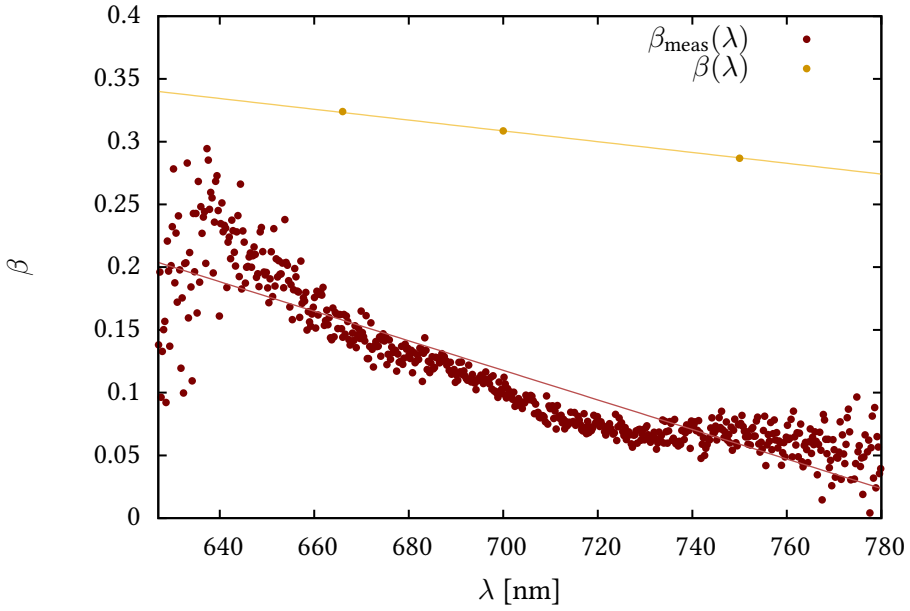

Figure 4.13.: Plot of the wavelength-dependence of the coupling factor β. The plot shows the coupling factors extracted from FDTD-Simulations as well as those derived from the comparison of the emission spectra into the waveguide and emitted into free space. Both dependencies are approximated by a linear function (plotted as lines) in order to allow a comparison of the mean slope. The data extracted from the simulations shows a slope of -0.43 μm^{-1} whereas the measured data features a slope of about -1.12 μm^{-1}.

any case, it seems likely that the discrepancy found has the same origin as the effects which prevents the measured coupling to be closer to the expected strength.

4.6. Summary

The experimental demonstration of the evanescent coupling of a single quantum emitter to a guided waveguide mode is performed with a NV-center which has been coupled to a tapered optical fiber (TOF). The nanofiber waist of a TOF has been optimized for efficient evanescent coupling to single nitrogen vacancy-centers. A highly accurate positioning of a preselected diamond nanocrystals has been used to assemble a system of a tapered optical fiber (TOF) and fluorescing diamond nanocrystal hosting a single NV-center. The nanocrystal was placed on the apex of the nanofiber waist of the TOF. From this system, the single photon emission of the NV-center was identified at the output of the TOF, verifying the evanescent coupling of the NV-center to the guided mode. At saturation power, 88% of the detected fluorescence signal at the TOF output stems from the NV-center. The residual uncorrelated background showed a linear increase with the excitation power. This background is attributed to fiber-fluorescence generated by excitation laser light coupled into the TOF by Rayleigh-scattering at the diamond nanocrystal. This scattering is inevitable for every quantum emitter hosted in dielectric nanoparticles. The generation of such fiber-fluorescence from the excitation laser is common feature of standard optical fibers.

From the power-dependent autocorrelation function, the excited lifetime has been determined to (63 ± 9) ns. This value is about a factor of three larger than usually found for NV-centers hosted in diamond nanocrystals (around (22 ± 4) ns [68]). The unanticipated long lifetime found in the experiment can be caused by the presence of the nanofiber, however, from the theoretical calculations (section 2.3.2) a reduction, rather than an extension of the lifetime is expected.

The total evanescent coupling of the NV-centers emission to the TOF has been quantified to (10 ± 5)%, which is about one third of the expected value at a wavelength of 666 nm. Similar results have been found with a single CdSe/ZnS nanocrystal and a diamond nanobeam, each coupled to a tapered optical fiber [71, 90]. A detailed analysis of the spectral dependence could be done based on the comparison of the free-space and fiber-coupled spectra of the broad NV-emission. Here, theory and experiment share the tendency, but the experiment shows a much stronger wavelength dependency.

5. Design and Fabrication of On-Chip Strip Waveguides

The evanescent coupling of a quantum emitter to a single waveguide mode (see chapter 2.1) has great potential in the field of integrated optics. Such integrated optical devices provide a highly attractive platform for applications in quantum information science as well as in the field of sensing, where photons can be used to mediate interactions between two separated quantum systems or to transfer information about the state of a single quantum system to a detector. In this context, a most basic device is a photon emitter and a detector which are connected by an optical mode of a light guiding structure. Additionally, there is the possibility to add different stages of interaction with other systems to add functionality. This part of this work is driven by the idea of implementing an on-chip platform which uses dielectric waveguides to build a basis for a huge variety of integrated optical devices. The requirements on such a photonic platform can be separated into three problems. First, the quantum system (or quantum emitter) has to be optically coupled to a waveguide. Second, the waveguide is expected to transport the photons with low loss and strong mode confinement (to reduce crosstalk with neighboring waveguides). Third, the system is required to be able to couple the photons to another quantum system, another device or the macroscopic world, for instance an external photo detector. Usually, the three aspects pose different, partly even contradictory requirements on a system.

In this chapter the design, fabrication, and characterization of a single-mode waveguide is presented addressing all three problems by featuring broadband efficient evanescent coupling to fluorescent quantum emitters combined with low-loss guidance and efficient off-chip coupling to single-mode optical fibers.

5.1. The Design of the Rectangular Cross-Section Waveguides

The waveguides in the on-chip design have a rectangular cross section geometry with finite extensions in x and y. Such a rectangular shape has two advantages. First, the cross-section is the natural result of a top-down lithographic fabrication process as it is common for on-chip devices. Second, two independent size parameters a_x and a_y provide more freedom for the design e.g. compared to the cylindrical nanofiber. A rectangular waveguide features hybrids of TE- and TM-modes. In the case of a non-quadratic waveguide, the modes with electrical polarization along y and x are not degenerate, meaning they show individual extensions, profiles, and propagation constants. For a waveguide with high aspect ratio ($a_x/a_y \ll 1$), these two polarizations are often referred to as quasi TE and quasi TM modes, as the geometry and the resulting modes are closely related to those of a one-dimensional slab waveguide (see chapter

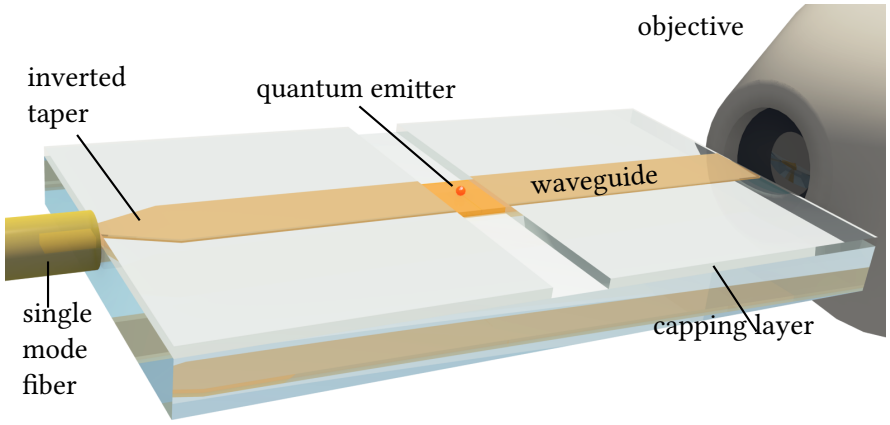

Figure 5.1.: a) Schematic view of a waveguide on a glass substrate with inverted taper and a butt-coupled single-mode fiber on the left. On the right a microscope objective is illustrated, used in combination with the butt-coupled fiber in the characterization of the waveguides. A quantum emitter coupled to the waveguide is indicated by a red sphere in the center.

2.2).

The complete analysis of these hybrid modes in such 2-dimensional confined rectangular waveguides cannot be done analytically. However, there are methods widely used in the literature to approximate mode profiles and propagation constants like the *effective index method* or the *Marcatili's method* [91]. Those methods are able to predict roughly the basic shape of the modes and approximate the effective refractive index n_{eff}. However, they do not provide details on the actual mode structure. In order to evaluate the coupling parameters later on, knowledge of the precise local electric field strength is essential. Therefore a more precise method for the mode calculation is necessary. Here, it comes in handy that todays computers allow for fast numeric mode-solving of complicated structures with high spacial and temporal resolution. As those simulated modes approximate the real modes well, this technique is also very useful to visualize and discuss the modal properties and features. Similar to the determination of the coupling constants for the cylindrical waveguide in section 4, the knowledge of those mode profiles and properties makes it possible to predict the coupling parameters with a dipole emitter.

The rectangularly shaped waveguides presented here are intended to transfer the evanescent coupling principle, shown for the NV-centers with a nanofiber (chapter 4) to an integrated on-chip waveguide (see figure 5.1). This integrated waveguide is designed to provide a versatile platform for on-chip optics. The geometric design is optimized for coupling to NV-center (see chapter 3), but can be easily rescaled to provide efficient evanescent optical coupling to various kinds of solid state quantum emitters like quantum dots or other defect centers in nanocrystals. For the waveguide core, the high refractive index dielectric material Ta_2O_5 ($n_2 = 2.1$) has been chosen, whereas the lower cladding is made of fused silica ($n_1 = 1.46$). Both materials show a low autofluorescence [92], an important property for sensitive experiments on the single emitter level.

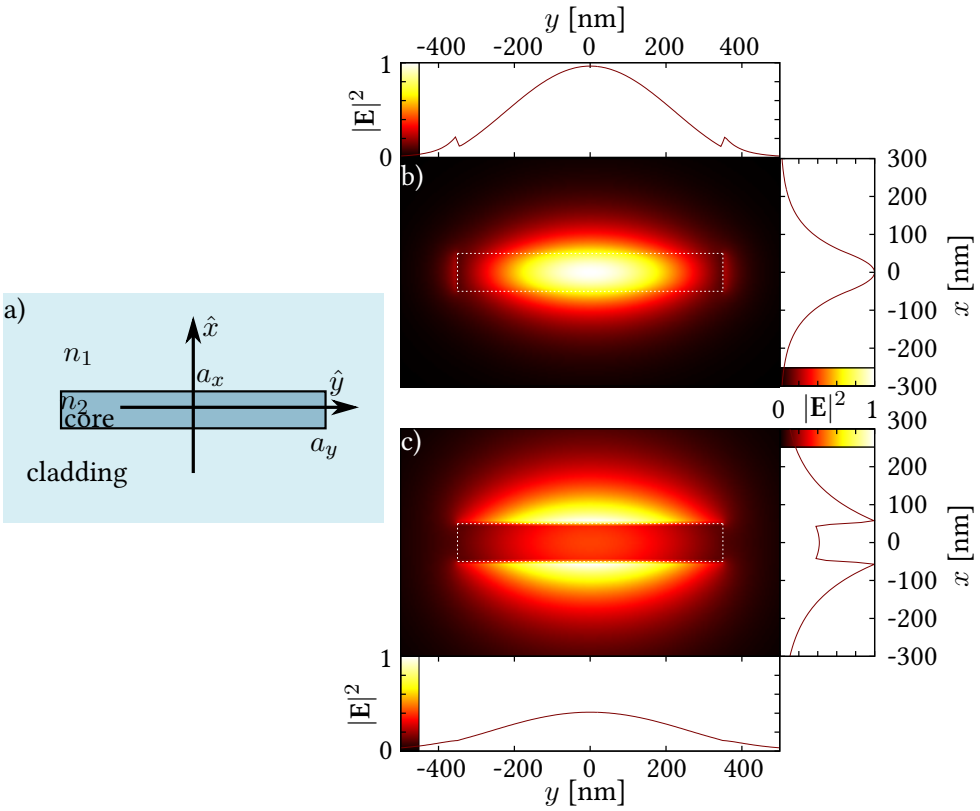

Figure 5.2.: a) Illustration of an rectangular waveguide of height 100 nm and width 700 nm. Such a structure is also known as buried channel waveguide or embedded strip waveguide. b) Two-dimensional color-coded plot of the electric field intensity of the quasi-TE fundamental guided mode of the waveguide at a wavelength of 650 nm. The mode profile of a central cut ($x = 0$) parallel to the y-axis is plotted above the color map and the central profile $y = 0$ parallel to the x(-axis is plotted on the left of the color map. c) The quasi TM mode is plotted in the same way as in b). The refractive indices are chosen in accordance to a Ta_2O_5-core ($n_2 = 2.1$) surrounded by fused silica ($n_1 = 1.46$). This structure supports a second higher order quasi-TE mode, which is not shown here.

5.1.1. Mode Profiles and Design of the Waveguides

The discussion of the mode profiles will start with basic aspects of a rectangular waveguide embedded in uniform cladding such as illustrated in figure 5.2 a). In a next step, a waveguide will be considered which is not covered by a dielectric but placed on a dielectric substrate. This section finishes with considerations about the waveguide design.

Due to the high aspect ratio cross-section the quasi TE and quasi TM modes, properties very similar to the pure TE and TM modes of the one-dimensional case (section 2.2) can be found. Even with moderate aspect ratios, a fundamental quasi TE and a fundamental quasi TM mode are supported. Like in the one-dimensional waveguide, those two modes are both fundamental modes as they do not experience a mode cut-off. The fundamental quasi-TE mode is plotted for an isotropically embedded single-mode waveguide in figure 5.2 b). This predominantly vertically $(\hat{y})$ polarized quasi TE-mode features an electric field, which is strongest inside the waveguide with evanescent field at the top/bottom as well as at the sides. The jump in the electric field E_y due to continuity relations (2.24) occurs at the dielectric interfaces at the left and right side of the waveguide but is less pronounced than for the nanofiber (compare section 2.3). In such an uniform cladding configuration there exists also a mainly vertically polarized quasi TM-mode (figure 5.2 c)). This mode has the highest intensity in the evanescent field above and below the waveguide and is less confined. The quasi-TM mode also features a strong[1] longitudinal component E_z at the upper and lower surface. As expected, this mode shows a very distinct discontinuity of the dominating the electric field component E_y. There is an additional second order quasi-TE mode supported by this structure at $650\,\text{nm}$ which is not shown here.

At this point, it has to be considered, that in order to place the emitter (e. g. a fluorescing diamond nanocrystal) on the waveguide surface, it must be accessible from the top. This can be realized with an uncovered waveguide on a glass substrate. Such an asymmetric cladding configuration changes the mode structure and effective indices. The quasi TE mode is slightly shifted into the substrate, whereas the quasi TM mode does not exist due to the strong asymmetry. Figure 5.3 a) illustrates this geometry and gives an example of the intensity distribution of the quasi TE-mode 5.3 b). The field components of a TE-mode are shown in figure 5.4. At the central mirror plane (including the x and z axis), E_z and E_y are zero due to the symmetry of the mode. So, for an emitter placed along this plane, coupling can only be expected when the dipole is oriented along the x-direction.

In order to enable efficient coupling of emitter's fluorescence to the waveguide, the electric field of the guided mode at the position of the emitter has to be maximized [28] (the theory for evanescent coupling is presented in section 2.1). Therefore, in a first step, the evanescent electric field (at the core-cladding interface) is maximized by reducing the height of the planar waveguide, yielding an optimal value of $100\,\text{nm}$. In a second step, the width of the waveguide is optimized to feature the multi-mode cut-off just at the high energy edge of the NV^-'s emission spectral range ($630\,\text{nm}$), which results in a width of $700\,\text{nm}$ (compare figure 5.5). This is done using a finite-element method (FEM) based mode solver (Mode Solutions from Lumerical).

[1] E_z has about half the value of E_y)

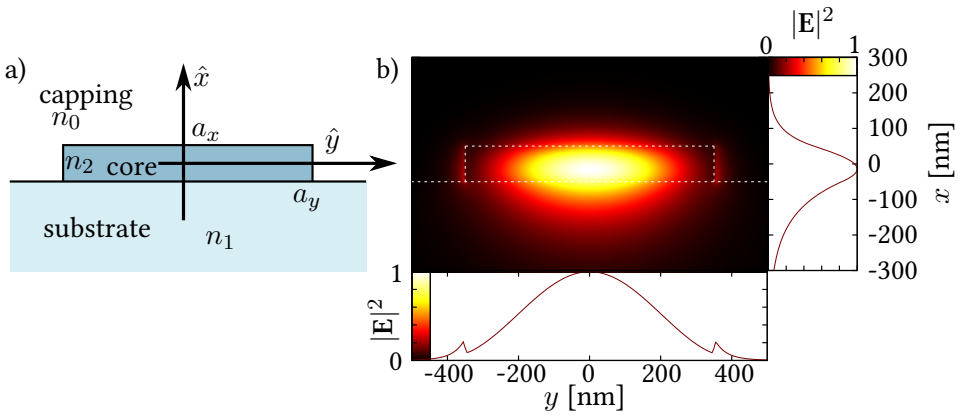

Figure 5.3.: a) Illustration of a waveguide with non-uniform cladding. Such a geometry with a substrate and a capping is common in experimental realizations. The necessary condition for a guided mode in the core is then given by $n_0 < n_1 < n_2$. Such a structure is often referred to as strip waveguide, channel waveguide or photonic wire waveguide. b) Intensity profile of such a waveguide with a height of 100 nm and a width of 700 nm is plotted for wavelength of 650 nm. Central cuts through the mode profile at $y = 0$ and $x = 0$ are plotted on the right and below the color map respectively. The refractive indices are $n_1 = 1.46$ (fused silica), $n_2 = 2.1$ (Ta_2O_5) and $n_0 = 1$ (air or vacuum).

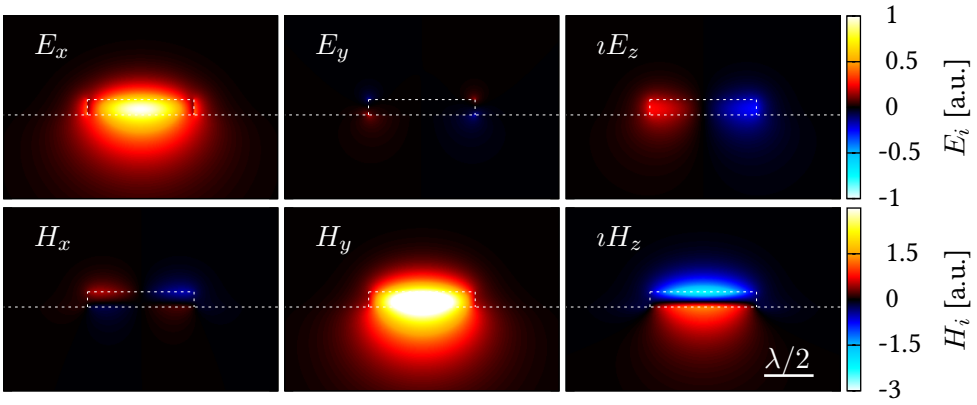

Figure 5.4.: Field components of the horizontally polarized (quasi-TE) fundamental mode with the same parameters as 5.3 (aspect ratio 1:7). The upper figures are $\mathrm{Re}(E_x)$, $\mathrm{Re}(E_y)$ and $\mathrm{Re}(\imath E_z)$ with identical scaling. In the lower row $\mathrm{Re}(H_x)$, $\mathrm{Re}(H_y)$ and $\mathrm{Re}(\imath H_z)$ are plotted with identical scaling, but multiplied by 1000 compared to the upper row.

During this discussion of rectangular waveguides, hybrid modes where found possessing similar properties as the basic TE and TM modes of a one-dimensional slab waveguide (section 2.2). The design of a strip waveguide with non-uniform cladding is used as a basis to design the waveguide which is produced for the experiment.

5.1.2. Dipole Coupling to Rectangular Waveguides

After the waveguide geometry is defined, numerical FDTD simulations are performed to estimate the expected coupling efficiency of a quantum emitter to the fundamental eigenmode (see figure 5.3 b)) with the quantum emitter modeled as a linear dipole positioned centered at the air-core interface.

As discussed in section 2.1, the properties of an emitter coupled to a waveguide can be described by two parameters, the coupling factor β and the emission enhancement factor α. Rectangular waveguides are only accessible via numeric procedures, therefore, both values will be derived from simulations. In contrast to section 4 discussing cylindrical waveguides, here the dimensions will not been shown in units of the vacuum wavelength λ but in absolute length. This is convenient as this rectangular structure is not defined by a single parameter, but by two parameters a_x and a_y. However, for a constant aspect ratio the general scaling with wavelength is still valid. Due to the fact, that right in the center of the waveguide only the x-component of the electric field is non-zero, coupling is only to be expected to a dipole oriented along the x-axis.

Numerical simulations of the mode profile for different wavelengths can be used to determine the mode dispersion $n_{\text{eff}}(\lambda)$. The FEM Eigenmode-Solver [93] directly outputs the dispersion $n_{\text{eff}}(\lambda)$ and the group velocity $n_{\text{gr}}(\lambda)$ which are shown in figure 5.5. In this graph the effective refractive index of the fundamental and first higher order quasi-TE mode are plotted, showing the clear mode cut-off at a wavelength, where the effective refractive index reaches the index of the substrate material.

From the simulated mode profile and the group index $n_{\text{gr}}(\lambda)$, the emission enhancement factor $\alpha(\lambda)$ can now be calculated. As the eigenmode expansion method [93] provides a discretized intensity distribution $\mathbf{E}(x_i, y_j)$ of the mode profile, a summation replaces the integral in the calculation of the emission enhancement factor α (2.10) yielding:

$$\alpha = \frac{\Gamma_{\text{wg}}}{\Gamma_{\text{iso}}} = \frac{3}{8\pi} \frac{c}{v_{\text{gr}} n^3(\mathbf{r}_0)} \frac{\lambda_0^2 E_x^2(\mathbf{r}_0)}{\sum_{i,j} \varepsilon(x,y) E_x^2(x_i, y_j)} \tag{5.1}$$

with the electric field $E_x(\mathbf{r}_0)$ at the position of the emitter $\mathbf{r}_0$. The resulting emission enhancement factor for different wavelengths is plotted in figure 5.7 a). The coupling factor β can be extracted from three-dimensional FDTD-simulations [37] of the structure in the same way as the simulation for the cylindrical waveguide in section 2.3.2. As shown in figure 5.7 b), the coupling is almost constant at about 35% for wavelengths from $500\,\text{nm}$ to $800\,\text{nm}$. It has to be pointed out that the coupling factor β, determined from the simulation, includes all possible modes in the waveguide. However, as the next higher order mode has a node in the central plane (see figure 5.6), coupling to this mode is not expected for a centered emitter.

As a third parameter, the expected increase in the overall emission rate $(\Gamma_{\text{wg}} + \Gamma_{\text{free}})/\Gamma_{\text{iso}}$ of the quantum emitter can be determined. This factor (see section 2.1) is given by the fraction of

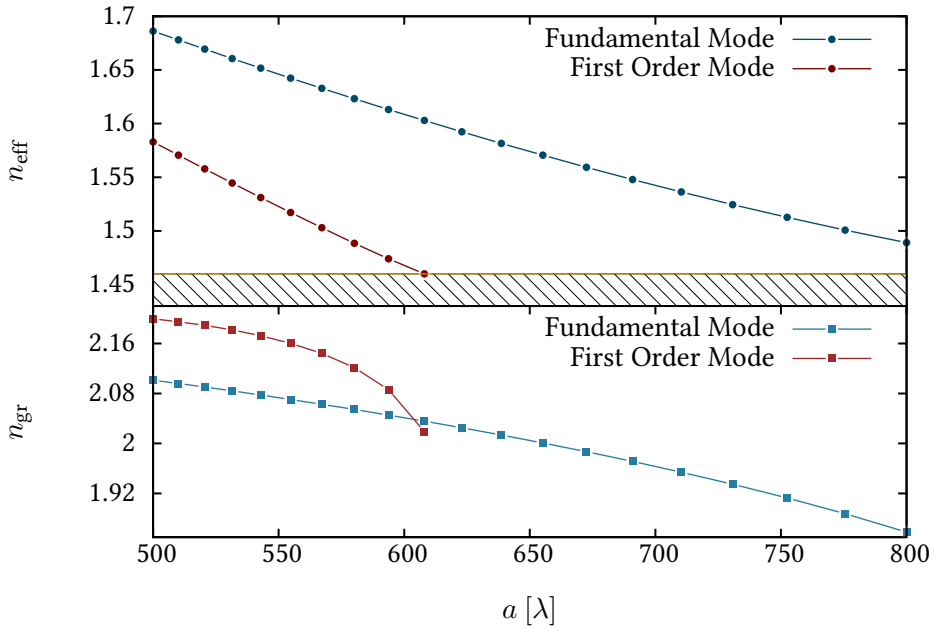

Figure 5.5.: Dispersion of a rectangular waveguide with a core of 700 nm in width and 100 nm in height and with a refractive index of $n_2 = 2.1$. The waveguide is placed on a glass substrate with a refractive index of $n_1 = 1.46$ and covered by air as sketched in figure 5.3. The upper plot shows the effective refractive index and the lower plot the group index. In both figures, the fundamental quasi-TE mode (see fig 5.6 a)) as well as the first higher order quasi-TE mode (see fig 5.6 b)) are plotted. The first higher order mode experiences a mode cut-off at a wavelength of 610 nm, where its effective refractive index of the mode penetrates the index of the substrate material (yellow line). Both graphs are obtained from eigenmode solving software [93].

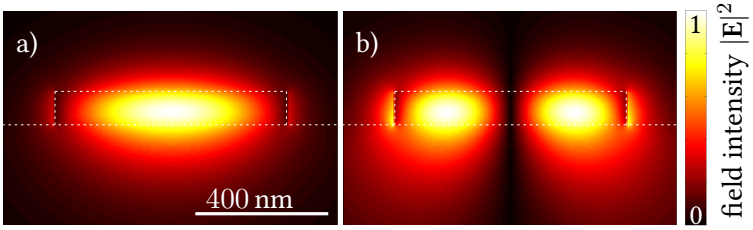

Figure 5.6.: Simulated mode profile $|\mathbf{E}|^2$ of the fundamental and the first higher order mode. The structure is the same as shown in figure 5.3 but with both modes calculated at a wavelength of 600 nm.

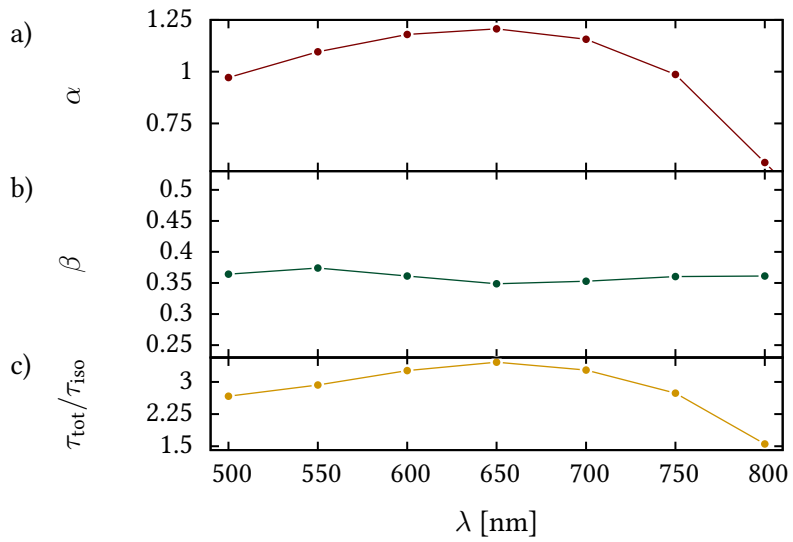

Figure 5.7.: Plot of the wavelength dependence of the three coupling parameters discussed in this section. All parameters are determined for a waveguide structure as shown in 5.3 (height of 100 nm and width of 700 nm), with a dipole placed above the waveguide, laterally centered.

the emission enhancement factor α and the coupling factor β. Its value is plotted as a function of the wavelength in figure 5.7 c) showing a maximum value above 3. This can be interpreted as a reduction in the excited state lifetime by this factor, due to the increase of the local density of optical modes (LDOS), for the coupled system.

In this section, the expected coupling of a dipole to the waveguide has been calculated. This derivation was based on numerically found mode profiles and full three-dimensional FDTD-simulations. Similar to analytic calculations with a dipole coupled to the nanofiber-section of a tapered optical fiber (chapter 4), a high broadband coupling efficiency (quantified by the coupling efficiency β) has been found yielding a typical values around 0.35 (figure 5.7).

5.2. Mode Conversion with an Inverted Taper

In order to transport the guided photons to other experimental devices, which are not integrated on the chip itself, efficient off-chip coupling to standard single-mode optical fibers is desired. Such combination of different waveguide types (e.g. single-mode optical fibers and on-chip waveguides) is useful to benefit from all their advantages. The off-chip coupling to optical fibers can be done with free-space optics and by direct contact. The so called end-fire coupling to free-space optics can be efficient, but as free-space optics are usually bulky, it is not desired in the context of integrated optics. In the literature, high off-chip coupling efficiencies have been reported with grating-couplers [32], but such systems are known to perform well

only for a narrow wavelength range. Another well established method for off-chip coupling is the butt-coupling technique, where two waveguide ends face each other. As the achievable coupling depends strongly on the mode overlap of the two waveguides, only a few percent of coupling efficiency can be expected when the strongly confined waveguide mode is coupled to a weakly confined mode of a standard optical fiber. However, an adiabatic tapering can be used to modify the mode shape and thereby increase the mode overlap. Mediated by such adiabatic mode-conversion, not only the butt-coupling efficiency, but also the collection efficiency for end-fire coupling with free-space optics can be increased by a great amount.

The approach used here is based on butt-coupling, mediated by an inverted in-plane tapering of the waveguide [94]. This promises high coupling efficiencies over a broad wavelength range.

In this section, first, the figure of merit for the coupling, the overlap of two modes, is introduced and the expected power coupling at a sudden discontinuity in the waveguide is described. Then, the adiabatic transition is discussed and finally, these findings are used to design a taper to increase the power-coupling between the strip-waveguide and the standard single-mode fiber.

5.2.1. Overlap Integral and Power-Coupling

In general, different modes can couple to each other if there is a discontinuity in the direction of propagation. Such a discontinuity might be an error from the fabrication process, a sudden but intended change in the waveguide geometry or even the end of the waveguide. In any case there is a set of input-modes E_ν and a set of output modes E'_μ (including radiative modes for a complete discussion). The complete set of input modes E_ν is a basis for all possible input photon wave functions and analogous, the complete set of output modes E'_μ is a basis for all possible output photon wave functions or states. The overall field is a sum of all modes with the amplitudes a_ν and a'_μ. Analogous to a basis-transformation, the input modes can be expressed in terms of the output modes [32]:

$$a_\nu E_\nu = \sum_\mu a'_\mu E'_\mu \qquad \text{with} \qquad a'_\mu = \frac{\langle a_\nu E_\nu, E'_\mu \rangle}{\langle E'_\mu, E'_\mu \rangle} \tag{5.2}$$

With this, the power per mode can be expressed as well in terms of the outgoing modes:

$$P'_\mu \propto |a'_\mu|^2 \langle E'_\mu, E'_\mu \rangle = |a_\nu|^2 \frac{|\langle E_\nu, E'_\mu \rangle|^2}{\langle E'_\mu, E'_\mu \rangle} \tag{5.3}$$

The coupled power is the ratio of the power in the output modes μ compared to the power in the input modes ν:

$$\eta_{\nu\mu} = \frac{P'_\mu}{P_\nu} = \frac{|\langle E_\nu, E'_\mu \rangle|^2}{\langle E_\nu, E_\nu \rangle \langle E'_\mu, E'_\mu \rangle} = \frac{|\int E^*_\nu E_\mu \, \mathrm{d}A|^2}{\int |E_\nu|^2 \, \mathrm{d}A \int |E_\mu|^2 \, \mathrm{d}A}$$

Here, the area A is the cross section at which the modes are calculated at and the asterisk ($*$) indicates the complex conjugate. The nominator is known as the overlap integral of the two modes. This is a measure for the similarity of the two modes. The denominator, on the other hand is a normalization factor [32].

The overlap integral is dominated by the inner product $\langle E_\nu, E_\mu \rangle$ of the input and output modes (ν and μ). As all modes of a waveguide are orthogonal [32], there is no coupling between modes in an unperturbed waveguide. Also, in a symmetric transition even modes can couple only to even modes and odd modes to odd modes. Furthermore, the overlap integral is also sensitive to the polarization. This property is maintained as well in an unperturbed waveguide, meaning that a mode, which is polarized in one direction can couple only to modes featuring the same polarization. The overlap integral is also symmetric in μ and ν, therefore, the coupling is the same in both directions. Additionally, the overall coupling, which is the sum over all $\eta_{\nu\mu}$, is always unity when all possible modes (guided and radiative) are considered and absorption can be neglected. However, in the actual experiment coupling to non-guided modes is often regarded as loss. Therefore, the interesting value is the sum over the coupling between the guided modes. Let the subscript g indicate the subset of modes which are guided, then the coupling is:

$$\eta_\mathrm{g} = \sum_{\nu,\mu=\mathrm{guided}} \eta_{\nu\mu} \tag{5.4}$$

The actual power coupling of two waveguides is not determined by the pure mode overlap but, as the propagation constants (or effective refractive indices) of the modes might differ, also reflections have to be considered. If the two modes coupled to each other show different effective refractive indices, reflections will reduce the coupled power according to the Fresnel's equations [30] to:

$$\eta_P = \left(\frac{n_{\mathrm{eff},\nu} - n_{\mathrm{eff},\mu}}{n_{\mathrm{eff},\nu} + n_{\mathrm{eff},\mu}} \right)^2 \eta_\mathrm{g} \tag{5.5}$$

Here, a sudden discontinuity was discussed, but changes in the waveguide geometry can also occur very slow or even adiabatic.

5.2.2. Adiabatic Taper

If the change in lateral size is very small while passing from one waveguide geometry to another, the initial mode E_ν is continuously transformed into a final mode E'_μ.[2] In such an adiabatic transition, at each point all modes are orthogonal which forbids mutual coupling among different modes. Therefore, each initial mode is transformed into a single, corresponding final mode (including radiative modes). E.g. in a symmetric configuration the fundamental mode of the initial waveguide will be transfered exclusively into the fundamental mode of the final waveguide. Therefore, during the transition from the initial to the final mode, the coupling efficiency is intrinsically unity as no power can be lost to other modes.

The condition for an adiabatic transition cannot be determined precisely. For wide one-dimensional waveguides, the ray-optics picture results in a condition of the tapering angle $\theta_t > \lambda/4n_\mathrm{eff}a$ [95, 96]. This condition is derived from the requirement of the angle between the waveguide sidewalls and all possible rays to be smaller than the angle of total internal reflection. However, for the inverted single-mode taper, this condition would result in an implausible short taper, which is not adiabatic. In the inverted tapering of strongly confined waveguides,

[2] This can be seen in direct analogy to the adiabatic theorem known from quantum mechanics [21].

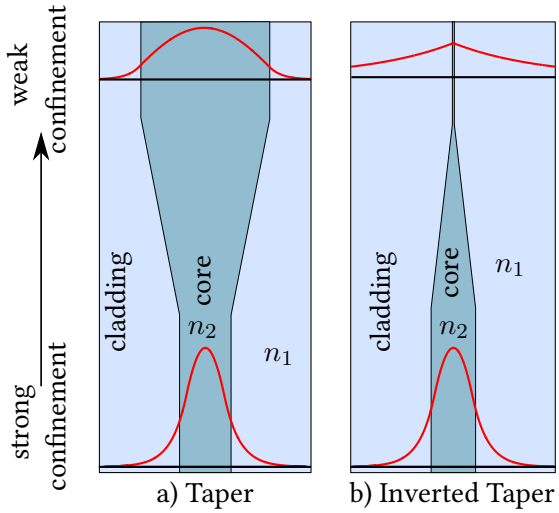

Figure 5.8.: Illustration of two types of adiabatic tapers. The arrow indicates the transition from a single strongly confined mode at the bottom to a large and weakly confined mode at the top. For both waveguides, exemplary TE-mode profiles ($E_y(x)$) are added (red) to illustrate the mode transformation due to the taper. a) An ordinary taper enlarges the waveguide itself, which increases the mode size. b) An inverted taper reduces the waveguide dimensions, which enlarges the mode by "squeezing" the mode out of the waveguide.

an intuitive condition is that the change of the waveguides dimensions per wavelength in the direction of propagation has to be negligible. However, this is no mathematically useful condition, therefore, the tapering angle can simplest be obtained from FDTD-simulations.

Such an adiabatic transition can be used to couple a strongly confined waveguide mode efficiently to a weakly guiding waveguide like an optical fiber. For such purpose, several different types of tapers can be used, the ordinary taper, the inverted taper and also stacks and combinations (see figure 5.8).

In ordinary tapers (figure 5.8 a)), the size of the waveguide increases along the propagation direction and therefore, the mode widens. Starting with a single-mode waveguide, at some point the waveguide can reach the multi-mode regime. However, if the transition is adiabatic, only the fundamental mode will be occupied. This process is reversible but it has to be noted, that higher order modes will not be transmitted through to the single-mode waveguide. The effective refractive index of the widened mode is reaching the core index, which is relevant to optimize the power-coupling. The mode profile will resemble the shape of the core, which will show a very high aspect ratio for lateral tapering.

Alternately, when starting from a highly confined waveguide mode, a reduction in waveguide size will also result in an increase of the mode size, as it is squeezed out of the waveguide (figure A.2 and A.5 illustrate mode-profiles for different waveguide widths). This inverted taper (figure 5.8 b)) will be single-mode all the way. The effective index of refraction approaches the value of the cladding. This type of taper allows to create mode sizes much bigger than the structure itself and its shape becomes circular and is independent of the actual shape of the

waveguide. The actual mode size is very sensitive to the width at the end of the taper. An extension of the taper tip is indicated a the top-end of the taper in figure 5.8 b), which can be used in the experimental realization to ensure the correct end-width of the taper. This type of taper is fully reversible as both ends support the fundamental mode only. The realization of such an inverted taper structure is presented subsequently in section.

More advanced structures can be built by sequencing or stacking different tapers with different materials. A special and very elegant version of a combined taper is the tapered optical fiber as discussed in chapter 4.

5.2.3. Design of the Inverted Taper

In the investigation of the waveguide samples, the on-chip single-mode waveguides with a highly confined mode have to be coupled to a weakly guided single-mode fiber. Here, an adiabatic inverted tapering of the waveguide width has been chosen to convert the mode to a size matching that of the single-mode fiber.

In an adiabatic taper, the mode is everywhere an eigenmode of a waveguide for that specific geometry. Therefore, once having found the waveguide width which features the mode profile with the highest mode overlap to a standard optical fiber, the end-width of the taper can be fixed to that width. A roughly circular symmetric mode shape is needed to achieve good coupling. Waveguides of size significantly below the wavelength feature such a circular symmetric mode if the cladding surrounding the waveguide is homogeneous. This situation can be realized by embedding the waveguide in the substrate material. Therefore, the tapered regions have to be covered by glass. By simulating the eigenmodes of such thinned waveguides, the width providing the best mode overlap with a standard optical fiber for the wavelength range from $630\,\text{nm}$ to $680\,\text{nm}$ has been found to be $110\,\text{nm}$. For this end-width, the theoretical power-coupling is above -$0.7\,\text{dB}$ (85%) in the desired spectral region and peaks at about $658\,\text{nm}$ with above -$0.45\,\text{dB}$ (90%). These values promise a huge improvement of the coupling with the help of an inverted taper. Compared to this, the butt-coupling efficiency without any modification is expected to be below 10%. Here, it has to be noted, that the optimum width has a low tolerance[3] to errors, e.g. a deviation of few nanometers can significantly reduce the coupling efficiency (as shown via an eigenmode solving in [97]).

Another important parameter in the design is the length (steepness) of the inverted taper. The problem of finding the shortest taper for which it is still adiabatic is addressed by two-dimensional FDTD-simulations [37] of the tapering plane (y-z plane). These simulations have been performed for several taper lengths while monitoring the guided and scattered fractions of the input beam. It has been found that a taper length (starting with a width of $700\,\text{nm}$ down to $110\,\text{nm}$ width) of above $40\,\mu\text{m}$ shows no scattering losses in the simulations. For the experimental realization of the taper, twice the length (about $80\,\mu\text{m}$) has been chosen. The shape of the taper can be chosen in different ways which can be of further advantage [98], however, to keep the design simple, the inverted taper for the realized structures is designed as linear taper.

[3] For waveguide widths significantly below the wavelength, the decay length of the evanescent field of the one-dimensional waveguide has been found to scale with the reciprocal waveguide width $1/a$ (section 2.2).

5.3. Fabrication

For the waveguides and especially the taper structures a fabrication technique is needed, which allows to produce patterns with feature sizes down to 100 nm. Photolithography, which is widely used in industry, is capable to produce sizes of a few tens of nanometers [99] in highly optimized processes. However, without such extensive optimization the achievable structure sizes are hardly below 1 µm. Therefore, for this work an alternate lithography method was chosen, the electron beam lithography (EBL). With a moderate optimization afford, electron beam lithography allows for structure sizes far below 100 nm [100]. Additionally, as the pattern were written directly computer-controlled in a CAD-like interface, structures can be modified easily, resulting in a very short test cycle. The second key technology used to fabricate the waveguides and inverted tapers is the reactive ion etching (RIE). The nanofabrication of the waveguide structures proceeds as follows (see figure 5.9) (further details can be found in [101]).

The sample wafer consists of a synthetic fused silica substrate, coated with a 100 nm thick layer of Ta_2O_5 in a sputtering process (by asphericon GmbH, Jena, Germany). The sample is prepared with a variety of cleaning steps including a bath in dimethyl sulfoxide (DMSO) at 90° C and oxygen plasma ashing. For the electron beam lithography (EBL) the sample is first spin-coated (1s at 800 rpm and 30s at 5000 rpm) with PMMA (950k A4 from Microchem) as a electro-sensitive resist for the EBL and then soft-baked on a hotplate for 15 min at 170°C. This results in a PMMA-layer thickness of about 190 nm. Then, the sample is spin-coated (30 s at 2000 rpm) with a conductive polymer (SX AR-PC 5000/90.1, Allresist GmbH), which acts as a discharge layer during the electron beam exposure. Compared to a standard metal discharge layer (e. g. chromium), a conductive polymer promises a reduction in sidewall-roughness [102] of the structures.

The electron beam lithography (EBL) of the waveguides and inverted tapers is performed with a Raith e_LiNE with an applied acceleration voltage of 10 kV. The waveguides and the inverted tapers are written with an optimal dose of 95 µC/cm^2. The writing order of the different elements and their positioning within the write field[4] is essential to ensure minimal stitching errors (an example for the stitching of two write fields is presented in figure 5.9): First one taper is written by deflecting the electron beam while the stage has a fixed position (vector/area mode). Second, the waveguide is written with a circulating beam while the sample stage moves with constant velocity (fixed beam moving stage, FBMS). Third, the taper at the end is written, again with in vector mode. Both tapers-tips are elongated with a single pixel line (see figure 5.10) to ensure the correct end-width of the taper. Immediately after EBL exposure, the conductive polymer is removed with clean nitrogen gas and de-ionized water (LicoJET mini high pressure cleaner, Lico-Tec GmbH). The PMMA is developed in 3:1 IPA:MIBK with 1.5% MEK at room temperature for 50 s, followed by a short cleaning-step in IPA. This removes the parts of the PMMA resist layer, which were exposed prior to the electron beam. Now, the sample is coated with the hard mask material (8 nm of chromium) using an electron beam evaporator in

[4] The term "write field" refers to the area the electron beam can access via deflection and without movement of the sample stage. To minimize stitching errors any movement of the sample stage without writing has to be avoided. By design, the point where the taper is connected to the waveguide is preferably right in the center of its write field. This reduces the stitching error as no stage movement is necessary between the patterning of the taper and the waveguide.

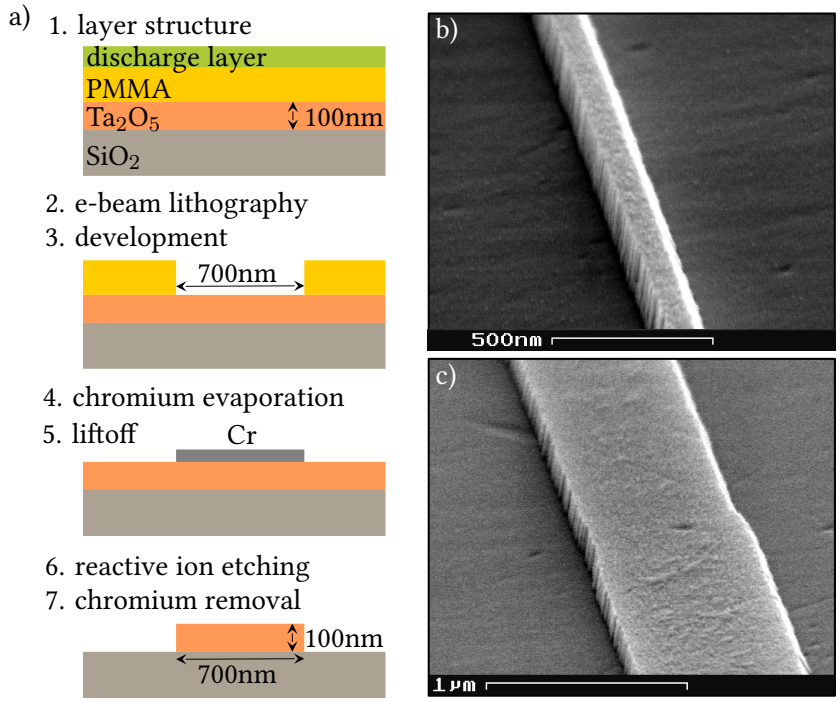

Figure 5.9.: a) Illustration of the main nanofabrication steps used to structure the planar strip-waveguides. Scanning electron microscope (SEM) images of b) the inverted taper close to its minimum width and c) the transition of the waveguide to the inverted taper after reactive ion etching.

a high vacuum coating plant. The subsequent liftoff is mediated by preheated DMSO at 90° C for more than 2 hours. Finally the sample is rinsed with acetone and IPA to remove any residual contaminants. The hard mask pattern is transfered to the Ta_2O_5 with inductively coupled plasma reactive ion etching (ICP-RIE) in an Oxford Instruments Plasmalab System 100. SF_6 is used as processing gas diluted with Ar (4:1 in volume) at a pressure of 5 mtorr. The ICP-power was optimized to 70 W with a RF-power of 100 W. With these parameters the 100 nm layer of Ta_2O_5 is removed completely within 1:40 min. Finally, the hard-mask is removed with a liquid chromium etchant.

For optimal performance of the mode conversion in the adiabatic inverted taper and protection of the whole waveguide structure, the chip is covered with the same refractive index as the substrate. Therefore, in a last step, a layer of 3 µm of SiO_2 is sputtered on top of the waveguides. In order to retain an area, where the waveguides are sensitive to emitters, a small part of the waveguide is masked during the sputtering process. The sample end facets were finished with an fiber polishing machine and diamond-covered polishing pads commercially available (Ultratec Minipol) for standard FC/PC standard fibers. After the polishing process of the end facets no scratches and distortions were visible in an optical microscope.

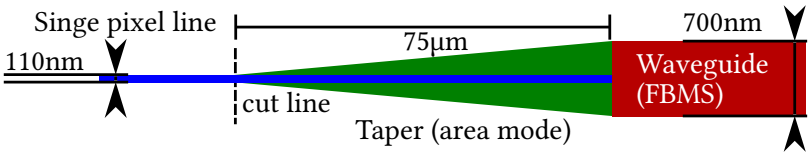

Figure 5.10.: Design of the inverted taper (not to scale). From left to right: Single pixel line (blue), the electron beam writes a single line. The width of the single pixel line is defined by the electron dose (current per writing speed) via the designated area. Both, the SPL and the taper (green) are written in the vector scanning or area mode. The waveguide (red) is written in the FBMS-mode (fixed beam moving stage), where the electron beam circulates to create the waveguide width while the sample stage moves. The transition from taper to waveguide has been found to be smoothest when there is neither an overlap nor a gap by design. Proximity effect correction methods have not been applied but could further optimize the structures.

5.4. Transmission and Off-Chip Coupling

The transmission, or propagation length, is an essential factor which quantifies the performance of waveguides. This section is concerned with the determination of the propagation loss per length and, simultaneously, evaluates the butt-coupling performance of the inverted tapers.

The electric field intensity and therefore also the power which is propagating in a guided mode can dissipate due to material absorption or scattering into radiative modes. The scattering can be caused by intrinsic material defects, polarizable particles within the evanescent field, or imperfections of the waveguide surface. As such scattering centers couple guided to radiative modes, also light propagating in free space can be coupled into the waveguide mode. A similar behavior has been found with the tapered optical fiber (chapter 4), where the excitation laser is partially coupled into the nanofiber mode via the Rayleigh-like scattering at the diamond nanocrystal.

If the absorbing or scattering centers are distributed along the waveguide the propagation loss can be described in statistical terms as a mean loss per length. The loss per scattering or absorbing center is proportional to the local power in the mode, therefore, the guided power per propagation length z can be described as an exponential decay with the decay rate B:

$$P(z) = P_0 \exp(-\frac{z}{B}) \tag{5.6}$$

The most intuitive way to measure propagation losses is to evaluate the overall transmission of the waveguide with length z. But, in such a measurement, propagation losses and in-coupling/out-coupling losses cannot be discriminated. This problem can be solved in a measurement of the waveguide transmission with several different waveguide lengths z. This will change the total contribution of the propagation loss but keeps the coupling efficiencies constant. This cut-back method [103] is applied in the following to determine the propagation loss as well as the in-coupling efficiency mediated by the inverted taper. On the logarithmic scale, the total transmission loss L_{total} introduced by the waveguide is given by the sum of the in-

coupling loss L_{in}, the propagation loss l_{prop} times propagation distance d, and the out-coupling loss L_{out}:

$$L_{\text{total}}(d) = L_{\text{in}} + L_{\text{out}} + l_{\text{prop}} \cdot d. \tag{5.7}$$

A linear fit of the measured total transmission loss L_{total} for different waveguide lengths d allows to determine the propagation and insertion losses.

The cut-back measurement is performed with a waveguide sample with an inverted taper on one side only. The sample is shortened from the side without taper to keep the in- and out-coupling mode geometries constant. In order to determine the transmission, probe laser light (wavelength: $658\,\text{nm}$), guided by a polarization compensated single-mode fiber is coupled into the waveguide via butt-coupling to the inverted taper (see illustration in Fig.: 5.1 from left to right). The light emerging from the output of the waveguide is collected with a microscope objective and can be imaged with a CCD or its intensity quantified with a photo-detector. Without inverted taper, the high mode confinement results in a high divergence of the output mode. Within the numerical aperture of the objective (NA$= 0.65$), 62.3% of this mode can be collected[5] (obtained from simulations of the waveguide mode-profile). This value is the maximum achievable out-coupling efficiency L_{out} in this configuration and, therefore, an upper theoretical limit for all measurements. The unprocessed transmission data is plotted against the waveguide length in figure 5.11.

From this data, a propagation loss l_{prop} below $1.8\,\text{dB/mm}$ as well as an insertion loss via the inverted taper L_{in} below $2.4\,\text{dB}$ (57% coupling efficiency) were obtained for at least two of the 4 waveguides (the results of the cut-back measurements are summarized in table 5.1). A alternate common method of obtaining the propagation losses is the stay light analysis. In the regime where the propagation length is limited by scattering to radiative modes, this scattered light can be analyzed by simply imaging a top ode side view of the waveguide onto a CCD-camera. If the propagation loss is distributed equally along the waveguide, the scattered power is proportional to the guided power and, therefore, the expected exponential decay rate B (see equation (5.6)) can be extracted from the CCD-image. This procedure is performed on waveguides created in the same way as this sample in [104] and compared to the cut-back method of the same sample. The scattered-light analyses results in substantially lower propagation losses with higher accuracy than obtained from the cut-back method. Four waveguides showed propagation losses from $1.5\,\text{dB/mm}$ to $2\,\text{dB/mm}$.

The sample investigated here is completely covered by a SiO_2 capping layer. Another sample produced identically, but partially covered during the sputtering process of the capping layer has been investigated in the same setup and geometry for a single length, showing about a factor of 2 lower total transmission.

5.5. Summary

A dielectric on-chip waveguide has been designed to provide a versatile platform for on-chip experiments in quantum information science and sensing applications. The waveguide promises

[5] The precise experimental determination of this value is challenging, mainly due to the strong stray-light which guided by the capping layer

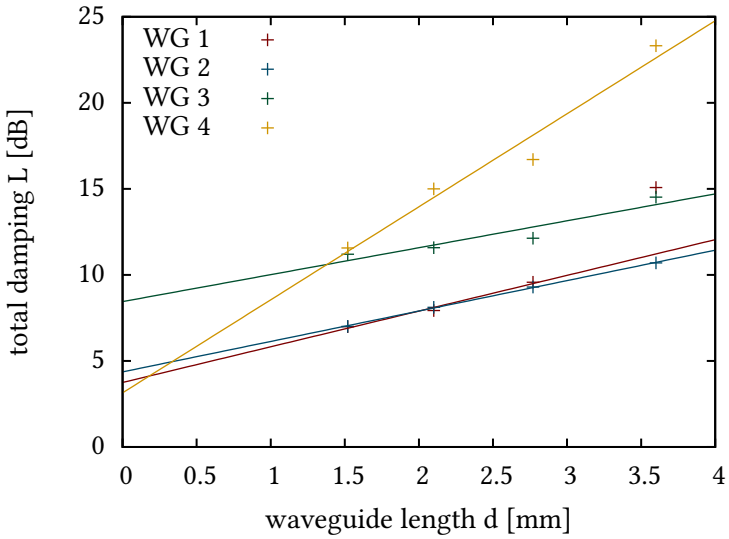

Figure 5.11.: Total losses of four waveguides in one sample for different sample-lengths obtained with the cut-back method. The value for waveguide 'WG 1' at 3.6 mm has not been included into the linear fit as this waveguide showed a strongly scattering defect.

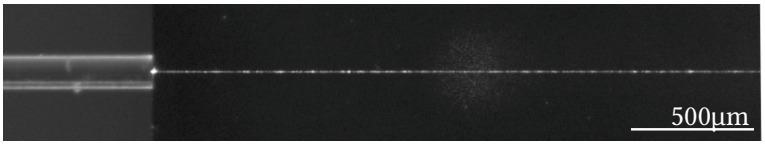

Figure 5.12.: Top-view photograph of the stray-light emitted by the waveguide illuminated by a probe laser at 658 nm (right) which is butt-coupled via a single-mode fiber (left).

Waveguide	Prop. loss	Insertion loss
1	(2.07 ± 0.24) dB/mm	(1.69 ± 0.53) dB
2	(1.77 ± 0.03) dB/mm	(2.31 ± 0.08) dB
3	(1.56 ± 0.40) dB/mm	(6.39 ± 1.05) dB
4	(5.40 ± 0.76) dB/mm	(1.09 ± 1.99) dB

Table 5.1.: Table with propagation losses and insertion losses for 4 waveguides of the same sample, obtained from the slope and the y-axis intercept of a linear fit to the total transmission for 4 different lengths, using the cut-back method (figure 5.11). The values of the insertion loss are obtained by subtracting the simulated value for the out-coupling loss, introduced by the limited NA of the collection optics ($L_{\text{out}} = 0.632$), from the y-axis intercept provided by the linear fit. The error-ranges originate from the least square fit asymptotic standard errors.

moderate coupling efficiencies of about 35% to a dipole placed on its surface and aligned parallel to the wide axis of the waveguide. In order to realize first test samples, a fabrication process has been developed based on nanofabrication techniques such as electron beam lithography and reactive ion etching. The electron beam lithography process allows to pattern continuous waveguides of several millimeters in length which can be connected to arbitrary structures without stitching errors. The overall process was optimized to produce reproducible results showing waveguide propagation losses below 1.8 dB/mm at 658 nm wavelength. As waveguides with high mode confinement are very sensitive to disturbances of its surface and the test samples show a certain sidewall-roughness (figure 5.9), this can be assumed as the main cause limiting the propagation length. In the literature, propagation losses as low as 0.4 dB/cm have been reported [105] using the same material system (Ta_2O_5 on SiO_2), but with larger dimensions (200 nm $\times$ 2-10 µm) and light with a longer wavelength (1070 nm). This larger dimensions result in a lower mode confinement and therefore to a lower sensitivity to sidewall roughness. However, with a system more comparable in geometry, Fu et al. [106] found propagation losses of (4.6 ± 3) dB/mm (wavelength 637 nm) for a rig waveguide of 1 µm in width and 160 nm in height of GaP ($n_{\mathrm{GaP}} \approx 3.2$) on diamond ($n_{\mathrm{C}} \approx 2.4$).

An inverted taper is added to the waveguide to provide efficient off-chip coupling to standard single-mode fibers by extending the waveguide mode to achieve high mode overlap with the fiber. For the fabricated samples, the off-chip coupling efficiency has been measured to be up to 57%, which is a big improvement compared to direct butt-coupling [107, 108, 97, 101].

After the positioning of the fluorescing diamond nanocrystal, the sample can be protected by a sputtered layer of glass. The guided mode will change slightly, but no significant change in the coupling efficiency is expected. However, the diamond nanocrystal might stop fluorescing either due to the changed surface termination of the diamond crystal or to thermal effects during the sputtering process. In a first test, about one half of the fluorescing diamond nanocrystals stopped fluorescing after being covered by sputtered SiO_2 [109].

With the values achieved for propagation length and off-chip coupling, combined with the expected coupling-efficiency from the emitter to the waveguide, a total coupling from the emitter to a standard fiber-coupled APD-detector of above 10% is in reach.

6. Conclusion and Outlook

Within this work, the light matter interaction of a single quantum emitter with a single guided optical mode has been discussed and demonstrated. For this purpose, a single nitrogen-vacancy center hosted in a diamond nanocrystal has been placed deterministically in the evanescent field of the waist of a tapered optical fiber (TOF). With this system, the coupling of the emitted fluorescence photons into the fiber has been proven based on the measured photon statistics. The measured coupling efficiency of this system of $(10 \pm 5)\%$ is a promising starting point for future applications in ultra-sensitive phase [110, 8, 111], absorption [112], and fluorescence spectroscopy. Furthermore, as a single quantum emitter can shift the phase of a propagating laser beam by several degrees, this level of nonlinearity would, for instance be sufficient to provide an useful photon-photon interaction for optical quantum information science [113, 26].

This demonstrated evanescent coupling principle has the advantage of being very simple and compact in construction. The space-saving properties of this coupling technique can be especially beneficial in integrated nanooptical devices. As first step towards such a device, an integrated on-chip waveguide has been designed to serve as a platform for demonstration of on-chip experiments. These strip waveguides provide high mode confinement, broadband evanescent coupling similar to the TOF and single-mode operation at the wavelengths of the NV-center's emission. As part of the design, an inverted taper has been developed and tested, which converts the highly confined waveguide mode to reach high mode-overlap with standard single mode fibers. These strip waveguides including the inverted taper off-chip couplers have been realized on first test samples featuring propagation losses below 2 dB/mm and off-chip coupling efficiencies up to 57%.

In the near future, besides the experimental demonstration of the coupling of an emitter to the waveguide mode, improvements in the propagation length are planned. The inherent island-like growth of the chromium hard-mask seems to be responsible for a variation in the resistance of the mask to the etching. Therefore, this structure of the chromium mask is imprinted onto the sidewalls of the waveguides. As chromium is the metal known for growing in the smallest islands, a modified fabrication process is being tested, using HSQ as electron beam resist. This developed HSQ (hydrogen silsesquioxane) can be used directly as mask for the reactive ion etching promising smoother structures. Initial test structures already featured sizes below 30 nm [114].

The derivation of the mode-profiles of the transverse magnetic (TM) mode in the one-dimensional waveguide (section 2.2) showed that the electric field vector perpendicular to an dielectric interface can feature a strong enhancement of the electric field amplitude on the low-index half-space (evanescent field). In the discussion of the nanofiber (section 2.3.2), this enhanced amplitude has been found to allow a high emission enhancement factor α and good coupling efficiencies β. This effect of enhanced evanescent coupling close to an interface can be exploited further if this interface can be brought to the position of the field maximum. This can

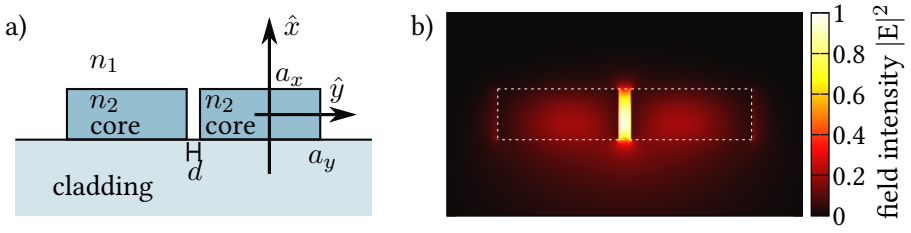

Figure 6.1.: a) Illustration of a possible realization of a slot waveguide and b) intensity profile of the fundamental mode of such a structure. The mode of the slot-waveguide of 100 nm in height, 700 nm in width and a 50 nm wide slot is calculated for a wavelength of 650 nm. The refractive indices are $n_1 = 1.46$ (fused silica), $n_2 = 2.1$ (Ta_2O_5) and $n_0 = 1$ (air or vacuum).

be realized by creating a small vertical slot inside the rectangular shaped waveguide, as it is discussed in section 5. With such a slot, the fundamental horizontally polarized mode features a strong ($E_{y,\,\text{slot}} \approx n_2^2 E_{y,\text{no slot}}$) and extremely confined evanescent field within the slot (illustrated in figure 6.1). Such a slot waveguide promises extraordinary broadband coupling ($\beta > 90\%$) and high emission enhancement factors ($\alpha > 100$ [28]) for a dipole placed inside such a slot [26, 115, 116, 117, 118, 119, 120].

The broadband-coupling via the evanescent field is beneficial in combination with emitters with broadband emission like the nitrogen-vacancy center. However, any small solid-state based emitter can be used in the same way. In the past years, many alternate fluorescent defect-centers have been identified, synthesized and characterized. One of the most promising alternatives to the NV-center is the silicon-vacancy center in diamond [121, 122, 123, 124]. This system shows a short excited state lifetime, enabling high emission rates, low sensitivity to external fields, spectrally stable emission wavelength and a high Debye-Waller factor (more than 70% of the emission is in the zero-phonon line [122]). However, to this date, the production of diamond nanocrystals hosting single SiV-centers is a matter of ongoing research (e. g. [125]). Such emitters will bring new aspects to this experiment.

Providing such a narrow band emitter, the optical resonators like cavities become interesting. There are several possible ways to implement cavity structures coupled to the TOF and the on-chip waveguide-device. Distributed Bragg reflectors and the coupling to toroid resonators can be utilized with TOFs [126, 127, 128], [129] as well as with on-chip waveguides [130],[131, 132]. The combination of an evanescently coupled narrow-band emitter to a waveguide with optical cavity can improve the coupling efficiency to a great amount (exceeding 90%) [130, 133, 126]. This will pave the way towards the realization of an efficient single photon source at room temperature, an essential building block of photonic quantum computing [5, 6, 7]. Such single photon sources can also be combined with directional couplers [134] and phase shifters to build complex networks in on-chip experiments [135].

In essence, this work has demonstrated the potential of evanescent coupling as a basis for an efficient and compact single photon source. Furthermore, this evanescent coupling shows great potential in nanooptical on-chip experiments in quantum information science and sensing.

A. One-dimensional Dielectric Waveguides - Detailed Derivation

In this appendix, the basic figures of merit of a guided electro-magnetic wave traveling in a one-dimensionally confined waveguide will be derived directly from Maxwell's equations. This derivation is equivalent to the section 2.2, but mathematically more rigorous.

Solutions of Maxwell's Equations for the One-Dimensional Waveguides

Dielectric waveguides are based on materials with different dielectric constants and hence different refractive indices. As the wavelength λ of the traveling light is not close the energy of atomic transitions in the material, the dispersion of the materials can be neglected ($\frac{\mathrm{d}\varepsilon}{\mathrm{d}\lambda} = 0$). Further assuming, that no static electric charges or currents are present, the macroscopic Maxwell's equations describing the electro-magnetic fields as function of time t and position r, can be written in their differential form as:

$$\nabla \times \mathbf{E}(\mathbf{r}, t) + \frac{\partial \mathbf{B}(\mathbf{r}, t)}{\partial t} = 0 \tag{A.1a}$$

$$\nabla \times \mathbf{H}(\mathbf{r}, t) - \frac{\partial \mathbf{D}(\mathbf{r}, t)}{\partial t} = 0 \tag{A.1b}$$

$$\nabla \cdot \mathbf{D}(\mathbf{r}, t) = 0 \tag{A.1c}$$

$$\nabla \cdot \mathbf{B}(\mathbf{r}, t) = 0 \tag{A.1d}$$

E, **D**, **B**, and **H** are the complex vector fields of the electric field and the electric displacement field as well as the complex pseudovector fields of the magnetic field, and the magnetizing field, respectively. Additionally, there are relations governing the material properties:

$$\mathbf{B}(\mathbf{r}, t) = \mu_0 \mathbf{H}(\mathbf{r}, t) \tag{A.2a}$$

$$\mathbf{D}(\mathbf{r}, t) = \varepsilon(\mathbf{r}) \mathbf{E}(\mathbf{r}, t) \tag{A.2b}$$

Here, the dielectric permittivity $\varepsilon(\mathbf{r}) = \varepsilon_0 \varepsilon_r(\mathbf{r})$ is allowed to be varying with position according to the structured dielectric materials. As common for dielectrics, the relative magnetic polarization μ_r of the material is neglected.

Now, the curl ($\nabla\times$) can be applied to the first Maxwell's equations (A.1a) and using equation (A.2a) as well the Laplacian operator $\nabla \times \nabla \times \mathbf{E}(\mathbf{r}, t) = \Delta\mathbf{E}(\mathbf{r}, t)$. Equation (A.1a) can then be expressed as:

$$\Delta\mathbf{E}(\mathbf{r}, t) + \mu_0 \frac{\partial}{\partial t} \nabla \times \mathbf{H}(\mathbf{r}, t) = 0 \tag{A.3}$$

The analogous equation for the magnetic field H can be derived from (A.1b) and (A.2b):

$$\Delta\mathbf{H}(\mathbf{r}, t) - \varepsilon(\mathbf{r}) \frac{\partial}{\partial t} \nabla \times \mathbf{E}(\mathbf{r}, t) = 0 \tag{A.4}$$

Let these functions be well-behaved, meaning it is allowed to change the order of temporal and spacial derivatives, then it follows:

$$\left(\Delta + \frac{n^2(\mathbf{r})}{c^2} \frac{\partial^2}{\partial t^2}\right) \mathbf{E}(\mathbf{r}, t) = 0 \tag{A.5a}$$

$$\left(\Delta + \frac{n^2(\mathbf{r})}{c^2} \frac{\partial^2}{\partial t^2}\right) \mathbf{H}(\mathbf{r}, t) = 0 \tag{A.5b}$$

The material properties can be expressed in terms of the refractive index n and the vacuum speed of light c using the relations:

$$c^2 = (\mu_0 \varepsilon_0)^{-1}, \qquad n^2(\mathbf{r}) = \varepsilon_r = \varepsilon(\mathbf{r})/\varepsilon_0 \tag{A.6}$$

Considering a monochromatic wave with a single angular frequency ω, then the time dependency of the electric field and the magnetizing field can be written as an harmonic oscillation:

$$\mathbf{E}(\mathbf{r}, t) = \mathbf{E}(\mathbf{r}) e^{i\omega t} \tag{A.7a}$$

$$\mathbf{H}(\mathbf{r}, t) = \mathbf{H}(\mathbf{r}) e^{i\omega t} \tag{A.7b}$$

yielding the stationary solution:

$$\left(\Delta - \frac{\omega^2}{c^2} n^2(\mathbf{r})\right) \mathbf{E}(\mathbf{r}) = 0 \tag{A.8a}$$

$$\left(\Delta - \frac{\omega^2}{c^2} n^2(\mathbf{r})\right) \mathbf{H}(\mathbf{r}) = 0 \tag{A.8b}$$

At this point, the dielectric structure has to be defined. In order to allow propagation direction $\hat{z}$, a waveguide structure can be used, which enables confinement of the light in two dimensions $(\hat{x}, \hat{y})$. This can be realized by a step function of the refractive index in x and y but invariant of z.

$$n(\mathbf{r}) = n(x, y) \tag{A.9}$$

The free propagation in $\hat{z}$ can be expressed in terms of a free propagation constant $k_z = \omega/c$, which is modified by the effective refractive index n_{eff}:

$$\mathbf{E}(x, y, z) = \mathbf{E}(x, y) e^{-\imath n_{\text{eff}} k z} \tag{A.10}$$

resulting in:

$$\frac{\partial^2 \mathbf{E}}{\partial x^2} + \frac{\partial^2 \mathbf{E}}{\partial y^2} + \left(n^2(x,y) - n_{\text{eff}}^2\right) k_z^2 \mathbf{E} = 0 \tag{A.11a}$$

$$\frac{\partial^2 \mathbf{H}}{\partial x^2} + \frac{\partial^2 \mathbf{H}}{\partial y^2} + \left(n^2(x,y) - n_{\text{eff}}^2\right) k_z^2 \mathbf{H} = 0 \tag{A.11b}$$

In order obtain simple analytical results, the dimensionality of the system can be reduced. To do so any variation in the $\hat{y}$-direction is neglected. This is now a one-dimensional waveguide as the confinement is in one dimension. In the this section, solutions of the wave-equations for this one-dimensional waveguide will be derived analytically (see figure 2.2).

TE- and TM-Modes

Let the mode be confined in $\hat{x}$ and the structure be invariant in $\hat{y}$ and $\hat{z}$. $\hat{z}$ is chosen to be the direction of propagation, which implies:

$$\frac{\partial E_x}{\partial y} = \frac{\partial E_y}{\partial y} = \frac{\partial E_z}{\partial y} = 0 \qquad \text{and} \qquad n(\mathbf{r}) = n(x) \tag{A.12}$$

This reduces the electric field to:

$$\mathbf{E}(x,y) = \mathbf{E}(x) = \hat{x} E_x(x) + \hat{y} E_y(x) \tag{A.13}$$

This is a basis consisting of two orthogonal polarized modes, the so called transverse electric (TE) and the transverse magnetic (TM) mode:

$$\text{TE:} \qquad E_y \neq 0, E_x = 0 \tag{A.14}$$

$$\text{TM:} \qquad E_x \neq 0, E_y = 0 \tag{A.15}$$

In the simplest case, the system consists of two materials ($n_1,\ n_2$) in a sandwich structure with the material with the higher refractive index n_2 in the middle, the core region of the waveguide.

TE - Transverse Electric Modes

The transverse electric mode (TE) has an electric field component in $\hat{y}$ only.

$$\mathbf{E} = \begin{pmatrix} 0 \\ E_y \\ 0 \end{pmatrix} \qquad \mathbf{H} = \begin{pmatrix} H_x \\ 0 \\ H_z \end{pmatrix} \tag{A.16}$$

The following equation defines the TE-Modes:

$$\frac{\mathrm{d}^2 E_y(x)}{\mathrm{d}x^2} + n(x)^2 k_z^2 E_y(x) = n_{\text{eff}}^2 k_z^2 E_y(x) \tag{A.17}$$

Here, the formal equivalence to the time-independent Schrödinger equation can be pointed out. [1] For simplicity, the fundamental length unit can be chosen in units of the vacuum wavelength λ. With this choice the wave vector k_z is turned into 2π:

$$\frac{\mathrm{d}^2 E_y(x)}{\mathrm{d}x^2} = -4\pi^2 \left(n_i^2 - n_{\text{eff}}^2\right) E_y(x) \tag{A.18}$$

An electro-magnetic wave, traveling along $\hat{z}$ in our structure, spans over both materials. As the effective refractive index is directly related to the propagation constant, each mode has a specific effective refractive index. Its value has to lie in between the refractive indices of both materials.

$$n_1 < n_{\text{eff}} < n_2 \tag{A.19}$$

Equation (A.18) can be solved separately for all three areas i (above the core, in the core and below the core):

$$E_{y,i}(x) = \mathcal{E}_{y,i} \exp\left[-2\pi\imath\sqrt{n_i^2 - n_{\text{eff}}^2}\, x\right] \tag{A.20}$$

Here, $\mathcal{E}_y$ is the complex electric field amplitude. From the relation (A.19) it can be derived that $\sqrt{n_1^2 - n_{\text{eff}}^2}$ is imaginary and $\sqrt{n_2^2 - n_{\text{eff}}^2}$ is real. Consequently, inside the waveguide the exponent in (A.20) is imaginary, causing harmonic oscillations of $E_{y,2}$. In contrast, outside of the waveguide the electric field decays exponentially with x as there the exponent of equation (A.20) is real.

From the integral form of Maxwell's equations, it can be easily derived that the parallel and perpendicular electric and magnetic fields components fulfill certain continuity relations at dielectric interfaces (see standard optics textbooks like [30]):

$$\text{continuous:} \qquad D_\perp \; E_\parallel \; B_\perp \; H_\parallel \tag{A.21}$$

$$\text{discontinuous:} \qquad E_\perp \; D_\parallel \; H_\perp \; B_\parallel \tag{A.22}$$

In the case of the one-dimensionally confined waveguide, the two interfaces are spanned in the $(\hat{y}, \hat{z})$-plane and the electric field has a $\hat{y}$-component only. Therefore, the electric field is continuous at both interfaces. Let the interfaces be located at $x = -a$ and $x = a$ then the continuity conditions can be expressed as:

$$E_{y,1}(a) = E_{y,2}(a) \qquad E_{y,1}(-a) = E_{y,2}(-a) \tag{A.23}$$

$$\Rightarrow \qquad \mathcal{E}_{y,1} \exp\left[-2\pi\sqrt{n_{\text{eff}}^2 - n_1^2}\,(\pm a)\right] = \mathcal{E}_{y,2} \exp\left[-2\pi\imath\sqrt{n_2^2 - n_{\text{eff}}^2}\,(\pm a)\right] \tag{A.24}$$

[1] The complex wave-function corresponds to $E_y(x)$ and $\omega^2 c^2 n(x)^2$ resembles the position-dependent potential $V(x)$ for the quantum-mechanical one-dimensional potential well. The well-known solutions for the finite potential well in quantum mechanics also apply in this case. Now, if the refractive index of the inner material n_2 is higher than n_1 the result is a partially reflecting wall, whereas if $n_2 < n_1$ there exist two classes of states, bound states and unbound states corresponding to guided and non-guided modes.

Then, the electric field in the tree regions can be expressed as:

$$E_y(x) = \begin{cases} \mathcal{E}_{y,1} \exp\left[2\pi\sqrt{n_{\text{eff}}^2 - n_1^2}\,(x+a)\right] & \text{for } x < -a \\ \mathcal{E}_{y,2} \cos\left[2\pi\sqrt{n_2^2 - n_{\text{eff}}^2}\,x + \gamma\right] & \text{for } |x| < a \\ \mathcal{E}_{y,1} \exp\left[2\pi\sqrt{n_{\text{eff}}^2 - n_1^2}\,(a-x)\right] & \text{for } x > a \end{cases} \tag{A.25}$$

The phase factor γ, introduced in the second equation, takes care of even and odd modes (symmetric and antisymmetric) and is $\pi/2$ for even modes, but 0 for odd modes. Plugging the expression for $E_{y,i}(x)$ into the first of the Maxwell's equations (formulas (A.1a) to (A.1d)) gives:

$$H_x(x) = -\frac{2\pi n_{\text{eff}}}{\omega\mu_0} E_y(x) \tag{A.26a}$$

$$H_y(x) = 0 \tag{A.26b}$$

$$H_z(x) = -\frac{1}{\imath\omega\mu_0}\frac{\partial E_y(x)}{\partial x} \tag{A.26c}$$

The third equation (A.26c) can be written as:

$$H_z(x) = -\frac{2\pi\imath}{\omega\mu_0} \begin{cases} -\sqrt{n_{\text{eff}}^2 - n_1^2}\,\mathcal{E}_{y,1} \exp\left[2\pi\sqrt{n_{\text{eff}}^2 - n_1^2}\,(x+a)\right] & \text{for} \quad x < -a \\ \sqrt{n_2^2 - n_{\text{eff}}^2}\,\mathcal{E}_{y,2} \sin\left[2\pi\sqrt{n_2^2 - n_{\text{eff}}^2}\,x + \gamma\right] & \text{for} \quad |x| < a \\ \sqrt{n_{\text{eff}}^2 - n_1^2}\,\mathcal{E}_{y,1} \exp\left[2\pi\sqrt{n_{\text{eff}}^2 - n_1^2}\,(a-x)\right] & \text{for} \quad x > a \end{cases} \tag{A.27}$$

Applying the continuity condition (formulas (A.21) and (A.22)) yields:

$$\mathcal{E}_{y,1} = \mathcal{E}_{y,2} \cos\left[\gamma - 2\pi\sqrt{n_2^2 - n_{\text{eff}}^2}\,a\right] \tag{A.28}$$

Using the continuity of the magnetic field $H_{z,1}(-a) = H_{z,2}(-a)$ in (A.27) provides:

$$-\sqrt{n_{\text{eff}}^2 - n_1^2}\,\mathcal{E}_{y,1} = \sqrt{n_2^2 - n_{\text{eff}}^2}\,\mathcal{E}_{y,2} \sin\left[\gamma - 2\pi\sqrt{n_2^2 - n_{\text{eff}}^2}\,a\right] \tag{A.29}$$

The continuity of $H_z(x)$ (provided μ_r is constant everywhere) is equivalent to the fact that the first derivative of the electric field $\partial E_y/\partial x$ is continuous. The same procedure for $x = a$ results in:

$$\mathcal{E}_{y,1} = \mathcal{E}_{y,2} \cos\left[2\pi\sqrt{n_2^2 - n_{\text{eff}}^2}\,a + \gamma\right] \tag{A.30}$$

$$\sqrt{n_{\text{eff}}^2 - n_1^2}\,\mathcal{E}_{y,1} = \sqrt{n_2^2 - n_{\text{eff}}^2}\,\mathcal{E}_{y,2} \sin\left[2\pi\sqrt{n_2^2 - n_{\text{eff}}^2}\,a + \gamma\right] \tag{A.31}$$

By dividing equation (A.29) by (A.28) and equation (A.31) by (A.28), it follows:

$$-\sqrt{\frac{n_{\text{eff}}^2 - n_1^2}{n_2^2 - n_{\text{eff}}^2}} = \tan\left[\gamma - 2\pi\sqrt{n_2^2 - n_{\text{eff}}^2}\,a\right] \tag{A.32}$$

$$\sqrt{\frac{n_{\text{eff}}^2 - n_1^2}{n_2^2 - n_{\text{eff}}^2}} = \tan\left[\pi\sqrt{n_2^2 - n_{\text{eff}}^2}\,a + \gamma\right] \tag{A.33}$$

γ can be eliminated combining both equations. Doing so, it has to be noted that the inverse function of the tangent, the arctangent is periodic in whole multiples q of π:

$$-\arctan\left[\sqrt{\frac{n_{\text{eff}}^2 - n_1^2}{n_2^2 - n_{\text{eff}}^2}}\right] + q_1\pi = \gamma - 2\pi\sqrt{n_2^2 - n_{\text{eff}}^2}\,a \tag{A.34}$$

$$\arctan\left[\sqrt{\frac{n_{\text{eff}}^2 - n_1^2}{n_2^2 - n_{\text{eff}}^2}}\right] + q_2\pi = 2\pi\sqrt{n_2^2 - n_{\text{eff}}^2}\,a + \gamma \tag{A.35}$$

Subtracting equation (A.35) from (A.34), provides:

$$\frac{2}{\pi}\arctan\left[\sqrt{\frac{n_{\text{eff}}^2 - n_1^2}{n_2^2 - n_{\text{eff}}^2}}\right] - (q_1 - q_2) = 4\sqrt{n_2^2 - n_{\text{eff}}^2}\,a \tag{A.36}$$

The difference between two integers is again an integer, therefore, $q_1 - q_2 =: -q$, yielding:

$$\frac{2}{\pi}\arctan\left[\sqrt{\frac{n_{\text{eff}}^2 - n_1^2}{n_2^2 - n_{\text{eff}}^2}}\right] + q = 4\sqrt{n_2^2 - n_{\text{eff}}^2}\,a \tag{A.37}$$

or:

$$q = 4a\sqrt{n_2^2 - n_{\text{eff}}^2} - \frac{2}{\pi}\arctan\left[\sqrt{\frac{n_{\text{eff}}^2 - n_1^2}{n_2^2 - n_{\text{eff}}^2}}\right] \tag{A.38}$$

This function can be evaluated graphically by plotting q as function of the effective refractive index and for different waveguide widths $(2a)$ (see figure A.1). Solutions of the equation exist for all values, for which the function graph crosses with an integer number of q (indicated by black circles in figure A.1). For every waveguide width $(2a)$, at least the fundamental mode $q = 0$ exists. In a certain parameter range ($(2a) < 1/(2\sqrt{n_2^2 - n_1^2})$), only one single guided mode exists whereas for the rest multiple modes are possible.

In order to plot the mode profiles (A.25) for selected dimensions, the spatial phase offset γ has to be discussed in more detail. Equations (A.28) and (A.30) define that γ can only take integer multiples of $\pi/2$. Without loss of generality, γ is either 0 or $\pi/2$. Then, the expression for $E_y(x)$ (A.25) results either in an antinode or zero-crossing at the symmetry plane $x = 0$:

$$E_y(x=0) = \begin{cases} \mathcal{E}_{y,2} & \text{(full amplitude)} \quad \text{for } \gamma = 0 \\ 0 & \text{(zero-crossing)} \quad \text{for } \gamma = \frac{\pi}{2} \end{cases} \tag{A.39}$$

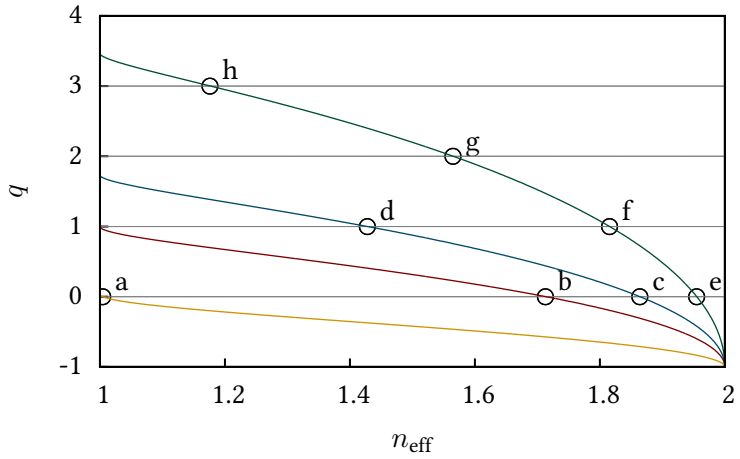

Figure A.1.: The value q (equation (A.38)) plotted against the effective refractive index for different waveguide widths: $2a = 0.01,\ 0.288,\ 0.5,\ 1$, and 2. For each crossing of a curve with a whole number of q a TE-mode exists. These points where the conditions for a mode is fulfilled are marked with a circle and a letter (the letters are used to reference the intersections with the plotted mode profiles in figure A.2) . The refractive indices are chosen $n_1 = 1$, $n_2 = 2$.

Comparing equations (A.34) and (A.35) then yields:

$$\gamma = \frac{\pi}{2}(q_1 + q_2)$$

Combined with $q_2 - q_1 = q$ and the fact that q, q_1 and q_2 are integers, it can be derived, that for even (odd) q, the phase factor gamma can be chosen as 0 ($\pi/2$). Conclusively, the modes with even q show an amplitude maximum (antinode) at the waveguide center and are called even modes. Accordingly, the modes with odd q have a zero-crossing at the waveguide center and are called odd modes. The fundamental mode is always an even mode and higher modes alternate between odd and even modes. Exemplary mode profiles for different waveguide widths are shown in figure A.2. Here, the mode profiles are denoted equally to the solutions of equation (A.38) in figure A.1.

This mode is referred to as transverse electric mode (TE) as the electric field has a transverse component only. In contrast, the magnetic field features a transverse and a longitudinal component $H_x(x)$ and $H_z(x)$ (plotted in figure A.3).

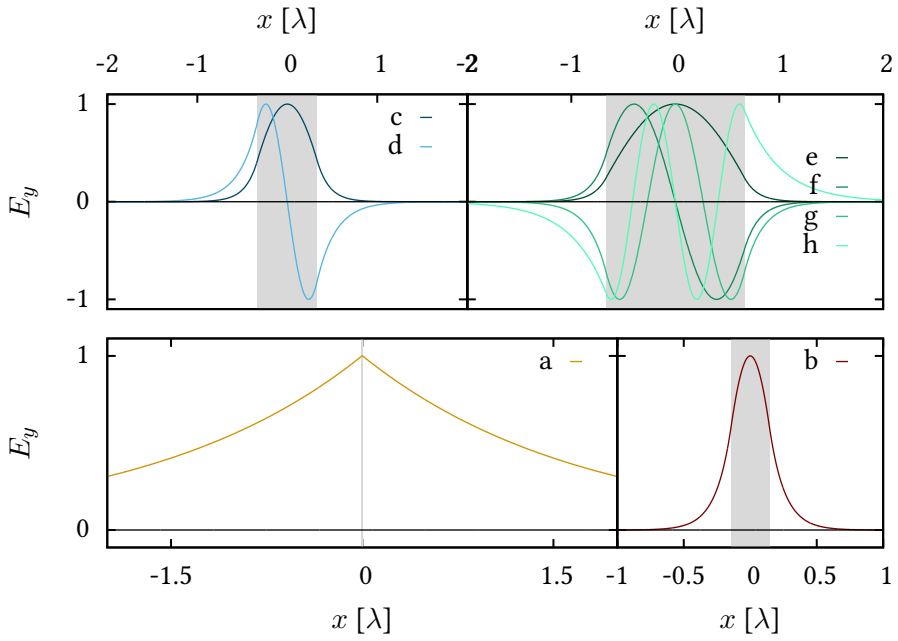

Figure A.2.: TE-mode profiles for $E_y(x)$ are plotted based on equation (A.25), using the graphical solutions from equation (A.38) presented in graph A.1. The identifiers are set accordingly to figure A.1.

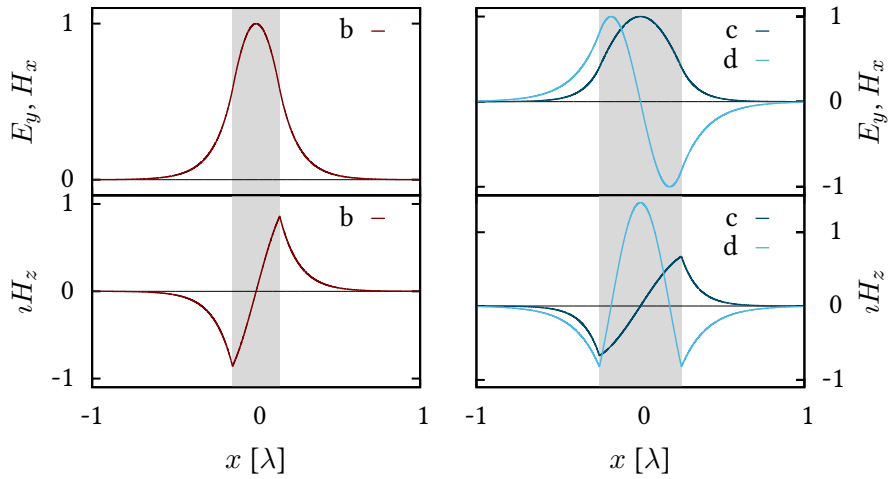

Figure A.3.: Profiles of the magnetizing fields $E_x(x)$, $H_x(x)$ and $H_z(x)$ for a subset of the TE-modes presented in figure A.2. The profiles are found as solutions to equations (A.25), (A.26a) and (A.27), respectively.

TM - Transverse Magnetic Modes

The transverse-magnetic modes have an electric field polarized in $\hat{x}$ meaning:

$$\mathbf{E} = \begin{pmatrix} E_x \\ 0 \\ E_z \end{pmatrix} \qquad \mathbf{H} = \begin{pmatrix} 0 \\ H_y \\ 0 \end{pmatrix} \tag{A.40}$$

As before, the fundamental length unit chosen the vacuum wavelength λ, and therefore, $k_z = 2\pi$: With the use of $\mathbf{H} = H_y$ and $\mathbf{H}$ being independent of y, equation (A.11b) for the magnetic field component transforms into:

$$\frac{\mathrm{d}^2 H_y}{\mathrm{d}x^2} + (2\pi)^2 \left(n^2(x,y) - n_{\text{eff}}^2\right) H_y = 0 \tag{A.41}$$

Analogous to the discussion of the TE-modes, this equation can be solved by:

$$H_y(x) = \begin{cases} \mathcal{H}_{y,1} \exp\left[2\pi\sqrt{n_{\text{eff}}^2 - n_1^2}\,(x+a)\right] & \text{for } x < -a \\ \mathcal{H}_{y,2} \cos\left[2\pi\sqrt{n_2^2 - n_{\text{eff}}^2}\,x + \gamma\right] & \text{for } |x| < a \\ \mathcal{H}_{y,1} \exp\left[-2\pi\sqrt{n_{\text{eff}}^2 - n_1^2}\,(x-a)\right] & \text{for } x > a \end{cases} \tag{A.42}$$

However, in contrast to the discussion of the TE-modes, the spatially varying refractive index enters, with $\varepsilon(\mathbf{r}) = \varepsilon(x)$ the electric field components:

$$E_x(x) = -\frac{2\pi n_{\text{eff}}}{\omega\varepsilon(x)} H_y(x) \tag{A.43}$$

$$E_y(x) = 0 \tag{A.44}$$

$$E_z(x) = \frac{1}{\imath\omega\varepsilon(x)} \frac{\partial H_y(x)}{\partial x} \tag{A.45}$$

The third equation (A.45) gives for the three regions i with the dielectric permittivity ε_i:

$$E_z(x) = \begin{cases} \frac{\sqrt{n_{\text{eff}}^2 - n_1^2}}{\imath\omega\varepsilon_1} \mathcal{H}_{y,1} \exp\left[2\pi\sqrt{n_{\text{eff}}^2 - n_1^2}\,(x+a)\right] & \text{for} \quad x < -a \\ -\frac{\sqrt{n_2^2 - n_{\text{eff}}^2}}{\imath\omega\varepsilon_2} \mathcal{H}_{y,2} \sin\left[2\pi\sqrt{n_2^2 - n_{\text{eff}}^2}\,x + \gamma\right] & \text{for} \quad |x| < a \\ -\frac{\sqrt{n_{\text{eff}}^2 - n_1^2}}{\imath\omega\varepsilon_1} \mathcal{H}_{y,1} \exp\left[-2\pi\sqrt{n_{\text{eff}}^2 - n_1^2}\,(x-a)\right] & \text{for} \quad x > a \end{cases} \tag{A.46}$$

With the continuity conditions (A.21) and (A.22) applied, yielding $H_{y,1}(-a) = H_{y,2}(-a)$, the first expression ($x < -a$) of $H_y(x)$ (A.42) results in:

$$\mathcal{H}_{y,1} = \mathcal{H}_{y,2} \cos\left[\gamma - 2\pi\sqrt{n_2^2 - n_{\text{eff}}^2}\,a\right] \tag{A.47}$$

The continuity at $x = -a$ of the electric field component in propagation direction $E_{z,1}(-a) = E_{z,2}(-a)$ gives:

$$-\frac{\sqrt{n_{\text{eff}}^2 - n_1^2}}{\varepsilon_1}\,\mathcal{H}_{y,1} = \frac{\sqrt{n_2^2 - n_{\text{eff}}^2}}{\varepsilon_2}\,\mathcal{H}_{y,2}\sin\left[\gamma - 2\pi\sqrt{n_2^2 - n_{\text{eff}}^2}\,a\right] \tag{A.48}$$

The same procedure for $x = a$ renders:

$$\mathcal{H}_{y,1} = \mathcal{H}_{y,2}\cos\left[2\pi\sqrt{n_2^2 - n_{\text{eff}}^2}\,a + \gamma\right] \tag{A.49}$$

$$\frac{\sqrt{n_{\text{eff}}^2 - n_1^2}}{\varepsilon_1}\,\mathcal{H}_{y,1} = \frac{\sqrt{n_2^2 - n_{\text{eff}}^2}}{\varepsilon_2}\,\mathcal{H}_{y,2}\sin\left[2\pi\sqrt{n_2^2 - n_{\text{eff}}^2}\,a + \gamma\right] \tag{A.50}$$

By dividing equation (A.48) by (A.47) and equation (A.50) by (A.49) and by using the relation $n_i = \varepsilon_i^2$, we get:

$$-\sqrt{\frac{n_2}{n_1}\frac{n_{\text{eff}}^2 - n_1^2}{n_2^2 - n_{\text{eff}}^2}} = \tan\left[\gamma - 2\pi\sqrt{n_2^2 - n_{\text{eff}}^2}\,a\right] \tag{A.51}$$

$$\sqrt{\frac{n_2}{n_1}\frac{n_{\text{eff}}^2 - n_1^2}{n_2^2 - n_{\text{eff}}^2}} = \tan\left[2\pi\sqrt{n_2^2 - n_{\text{eff}}^2}\,a + \gamma\right] \tag{A.52}$$

Analogous to the procedure with the TE-modes, γ can be eliminated combining both equations. Therefore, it has to be noted that the inverse function of tan is periodic in whole multiples q of π.

$$-\arctan\left[\sqrt{\frac{n_2}{n_1}\frac{n_{\text{eff}}^2 - n_1^2}{n_2^2 - n_{\text{eff}}^2}}\right] + q_1\pi = \gamma - 2\pi\sqrt{n_2^2 - n_{\text{eff}}^2}\,a \tag{A.53}$$

$$\arctan\left[\sqrt{\frac{n_2}{n_1}\frac{n_{\text{eff}}^2 - n_1^2}{n_2^2 - n_{\text{eff}}^2}}\right] + q_2\pi = 2\pi\sqrt{n_2^2 - n_{\text{eff}}^2}\,a + \gamma \tag{A.54}$$

By substracting equation (A.53) from (A.54) one gets:

$$\frac{2}{\pi}\arctan\left[\sqrt{\frac{n_2}{n_1}\frac{n_{\text{eff}}^2 - n_1^2}{n_2^2 - n_{\text{eff}}^2}}\right] - (q_1 - q_2) = 4\sqrt{n_2^2 - n_{\text{eff}}^2}\,a \tag{A.55}$$

The difference between two integers is again an integer, therefore, $q_1 - q_2 = -q$, yielding:

$$\frac{2}{\pi}\arctan\left[\sqrt{\frac{n_2}{n_1}\frac{n_{\text{eff}}^2 - n_1^2}{n_2^2 - n_{\text{eff}}^2}}\right] + q = 4\sqrt{n_2^2 - n_{\text{eff}}^2}\,a \tag{A.56}$$

or:

$$q = 4a\sqrt{n_2^2 - n_{\text{eff}}^2} - \frac{2}{\pi}\arctan\left[\sqrt{\frac{n_2}{n_1}\frac{n_{\text{eff}}^2 - n_1^2}{n_2^2 - n_{\text{eff}}^2}}\right] \tag{A.57}$$

Fully analogous to the treatment of the TE-modes, can be evaluated graphically by plotting q as function of the effective refractive index and again for the same waveguide widths $(2a)$.

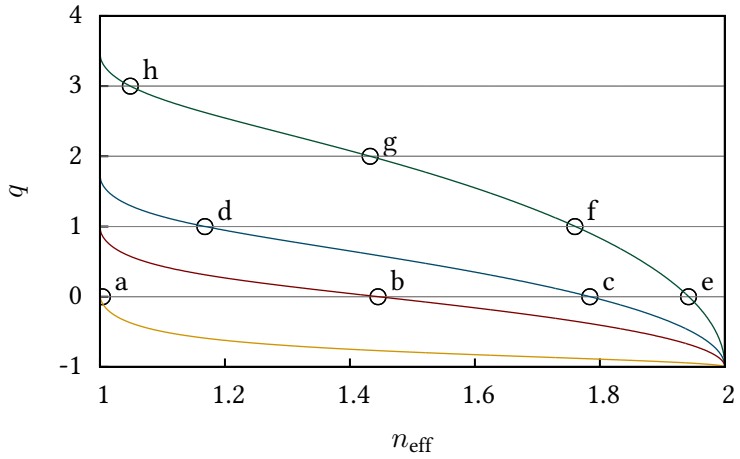

Figure A.4.: q plotted as function of the refractive index n_{eff} with equal parameters to figure A.1, but for TM-modes. Each crossing of a function graph with an integer value of q fulfills the condition for an allowed mode. Such crossings are indicated by a black circle and labeled with a letter.

The mode profiles of $H_y(x)$ are plotted in figure A.5. In contrast to the $E_y(x)$-profiles of the TE-modes, $H_y(x)$ of the TM-modes shows kinks at the dielectric interface. Furthermore, as shown in figure A.6, the electric field component E_x can feature a strong jump at the interface. Due to this jump, the electric field strength of the evanescent field is able to exceed the electric field strength inside the core region. This jump in the electric field is used to achieve high evanescent coupling with the tapered optical fibers (TOF) (see sections 2.3.2 and 4). However, such electric field jump limited to transverse magnetic modes or hybrid modes featuring a strong TM-part.

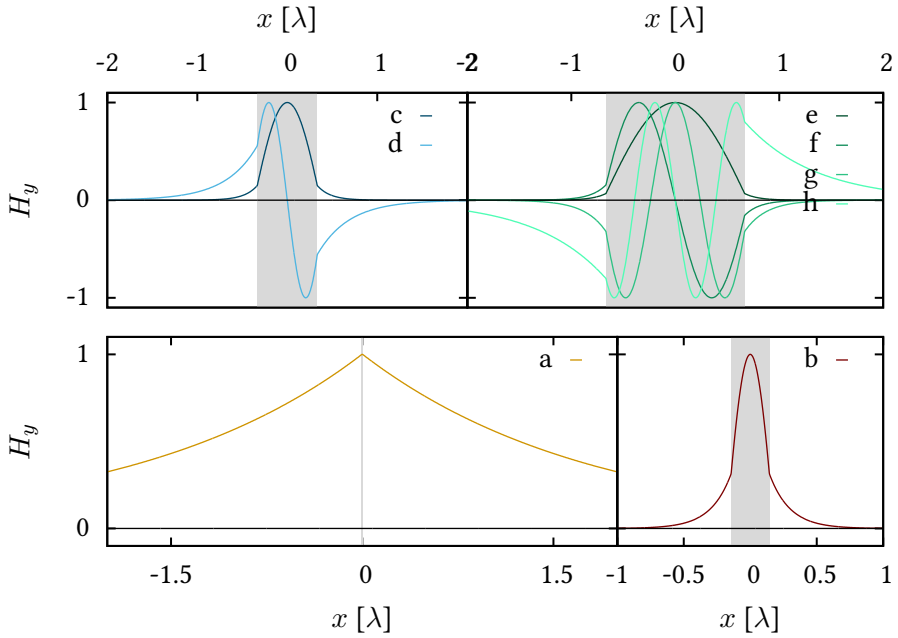

Figure A.5.: TM-mode profiles of the H_y-component of four exemplary waveguides determined as solutions for equation (A.42). The plotted profiles use the solutions of equation (A.57) as plotted in figure A.4.

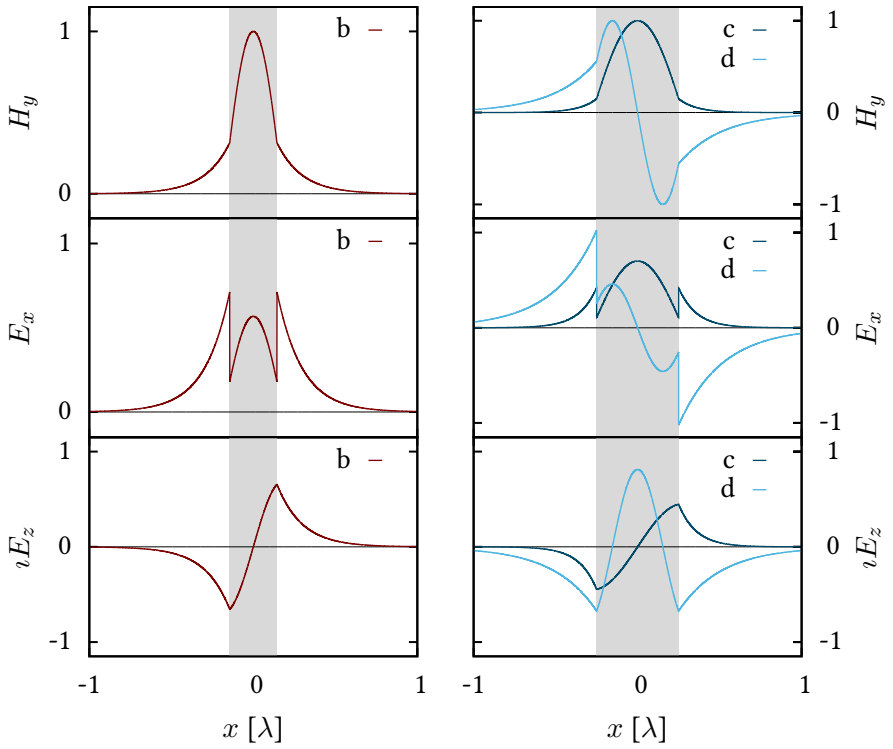

Figure A.6.: Profiles of the components H_y, E_x and E_z of two of the waveguide widths discussed in figure A.5. These profiles are based on equations (A.42), (A.43) and (A.46), respectively.

B. Experimental Setup

This chapter provides technical details on the experimental setup, which is designed for the characterization and preselection of diamond nanocrystals, the assembly of the coupled system of tapered optical fiber and diamond nanocrystal, and the analysis of the coupled system. The hybrid microscope, assembled as part of this thesis, is shortly described in the first section. The second section of this chapter discusses the basic functionality of the atomic force microscope and its capabilities to map surface topography on the nanometer scale.

Hybrid Microscope

The hybrid microscope, a combination of confocal scanning microscope and atomic force microscope, is presented in figure B.1. The excitation laser light at $532\,\mathrm{nm}$ is indicated by green arrows. It is guided to the confocal microscope via a polarization-maintaining fiber (PM) and coupled to free-space via a collimation optics. The excitation laser light is intensity-controlled and its polarization is rotated by a set of polarizers, liquid crystal retarders (LCR) and a quarter-wave plate ($\lambda/4$). Via a scanning voice coil mirror (VCM) and a 4f-telescope the excitation laser is guided into the microscope objective which focuses the excitation onto the sample. The fluorescence signal (red arrows) is collected via the same objective, transmitted by the dichroic mirror, cleaned with a low-pass filter at $590\,\mathrm{nm}$ (OG590) and a notchfilter at $532\,\mathrm{nm}$ and coupled into a SM600 optical fiber. Above the sample stage, the atomic force microscope (AFM) is situated. With this AFM, recording the sample's surface topology as well as the nanomanipulation of diamond nanocrystals can be performed, while the process can be monitored confocally. When a diamond nanocrystal has been placed on the tapered optical fiber (TOF), its fluorescence signal is partially channeled into the TOF. The signal in both arms of the TOF is cleaned with a low-pass filter at $590\,\mathrm{nm}$ (OG590) and a notch-filter at $532\,\mathrm{nm}$ and coupled into a SM600 optical fiber. All fibers guiding fluorescence signal can either be connected directly to an avalanche photo diode (APD), a Hanbury-Brown and Twiss-interferometer (a beamsplitter, two APDs, a time-to-digital converter (TDC) and a histogramming software) or a spectrometer. In the home-build spectrometer, the light guided by the input-fiber is collimated on to a diffraction grating. The refracted light is the imaged with a lens on to a CCD-camera (Andor iDus401A-BV), yielding a spectral resolution of $0.7\,\mathrm{nm}$.

Atomic Force Microscope

The atomic force microscope (AFM) is widely used in science to image topology but also to manipulate particles on the nanometer scale. The AFM has been discussed widely in the literature, however, a short introduction into its working principle is presented here.

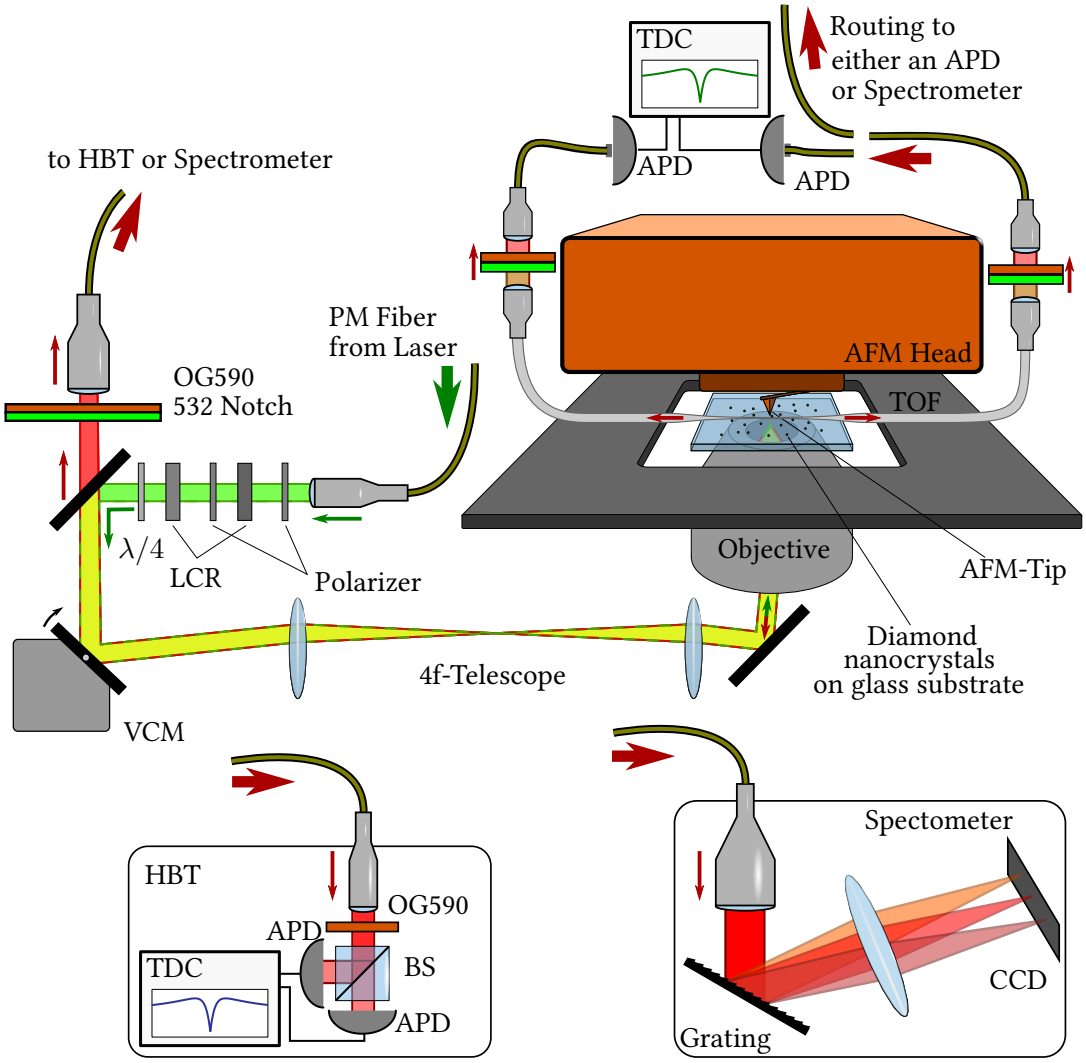

Figure B.1.: Schematic of the hybrid microscope including the AFM, the confocal microscope, the Hanbury-Brown and Twiss-interferometer (HBT) and the spectrometer.

The atomic force microscope uses the interaction of a sharp probe-tip with a specimen to gain informations about its local topology. There are several different operation modes and also modifications. The focus lies on the topological imaging of a surface using the intermittent contact mode or tapping mode in constant height mode. The probing tip is fixed below a cantilever, which acts as a spring. The cantilever is excited to vibrations perpendicular to the sample surface. The vibrational frequency is close to the resonance but not on resonance, therefore, a change in the damping will lead to a change in amplitude. When the tip is scanned across the samples surface, the topology of the surface will result in variation of the damping of the cantilevers vibration. The resulting variations in the vibrational amplitude can now be fed as error-signal into a feedback PID-controller, which moves the cantilever up and down to keep the amplitude of the vibration constant. There are two signals which can be recorded, the error-signal which is fed into the PID-controller as well as the PID's output signal. The error-signal contains information about the position of the edges, whereas the output of the PID is the absolute height information. It has to be noted that the forces between the probe and sample highly depend on the material of the topmost layer on the surface. A change in substrate material can produce a signal which can be misinterpreted as height change. For instance, measuring the height of a step of two different surface materials can be fault-prone. The probe-tip or AFM-tip is sharp but not infinitely pointy. Its own shape is always imprinted onto the structure, similar to a convolution. For once, this effect makes it impossible to resolve structures smaller than the tip but also a certain topological structure on the tip will be mixed with the structure of the sample.

On the technical side, here, as in most realizations, the vibrational amplitude is measured via the reflection of a laser at the cantilever onto a quadrant diode. In the standard configuration, a visible red laser diode is used for this purpose as it makes the alignment of the laser onto the cantilever untroublesome. However, such a wavelength will partially be collected via the confocal microscope and by far outshine the signal of the NV-centers. As this would make it impossible to operate the AFM at the same time as the confocal microscope, the hybrid nature of this setup would be obsolete. To circumvent this problem a laser diode with a wavelength of above 850nm has been chosen as replacement, which can be filtered out easily. Additionally, a long-pass filter is placed inside of the AFM to cut-off the non-lasing LED luminescence. The cantilever itself is excited with a piezo-element. The AFM used for the experiments presented here is using a flexure-based scanner which is driven with voice coils. This technique is claimed to be highly linear even without closed-loop stabilization and therefore, a cost-efficient alternative.

The pick-up of a diamond nanocrystals with the AFM-tip (see section 4) is mediated by surface van der Waals forces acting between close surfaces. When pushing the AFM-tip onto the diamond, there is a certain probability that the van der Waals force of the diamond to the tip exceeds the force to the surface. In this case, removing the tip will also remove the diamond nanocrystal. The diamond is then strongly sticking to the tip compared to gravitation and air flow. By pushing the tip again onto a surface, the diamond can be released from the tip and sticks to the surface. Here again, the force to the surface has to be stronger than to the tip. Such surface forces are very sensitive to environmental conditions. It has been reported, that a high humidity is needed to allow successful pick-up. This was ensured by placing a water evaporator close to the setup. Within this work, a prior cleaning step of the AFM-tips in oxygen

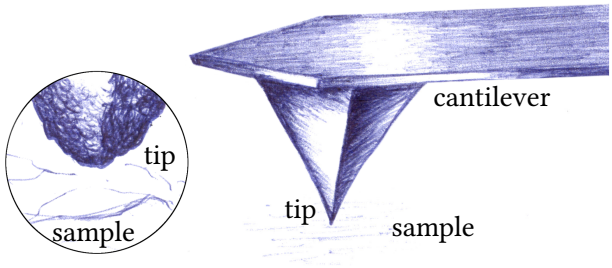

Figure B.2.: Illustrations of a typical probe-tip of an atomic force microscope. AFM-tip attached to the cantilever (right) and a closeup on the tip (left). Typical tip radii are of the order of a few nanometers, the tips used in this experiment have a tip radius of about 50nm.

plasma has been inevitable. Flattening of the tip prior to the pick-up can enhance the pick-up probability further. Including all these measures, most diamond nanocrystals could be picked up successfully, however, about one third could be placed again after several tenths of tries. The other two thirds might have shown stronger sticking to the tip then to the sample surface, sticked to the side of the tip or where lost during the process.

Bibliography

[1] M. V. Gurudev Dutt, L. Childress, L. Jiang, E. Togan, J. Maze, F. Jelezko, A. S. Zibrov, P. R. Hemmer, and M. D. Lukin. Quantum Register Based on Individual Electronic and Nuclear Spin Qubits in Diamond. *Science*, 316(5829):1312–1316, 2007.

[2] Peter Christian Maurer, Georg Kucsko, Christian Latta, Liang Jiang, Norman Ying Yao, Steven D Bennett, Fernando Pastawski, David Hunger, Nicholas Chisholm, Matthew Markham, et al. Room-temperature quantum bit memory exceeding one second. *Science*, 336(6086):1283–1286, 2012.

[3] Edward Mills Purcell. Spontaneous Emission Probabilities at Radio Frequencies. *Phys. Rev.*, 69:674–674, 1946.

[4] Daniel Kleppner. Inhibited spontaneous emission. *Physical Review Letters*, 47(4):233, 1981.

[5] Knill E., Laflamme R., and Milburn G. J. A scheme for efficient quantum computation with linear optics. *Nature*, 409(6816):46–52, 2001.

[6] Pieter Kok, W. J. Munro, Kae Nemoto, T. C. Ralph, Jonathan P. Dowling, and G. J. Milburn. Linear optical quantum computing with photonic qubits. *Rev. Mod. Phys.*, 79:135–174, 2007.

[7] Thomas Jennewein, Marco Barbieri, and Andrew G. White. Single-photon device requirements for operating linear optics quantum computing outside the post-selection basis. *Journal of Modern Optics*, 58(3-4):276–287, 2011.

[8] M. Pototschnig, Y. Chassagneux, J. Hwang, G. Zumofen, A. Renn, and V. Sandoghdar. Controlling the Phase of a Light Beam with a Single Molecule. *Phys. Rev. Lett.*, 107:063001, 2011.

[9] T. G. Tiecke, Jeffrey Douglas Thompson, Nathalie Pulmones de Leon, L. R. Liu, V. Vuletić, and Mikhail D. Lukin. Nanophotonic quantum phase switch with a single atom. *Nature*, 508(7495):241–244, 2014.

[10] Eden Rephaeli, Jung-Tsung Shen, and Shanhui Fan. Full inversion of a two-level atom with a single-photon pulse in one-dimensional geometries. *Phys. Rev. A*, 82:033804, 2010.

[11] Darrick E. Chang, Anders S. Sørensen, Eugene A. Demler, and Mikhail D. Lukin. A single-photon transistor using nanoscale surface plasmons. *Nature Physics*, 3(11):807–812, 2007.

[12] Jaesuk Hwang, Martin Pototschnig, Robert Lettow, Gert Zumofen, Alois Renn, Stephan Götzinger, and Vahid Sandoghdar. A single-molecule optical transistor. *Nature*, 460(7251):76–80, 2009.

[13] Philipp Neumann, Ingmar Jakobi, Florian Dolde, Christian Burk, Rolf Reuter, Gerald Waldherr, Jan Honert, Thomas Wolf, Andreas Brunner, Jeong Hyun Shim, et al. High-precision nanoscale temperature sensing using single defects in diamond. *Nano letters*, 13(6):2738–2742, 2013.

[14] M. W. Doherty, F. Dolde, H. Fedder, F. Jelezko, J. Wrachtrup, N. B. Manson, and L. C. L. Hollenberg. Theory of the ground-state spin of the NV- center in diamond. *Physical Review B*, 85(20):205203, 2012.

[15] Maze J. R., Stanwix P. L., Hodges J. S., Hong S., Taylor J. M., Cappellaro P., Jiang L., Dutt M. V. Gurudev, Togan E., Zibrov A. S., Yacoby A., Walsworth R. L., and Lukin M. D. Nanoscale magnetic sensing with an individual electronic spin in diamond. *Nature*, 455(7213):644–647, 2008.

[16] Andreas W. Schell, Philip Engel, Julia F. M. Werra, Christian Wolff, Kurt Busch, and Oliver Benson. Scanning Single Quantum Emitter Fluorescence Lifetime Imaging: Quantitative Analysis of the Local Density of Photonic States. *Nano Letters*, 14(5):2623–2627, 2014.

[17] Ryan Beams, Dallas Smith, Timothy W. Johnson, Sang-Hyun Oh, Lukas Novotny, and A. Nick Vamivakas. Nanoscale fluorescence lifetime imaging of an optical antenna with a single diamond NV center. *Nano letters*, 13(8):3807–3811, 2013.

[18] Benedikt Schwarz, Peter Reininger, Daniela Ristanić, Hermann Detz, Aaron Maxwell Andrews, Werner Schrenk, and Gottfried Strasser. Monolithically integrated mid-infrared lab-on-a-chip using plasmonics and quantum cascade structures. *Nature communications*, 5:4085, 2014.

[19] Harold Craighead. Future lab-on-a-chip technologies for interrogating individual molecules. *Nature*, 442(7101):387–393, 2006.

[20] Ariane Stiebeiner, Ruth Garcia-Fernandez, and Arno Rauschenbeutel. Design and optimization of broadband tapered optical fibers with a nanofiber waist. *Opt. Express*, 18(22):22677–22685, 2010.

[21] Mark Fox. *Quantum Optics: An Introduction*, volume 6. 2006.

[22] Y.K. Wang and I.C. Khoo. On the Wigner-Weisskopf approximation in quantum optics . *Optics Communications*, 11(4):323–326, 1974.

[23] Lukas Novotny and Bert Hecht. *Principles of Nano-Optics*. 2006.

[24] M. O. Scully and S. Zubairy. *Quantum Optics*. 1997.

[25] Stephen M. Barnett, Bruno Huttner, and Rodney Loudon. Spontaneous emission in absorbing dielectric media. *Phys. Rev. Lett.*, 68:3698–3701, 1992.

[26] J. Hwang and E. A. Hinds. Dye molecules as single-photon sources and large optical nonlinearities on a chip. *New Journal of Physics*, 13(8):085009, 2011.

[27] Levi P. Neukirch, Jan Gieseler, Romain Quidant, Lukas Novotny, and A. Nick Vamivakas. Observation of nitrogen vacancy photoluminescence from an optically levitated nanodiamond. *Optics letters*, 38(16):2976–2979, 2013.

[28] Qimin Quan, Irfan Bulu, and Marko Loncar. Broadband waveguide QED system on a chip. *Phys. Rev. A*, 80:011810, 2009.

[29] Faraon Andrei, Barclay Paul E., Santori Charles, Fu Kai-Mei C., and Beausoleil Raymond G. Resonant enhancement of the zero-phonon emission from a colour centre in a diamond cavity. *Nat Photon*, 5(5):301–305, 2011.

[30] L. Bergmann and C. Schaefer. *Lehrbuch der Experimentalphysik*. Band 3. 2004.

[31] I. N. Bronstein, K. A. Semendjajew, G. Musiol, and H. Muehlig. *Taschenbuch der Mathematik, 5. Auflage*. Verlag Harri Deutsch, 2001.

[32] R. R. A. Syms and J. R. Cozens. *Optical Guided Waves and Devices*. 1992.

[33] Fam Le Kien, J.Q. Liang, K. Hakuta, and V.I. Balykin. Field intensity distributions and polarization orientations in a vacuum-clad subwavelength-diameter optical fiber. *Optics Communications*, 242(4–6):445–455, 2004.

[34] Ariane Stiebeiner. *Nanofiber-based spectroscopy of organic molecules*. PhD thesis, 2013.

[35] V. V. Klimov and M. Ducloy. Spontaneous emission rate of an excited atom placed near a nanofiber. *Phys. Rev. A*, 69(1):013812, 2004.

[36] F. Warken, E. Vetsch, D. Meschede, M. Sokolowski, and A. Rauschenbeutel. Ultrasensitive surface absorption spectroscopy using sub-wavelength diameter optical fibers. *Opt. Express*, 15(19):11952–11958, 2007.

[37] Ardavan F. Oskooi, David Roundy, Mihai Ibanescu, Peter Bermel, J. D. Joannopoulos, and Steven G. Johnson. MEEP: A flexible free-software package for electromagnetic simulations by the FDTD method. *Computer Physics Communications*, 181:687–702, 2010.

[38] Artem V. Boriskin, Svetlana V. Boriskina, Anthony Rolland, Ronan Sauleau, and Alexander I. Nosich. Test of the FDTD accuracy in the analysis of the scattering resonances associated with high-Q whispering-gallery modes of a circular cylinder. *JOSA A*, 25(5):1169–1173, 2008.

[39] Marcus W. Doherty, Neil B. Manson, Paul Delaney, Fedor Jelezko, Jörg Wrachtrup, and Lloyd C.L. Hollenberg. The nitrogen-vacancy colour centre in diamond . *Physics Reports*, 528(1):1–45, 2013.

[40] Christian Kurtsiefer, Sonja Mayer, Patrick Zarda, and Harald Weinfurter. Stable Solid-State Source of Single Photons. *Phys. Rev. Lett.*, 85(2):290–293, 2000.

[41] Quantum Communications Victoria, The University of Melbourne, School of Physics, QCV, Parkville VIC 3010, Australia.

[42] Dolde F., Fedder H., Doherty M. W., Nobauer T., Rempp F., Balasubramanian G., Wolf T., Reinhard F., Hollenberg L. C. L., Jelezko F., and Wrachtrup J. Electric-field sensing using single diamond spins. *Nat Phys*, 7(6):459–463, 2011.

[43] T. Staudacher, F. Shi, S. Pezzagna, J. Meijer, J. Du, C. A. Meriles, F. Reinhard, and J. Wrachtrup. Nuclear magnetic resonance spectroscopy on a (5-nanometer) 3 sample volume. *Science*, 339(6119):561–563, 2013.

[44] Patrick Maletinsky, Sungkun Hong, Michael Sean Grinolds, B. Hausmann, Mikhail D. Lukin, Ronald L. Walsworth, Marko Loncar, and Amir Yacoby. A robust scanning diamond sensor for nanoscale imaging with single nitrogen-vacancy centres. *Nature nanotechnology*, 7(5):320–324, 2012.

[45] Andreas W. Schell, Philip Engel, Julia F. M. Werra, Christian Wolff, Kurt Busch, and Oliver Benson. Scanning single quantum emitter fluorescence lifetime imaging: Quantitative analysis of the local density of photonic states. *Nano letters*, 14(5):2623–2627, 2014.

[46] A. Batalov, C. Zierl, T. Gaebel, P. Neumann, I-Y. Chan, G. Balasubramanian, P. R. Hemmer, F. Jelezko, and J. Wrachtrup. Temporal coherence of photons emitted by single nitrogen-vacancy defect centers in diamond using optical Rabi-oscillations. *Physical review letters*, 100(7):077401, 2008.

[47] P. Siyushev, H. Pinto, M. Vörös, A. Gali, F. Jelezko, and J. Wrachtrup. Optically Controlled Switching of the Charge State of a Single Nitrogen-Vacancy Center in Diamond at Cryogenic Temperatures. *Phys. Rev. Lett.*, 110:167402, 2013.

[48] K. Beha, A. Batalov, N. B. Manson, R. Bratschitsch, and A. Leitenstorfer. Optimum Photoluminescence Excitation and Recharging Cycle of Single Nitrogen-Vacancy Centers in Ultrapure Diamond. *Phys. Rev. Lett.*, 109:097404, 2012.

[49] N. Aslam, G. Waldherr, P. Neumann, F. Jelezko, and J. Wrachtrup. Photo-induced ionization dynamics of the nitrogen vacancy defect in diamond investigated by single-shot charge state detection. *New Journal of Physics*, 15(1):013064, 2013.

[50] C. Wang. *A Solid-State Single Photon Source Based on Color Centers in Diamond*. Promotion, Ludwig Maximilians Universität München, 2007.

[51] A. Gali, T. Simon, and J. E. Lowther. An ab initio study of local vibration modes of the nitrogen-vacancy center in diamond. *New Journal of Physics*, 13(2):025016, 2011.

[52] G. Davies and M. F. Hamer. Optical Studies of the 1.945 eV Vibronic Band in Diamond. *Proceedings of the Royal Society of London. Series A, Mathematical and Physical Sciences*, 348(1653):285–298, 1976.

[53] Anthony Mark Fox. *Optical properties of solids*, volume 3. 2001.

[54] Bradley R. Smith, David W. Inglis, Bjornar Sandnes, James R. Rabeau, Andrei V. Zvyagin, Daniel Gruber, Christopher J. Noble, Robert Vogel, Eiji Ōsawa, and Taras Plakhotnik. Five-Nanometer Diamond with Luminescent Nitrogen-Vacancy Defect Centers. *Small*, 5(14):1649–1653, 2009.

[55] Jean-Paul Boudou, Julia Tisler, Rolf Reuter, Alain Thorel, Patrick A Curmi, Fedor Jelezko, and Joerg Wrachtrup. Fluorescent nanodiamonds derived from HPHT with a size of less than 10nm. *Diamond and Related Materials*, 37:80–86, 2013.

[56] Igor I. Vlasov, Olga Shenderova, Stuart Turner, Oleg I. Lebedev, Artem A. Basov, Ilmo Sildos, Mickel Rähn, Andrey A. Shiryaev, and Gustaaf Van Tendeloo. Nitrogen and Luminescent Nitrogen-Vacancy Defects in Detonation Nanodiamond. *Small*, 6(5):687–694, 2010.

[57] Microdiamant AG, Kreuzlingerstrasse 1, CH-8574 Lengwil, Schweiz.

[58] L.M. Van Moppes & Sons SA, 55, av. de la Praille, CH-1211 Genf 26, Schweiz.

[59] Quantum Particles, c/o L.M. Van Moppes & Sons SA, CH-1211 Genf 26, Schweiz .

[60] Fabian Petersen. In-situ Nanomanipulation von einzelnen Diamant Nanokristallen und Kopplung an das evanszente Feld einer optischen Nanofaser. Master's thesis, Ludwig–Maximilians–Universität München, 2013.

[61] Bradac C., Gaebel T., Naidoo N., Sellars M. J., Twamley J., Brown L. J., Barnard A. S., Plakhotnik T., Zvyagin A. V., and Rabeau J. R. Observation and control of blinking nitrogen-vacancy centres in discrete nanodiamonds. *Nat Nano*, 5(5):345–349, 2010.

[62] M. V. Hauf, B. Grotz, B. Naydenov, M. Dankerl, S. Pezzagna, J. Meijer, F. Jelezko, J. Wrachtrup, M. Stutzmann, F. Reinhard, and J. A. Garrido. Chemical control of the charge state of nitrogen-vacancy centers in diamond. *Phys. Rev. B*, 83:081304, 2011.

[63] Aditi Datta, Mesut Kirca, Yao Fu, and Albert C To. Surface structure and properties of functionalized nanodiamonds: a first-principles study. *Nanotechnology*, 22(6):065706, 2011.

[64] René Hoffmann, Harald Obloh, Norio Tokuda, Nianjun Yang, and Christoph E. Nebel. Fractional Surface Termination of Diamond by Electrochemical Oxidation. *Langmuir*, 28(1):47–50, 2012.

[65] Hannes Schniepp and Vahid Sandoghdar. Spontaneous Emission of Europium Ions Embedded in Dielectric Nanospheres. *Phys. Rev. Lett.*, 89(25):257403, 2002.

[66] D. V. Kuznetsov, Vl. K. Roerich, and M. G. Gladush. Local field and radiative relaxation rate in a dielectric medium. *Journal of Experimental and Theoretical Physics*, 113(4):647–658, 2011.

[67] K. K. Pukhov, T. T. Basiev, and Yu. V. Orlovskii. Spontaneous emission in dielectric nanoparticles. *JETP Letters*, 88(1):12–18, 2009.

[68] Alexios Beveratos, Rosa Brouri, Thierry Gacoin, Jean-Philippe Poizat, and Philippe Grangier. Nonclassical radiation from diamond nanocrystals. *Phys. Rev. A*, 64:061802, 2001.

[69] Beveratos, A., Kühn, S., Brouri, R., Gacoin, T., Poizat, J.-P., and Grangier, P. Room temperature stable single-photon source. *Eur. Phys. J. D*, 18(2):191–196, 2002.

[70] Lars Liebermeister, Fabian Petersen, Asmus v Münchow, Daniel Burchardt, Juliane Hermelbracht, Toshiyuki Tashima, Andreas W Schell, Oliver Benson, Thomas Meinhardt, Anke Krueger, et al. Tapered fiber coupling of single photons emitted by a deterministically positioned single nitrogen vacancy center. *Applied Physics Letters*, 104(3):031101, 2014.

[71] Masazumi Fujiwara, Kiyota Toubaru, Tetsuya Noda, Hong-Quan Zhao, and Shigeki Takeuchi. Highly Efficient Coupling of Photons from Nanoemitters into Single-Mode Optical Fibers. *Nano Letters*, 11(10):4362–4365, 2011.

[72] Tim Schröder, Masazumi Fujiwara, Tetsuya Noda, Hong-Quan Zhao, Oliver Benson, and Shigeki Takeuchi. A nanodiamond-tapered fiber system with high single-mode coupling efficiency. *Opt. Express*, 20(10):10490–10497, 2012.

[73] Ramachandrarao Yalla, Fam Le Kien, M. Morinaga, and K. Hakuta. Efficient Channeling of Fluorescence Photons from Single Quantum Dots into Guided Modes of Optical Nanofiber. *Phys. Rev. Lett.*, 109:063602, 2012.

[74] Ramachandrarao Yalla, K. P. Nayak, and K. Hakuta. Fluorescence photon measurements from single quantum dots on an optical nanofiber. *Opt. Express*, 20(3):2932–2941, 2012.

[75] Ariane Stiebeiner, O. Rehband, R. Garcia-Fernandez, and A. Rauschenbeutel. Ultrasensitive fluorescence spectroscopy of isolated surface-adsorbed molecules using an optical nanofiber. *Optics express*, 17(24):21704–21711, 2009.

[76] K. P. Nayak, P. N. Melentiev, M. Morinaga, Fam Le Kien, V. I. Balykin, and K. Hakuta. Optical nanofiber as an efficient tool for manipulating and probing atomicFluorescence. *Opt. Express*, 15(9):5431–5438, 2007.

[77] E. Vetsch, D. Reitz, G. Sagué, R. Schmidt, S. T. Dawkins, and A. Rauschenbeutel. Optical Interface Created by Laser-Cooled Atoms Trapped in the Evanescent Field Surrounding an Optical Nanofiber. *Phys. Rev. Lett.*, 104(20):203603, 2010.

[78] F. Ciccarello, M. Paternostro, S. Bose, D. E. Browne, G. M. Palma, and M. Zarcone. Physical model for the generation of ideal resources in multipartite quantum networking. *Phys. Rev. A*, 82:030302, 2010.

[79] F. Warken. *Ultradünne Glasfasern als Werkzeug zur Kopplung von Licht und Materie*. PhD thesis, University of Bonn, 2007.

[80] Nathalie Nagl. Resonante Anregung von NV-Zentren und Bestimmung von Glasfaserfluoreszenzen. Bachelor's thesis, Ludwig-Maximilians-Universität München, 2015.

[81] Asmus von Münchow. Das Rasterkraftmikroskop als Werkzeug zur Nanomanipulation von fluoreszierenden Nanodiamantkristallen. Bachelor's thesis, Ludwig–Maximilians–Universität München, 2013.

[82] Andreas W. Schell, Günter Kewes, Tim Schröder, Janik Wolters, Thomas Aichele, and Oliver Benson. A scanning probe-based pick-and-place procedure for assembly of integrated quantum optical hybrid devices. *Review of Scientific Instruments*, 82(7):073709, 2011.

[83] Dingwei Zheng. *Study and Manipulation of Photoluminescent NV Color Center in Diamond*. PhD thesis, f École Normal Supérieure de Cachan, 2010.

[84] Thiago P. Mayer Alegre, Charles Santori, Gilberto Medeiros-Ribeiro, and Raymond G. Beausoleil. Polarization-selective excitation of nitrogen vacancy centers in diamond. *Phys. Rev. B*, 76:165205, 2007.

[85] Kai-Mei C. Fu, Charles Santori, Paul E. Barclay, Lachlan J. Rogers, Neil B. Manson, and Raymond G. Beausoleil. Observation of the Dynamic Jahn-Teller Effect in the Excited States of Nitrogen-Vacancy Centers in Diamond. *Phys. Rev. Lett.*, 103:256404, 2009.

[86] Yuen Yung Hui, Yi-Ren Chang, Nitin Mohan, Tsong-Shin Lim, Yi-Ying Chen, and Huan-Cheng Chang. Polarization Modulation Spectroscopy of Single Fluorescent Nanodiamonds with Multiple Nitrogen Vacancy Centers. *The Journal of Physical Chemistry A*, 115(10):1878–1884, 2011.

[87] Abbas Mohtashami and A. Femius Koenderink. Suitability of nanodiamond nitrogen vacancy centers for spontaneous emission control experiments. *New Journal of Physics*, 15(4):043017, 2013.

[88] Florian Böhm. Tieftemperaturuntersuchungen von Silizium-Fehlstellen-Farbzentren in Diamant-Nanokristallen. Master's thesis, Ludwig-Maximilians-Universität München, 2015.

[89] Lorenz Mayr. Charakterisierung von Nanodiamantkristallen als Einzelphotonenquellen. Bachelor's thesis, Ludwig-Maximilians-Universität München Fakultät für Physik, 2012.

[90] Rishi N. Patel, Tim Schröder, Noel Wan, Luozhou Li, Sara L. Mouradian, Edward H. Chen, and Dirk R Englund. Efficient Photon Coupling from a Diamond Nitrogen Vacancy Centre by Integration with Silica Fibre. *arXiv preprint arXiv:1502.07849*, 2015.

[91] E. A. J. Marcatili. Dielectric Rectangular Waveguide and Directional Coupler for Integrated Optics. *Bell System Technical Journal*, 48(7):2071–2102, 1969.

[92] Y. Zhao, M. Jenkins, P. Measor, K. Leake, S. Liu, H. Schmidt, and A. R. Hawkins. Hollow waveguides with low intrinsic photoluminescence fabricated with Ta2O5 and SiO2 films. *Applied Physics Letters*, 98(9):091104, 2011.

[93] Inc. Lumerical Solutions. *MODE Solutions*.

[94] Vilson R. Almeida, Roberto R. Panepucci, and Michal Lipson. Nanotaper for compact mode conversion. *Optics letters*, 28(15):1302–1304, 2003.

[95] W. K. Burns, A. F. Milton, and A. B. Lee. Optical waveguide parabolic coupling horns. *Applied Physics Letters*, 30(1):28–30, 1977.

[96] Yunfei Fu, Tong Ye, Weijie Tang, and Tao Chu. Efficient adiabatic silicon-on-insulator waveguide taper. *Photonics Research*, 2(3):A41–A44, 2014.

[97] Franco Saworski. Kopplungs- und Propagationsverlust in Ta_2O_5 Singlemode-Wellenleitern. Bachelor's thesis, Ludwig-Maximilians-Universität München, 2013.

[98] Yinan Zhang, Changlin Li, and Marko Loncar. Optimal broadband antireflective taper. *Opt. Lett.*, 38(5):646–648, 2013.

[99] M. Switkes, R. R. Kunz, M. Rothschild, R. F. Sinta, M. Yeung, and S.-Y. Baek. Extending optics to 50 nm and beyond with immersion lithography. *Journal of Vacuum Science & Technology B*, 21(6):2794–2799, 2003.

[100] Wenchuang Walter Hu, Koshala Sarveswaran, Marya Lieberman, and Gary H. Bernstein. Sub-10 nm electron beam lithography using cold development of poly (methylmethacrylate). *Journal of Vacuum Science & Technology B*, 22(4):1711–1716, 2004.

[101] Niko Heinrichs. Design, fabrication and characterization of dielectric Ta2 O5 waveguides. Master's thesis, 2015.

[102] Mustafa Muhammad, Steven C. Buswell, Steven K. Dew, and Maria Stepanova. Nanopatterning of PMMA on insulating surfaces with various anticharging schemes using 30 keV electron beam lithography. *Journal of Vacuum Science & Technology B*, 29(6):06F304, 2011.

[103] Robert G. Hunsperger. *Integrated Optics*. 2002.

[104] Maximilian Göppel. Studien über Transmissionsverhalten und Propagationsverluste bei dielektrischen Ta_2O_5 -Wellenleitern. Master's thesis, Ludwig-Maximilians-Universität München, 2015.

[105] Balpreet Singh Ahluwalia, Olav Gaute Hellesø, Ananth Z. Subramanian, Nicolas M. B. Perney, Neil P. Sessions, and James S. Wilkinson. Fabrication and optimization of Tantalum pentoxide waveguides for optical micro-propulsion. *Proc. SPIE*, 7604:76040W, 2010.

[106] K.-M. C. Fu, C. Santori, P. E. Barclay, I. Aharonovich, S. Prawer, N. Meyer, A. M. Holm, and R. G. Beausoleil. Coupling of nitrogen-vacancy centers in diamond to a GaP waveguide. *Applied Physics Letters*, 93(23):234107, 2008.

[107] Sabine Mittelhammer. Design und Charakterisierung von planaren dielektrischen Wellenleitern. Bachelor's thesis, Ludwig-Maximilians-Universität München, 2013.

[108] Roman Bause. Optimierte Kopplung zwischen planaren optischen Wellenleitern und Glasfasern. Bachelor's thesis, Ludwig-Maximilians-Universität München, 2013.

[109] Lisa Schula. Einbetten von fluoreszierenden Nanodiamanten in SiO_2. Bachelor's thesis, Ludwig-Maximilians-Universität München, 2014.

[110] Syed Abdullah Aljunid, Meng Khoon Tey, Brenda Chng, Timothy Liew, Gleb Maslennikov, Valerio Scarani, and Christian Kurtsiefer. Phase shift of a weak coherent beam induced by a single atom. *Physical review letters*, 103(15):153601, 2009.

[111] Mario Agio and Vahid Sandoghdar. Coherent spectroscopy in strongly confined optical fields . *Physica B: Condensed Matter*, 407(20):4086–4092, 2012.

[112] Meng Khoon Tey, Zilong Chen, Syed Abdullah Aljunid, Brenda Chng, Florian Huber, Gleb Maslennikov, and Christian Kurtsiefer. Strong interaction between light and a single trapped atom without the need for a cavity. *Nature Physics*, 4(12):924–927, 2008.

[113] William J Munro, Kae Nemoto, and Timothy P Spiller. Weak nonlinearities: a new route to optical quantum computation. *New Journal of Physics*, 7(1):137, 2005.

[114] Peter Fischer. Wellenleiter und Einzelphotonenquellen. Master's thesis, Ludwig–Maximilians–Universität München, 2015 (in prep.).

[115] Vilson R. Almeida, Qianfan Xu, Carlos A. Barrios, and Michal Lipson. Guiding and confining light in void nanostructure. *Opt. Lett.*, 29(11):1209–1211, 2004.

[116] Young Chul Jun, Ryan M. Briggs, Harry A. Atwater, and Mark L. Brongersma. Broadband enhancement of light emission insilicon slot waveguides. *Opt. Express*, 17(9):7479–7490, 2009.

[117] Mark P. Hiscocks, Chun-Hsu Su, Brant C. Gibson, Andrew D. Greentree, Lloyd C. L. Hollenberg, and François Ladouceur. Slot-waveguide cavities for optical quantum information applications. *Opt. Express*, 17(9):7295–7303, 2009.

[118] Pao Tai Lin, Sen Wai Kwok, Hao-Yu Greg Lin, Vivek Singh, Lionel C. Kimerling, George M. Whitesides, and Anu Agarwal. Mid-Infrared Spectrometer Using Opto-Nanofluidic Slot-Waveguide for Label-Free On-Chip Chemical Sensing. *Nano Letters*, 14(1):231–238, 2014.

[119] Volker J. Sorger, Nitipat Pholchai, Ertugrul Cubukcu, Rupert F. Oulton, Pavel Kolchin, Christian Borschel, Martin Gnauck, Carsten Ronning, and Xiang Zhang. Strongly

Enhanced Molecular Fluorescence inside a Nanoscale Waveguide Gap. *Nano Letters*, 11(11):4907–4911, 2011.

[120] Yingran He, Sailing He, and Xiaodong Yang. Optical field enhancement in nanoscale slot waveguides of hyperbolic metamaterials. *Opt. Lett.*, 37(14):2907–2909, 2012.

[121] Chunlang Wang, Christian Kurtsiefer, Harald Weinfurter, and Bernd Burchard. Single photon emission from SiV centres in diamond produced by ion implantation. *Journal of Physics B: Atomic, Molecular and Optical Physics*, 39(1):37, 2006.

[122] Elke Neu, Carsten Arend, E. Gross, F. Guldner, Christian Hepp, David Steinmetz, Elisabeth Zscherpel, Slimane Ghodbane, Hadwig Sternschulte, Doris Steinmueller-Nethl, et al. Narrowband fluorescent nanodiamonds produced from chemical vapor deposition films. *Applied Physics Letters*, 98(24):243107, 2011.

[123] Elke Neu, Felix Guldner, Carsten Arend, Yuejiang Liang, Slimane Ghodbane, Hadwig Sternschulte, Doris Steinmueller-Nethl, Anke Krueger, and Christoph Becher. Low temperature investigations and surface treatments of colloidal narrowband fluorescent nanodiamonds. *Journal of Applied Physics*, 113(20):203507, 2013.

[124] A. Sipahigil, K. D. Jahnke, L. J. Rogers, T. Teraji, J. Isoya, A. S. Zibrov, F. Jelezko, and M. D. Lukin. Indistinguishable Photons from Separated Silicon-Vacancy Centers in Diamond. *Phys. Rev. Lett.*, 113:113602, 2014.

[125] Vlasov Igor I., Shiryaev Andrey A., Rendler Torsten, Steinert Steffen, Lee Sang-Yun, Antonov Denis, Voros Marton, Jelezko Fedor, Fisenko Anatolii V., Semjonova Lubov F., Biskupek Johannes, Kaiser Ute, Lebedev Oleg I., Sildos Ilmo, Hemmer Philip. R., Konov Vitaly I., Gali Adam, and Wrachtrup Jorg. Molecular-sized fluorescent nanodiamonds. *Nat Nano*, 9(1):54–58, 2013.

[126] C. Wuttke, M. Becker, S. Brückner, M. Rothhardt, and A. Rauschenbeutel. Nanofiber Fabry-Perot microresonator for nonlinear optics and cavity quantum electrodynamics. *Opt. Lett.*, 37(11):1949–1951, 2012.

[127] Andreas W Schell, Hideaki Takashima, Shunya Kamioka, Yasuko Oe, Masazumi Fujiwara, Oliver Benson, and Shigeki Takeuchi. Highly Efficient Coupling of Nanolight Emitters to a Ultra-Wide Tunable Nanofibre Cavity. *Scientific reports*, 5:9619, 2015.

[128] Roland Albrecht, Alexander Bommer, Christoph Pauly, Frank Mücklich, Andreas W. Schell, Philip Engel, Tim Schröder, Oliver Benson, Jakob Reichel, and Christoph Becher. Narrow-band single photon emission at room temperature based on a single nitrogen-vacancy center coupled to an all-fiber-cavity. *Applied Physics Letters*, 105(7):073113, 2014.

[129] Markus Gregor, Rico Henze, Tim Schröder, and Oliver Benson. On-demand positioning of a preselected quantum emitter on a fiber-coupled toroidal microresonator. *Applied Physics Letters*, 95(15):153110, 2009.

[130] Xu Wang, Samantha Grist, Jonas Flueckiger, Nicolas A. F. Jaeger, and Lukas Chrostowski. Silicon photonic slot waveguide Bragg gratings and resonators. *Opt. Express*, 21(16):19029–19039, 2013.

[131] Carlos Angulo Barrios. Optical slot-waveguide based biochemical sensors. *Sensors*, 9(6):4751–4765, 2009.

[132] Birgit J. M. Hausmann, I. B. Bulu, P. B. Deotare, M. McCutcheon, V. Venkataraman, M. L. Markham, D. J. Twitchen, and Marko Loncar. Integrated high-quality factor optical resonators in diamond. *Nano letters*, 13(5):1898–1902, 2013.

[133] Fam Le Kien and K. Hakuta. Cavity-enhanced channeling of emission from an atom into a nanofiber. *Phys. Rev. A*, 80:053826, 2009.

[134] Alberto Politi, Martin J. Cryan, John G. Rarity, Siyuan Yu, and Jeremy L. O'Brien. Silica-on-silicon waveguide quantum circuits. *Science*, 320(5876):646–649, 2008.

[135] Jacques Carolan, Christopher Harrold, Chris Sparrow, Enrique Martín-López, Nicholas J. Russell, Joshua W. Silverstone, Peter J. Shadbolt, Nobuyuki Matsuda, Manabu Oguma, Mikitaka Itoh, Graham D. Marshall, Mark G. Thompson, Jonathan C. F. Matthews, Toshikazu Hashimoto, Jeremy L. O'Brien, and Anthony Laing. Universal linear optics. *Science*, 349(6249):711–716, 2015.

Danksagung

Ich möchte mich an dieser Stelle bei allen Menschen bedanken, die mich bei die letzten Jahre begleitet und mich bei diesem Projekt direkt oder auch indirekt unterstützt haben.

An erster Stelle danke ich Prof. Harald Weinfurter, der mir als Doktorvater die Promotion an diesem spannenden Projekt ermöglicht hat. Großer Dank gebührt außerdem PD Dr. Markus Weber, der mich intensiv Betreut hat und dessen breite Unterstützung ich genießen durfte. Ich danke Martin Zeitlmair für die gemeinsame Zeit am Projekt, aber auch dafür dass er das Projekt mit Begeisterung fortführt. Ich danke Phillipp Altpeter für die großzügige Unterstützung und Expertise im Reinraum ohne die die Fabrikation der On-Chip-Wellenleiter in dieser Form wohl nicht möglich gewesen wäre. Mein Dank gilt auch Wenjamin Rosenfeld, der sich immer Zeit für aufschlussreiche Diskussionen nahm. Ich danke ausdrücklich den Master- und Diplomstudenten die das Projekt in vielen Aspekten wesentlich vorangebracht haben, Daniel Burchardt, Fabian Petersen, Niko Heinrichs, Florian Böhm, Peter Fischer und Lukas Worthmann. Für ihren wesentlichen Beitrag zum Projekt danke ich außerdem Dr. Toshiyuki Tashima sowie den Bachelorstudenten Lukas Knips, Lorenz Mayr, Asmus von Münchow, Sabine Mittelhammer, Roman Bause, Franco Saworski, Lisa Schula, Johannes Thurner, Nathalie Nagl und Maximilian Göppel.

Ich möchte auch nicht versäumen den Kolaborationspartnern zu danken, Dr. Ariane Stiebeiner für die Optimierung der Fasertaille und Prof. Arno Rauschenbeutel dafür dass er uns die gedünnten Fasern zur Verfügung gestellt hat. Ich danke außerdem Dr. Andreas Schell und Prof. Oliver Benson für die Unterstützung bei der Nanomanipulation der Diamantkristalle.

Ich möchte auch allen weiteren Kollegen danken, die mir mit Rat und Tat zur Seite standen und mir durch eine positive Arbeitsatmosphäre sehr dabei geholfen haben die großen und kleinen Herausforderungen zu bewältigen.

Mit Nachdruck bedanke ich mich auch bei meinen Eltern, Freunden, meinem Bruder aber auch ganz besonders bei meiner Freundin, die während der ganzen Zeit hinter mir standen.